EFFECT OF SHEAR, ELONGATION, AND PHASE SEPARATION IN HOLLOW FIBER MEMBRANE SPINNING

A Dissertation
Presented to
The Academic Faculty

by

Kyung Hee Oh

In Partial Fulfillment
of the Requirements for the Degree
Doctor of Philosophy in the
School of Chemical & Biomolecular Engineering

Georgia Institute of Technology
August 2014

EFFECT OF SHEAR, ELONGATION, AND PHASE SEPARATION IN HOLLOW FIBER MEMBRANE SPINNING

Approved by:

Dr. Victor Breedveld, Advisor
School of Chemical & Biomolecular Engineering
Georgia Institute of Technology

Dr. Hang Lu
School of Chemical & Biomolecular Engineering
Georgia Institute of Technology

Dr. William J. Koros
School of Chemical & Biomolecular Engineering
Georgia Institute of Technology

Dr. Haskell W. Beckham
School of Materials Science & Engineering
Georgia Institute of Technology

Dr. Carson Meredith
School of Chemical & Biomolecular Engineering
Georgia Institute of Technology

Date Approved: March 31, 2014

Dedicated to my loving family

ACKNOWLEDGEMENTS

During my time at Georgia Tech, I was privileged to have many good people who inspired and supported me.

I would like to express my greatest appreciation to my thesis advisor Dr. Victor Breedveld, for his guidance and advice. I was inspired and motivated by his attitude and philosophy toward being a self-critical researcher and doing good science. I am glad to have had the opportunity to work with him, and am appreciative of his patience and encouragement during my trials and errors. I'm grateful to Dr. William J. Koros, for providing practical advice and broad knowledge about membrane production and for allowing me to use resources and facilities. I would like to thank Dr. Hang Lu for helpful discussion about microfluidic device fabrication, and unlimited access to facilities and resources. I am also grateful for Dr. Carson Meredith and Dr. Haskell Beckham for their invaluable advice over polymeric materials.

I am appreciative to past and current group members. I would like to thank Dr. Kayode Olanrewaje and Dr. Tracie Owens for their assistance when I first joined the lab and started PhD research. I would like to thank Dr. Emily C. Peterson and Dr. Lester Li for their companionship during the past four years. I will always remember our discussions over research as well as the jokes and conversations we had. I would like to thank Sri Charan Yarlagadda for sharing good times and hard times in the lab. I'm grateful for Zhenguan Tang, Won Tae Choi, and Lu Jiang for all the laughs in the group. I am also thankful to the Lu group members for helping me to use their facilities.

I will remember the memories that I shared with my friends in Atlanta, Mikyung Cho, Jee Eun Park, Eunji Lim, and Seonhee Park, for being my best friends and for sharing the joyful moments. I would like to extend thanks to Hyea Kim and Shinae Kim for taking care of me as mentors.

I am forever grateful for my mom for her unconditional love and sacrifice. She always encouraged me to have bigger dreams and supported me with all she could. I also thank my brother for being there for me and letting me know he always cares. Special thanks to my cousin, Janice Kim, for being my sister, friend, and personal consultant whenever I had difficulties and obstacles. Finally, I would like to thank my husband, Hyung Chul Kim, for loving and understanding me through this time and for being the love of my life.

TABLE OF CONTENTS

LIST OF TABLES

Page

LIST OF FIGURES

Page

LIST OF SYMBOLS AND ABBREVIATIONS

ϕ_1	Volume fraction
ΔG_m	Gibbs free energy of mixing
a	Cut-off level
D_{eff}	Effective diffusivity of phase separation
E_{coh}	Cohesion energy
n	Power law exponent
n_i	Number of molecules
R	Gas constant
T	Absolute temperature
t	Time
t_{gap}	Residence time in air gap
v_f	Take-up velocity
V_m	Molar volume
v_o	Extrusion velocity
δ	Solubility parameter
Δd	the thickness of phase separated layer
ε	Hencky strain
η	Shear viscosity
η_∞	High shear viscosity
η_e	Elongational viscosity
η_o	Zero shear viscosity
λ	Relaxation time
χ	Flory Huggins interaction parameter

CaBER	Capillary breakup extensional rheometer
CAD	Computer aided design
CCD	Charge coupled device
DR	Draw ratio
FiSER	Fiber stretching extensional rheometer
MG	Macrovoid growth
MW	Molecular weight
N_2	Nitrogen gas
NMP	*N*-Methyl-2-pyrrolidone
PDMS	polydimethylsiloxane
PEI	Polyetherimide
PES	Polyethersulfone
PS	Phase separation
PSK	Phase separation kinetics
SEM	scanning electron microscope
TPE	Thermosetting polyester resin
UCM	Upper Convected Maxwell
wt%	Weight%

SUMMARY

Polymeric membranes are favorable separation media for many industrial applications, due to their low production cost and general ease in processing compared to inorganic materials. The polymer's inherent limits in the separation efficiency (trade-off between gas selectivities and permeance) can be compensated by enhancing the operation capacity through utilizing a hollow fiber configuration or by blending inorganic materials with superior separation performance into the polymer matrix. The potential of materials can be fully utilized when they are processed into a favorable structure and understanding the hollow fiber fabrication process is important. Controlling the various spinning parameters contains many uncertainties and previous research mostly relied on experience and empirical knowledge to optimize process conditions. The complexity of the spinning process can be systematically investigated by focusing on two governing fundamental phenomena: phase separation kinetics (PSK) and rheology (shear and elongation). The kinetics of phase separation has been studied via several experimental methods, but there is a need for a well-controlled experimental setup for quantification of the phase separation kinetics on the relevant timescale and length scale, particularly under the complex conditions (i.e., dry wet phase separation) that are typical for membrane spinning. Furthermore, the effects of rheology, shear and elongational stresses are often not straightforward in the fiber spinning process, and decoupling these variables is essential for understanding and ultimately controlling process conditions. Moreover, instabilities are often encountered during fiber spinning, which limits the range of processing conditions. Instabilities in hollow fiber membrane spinning have hardly been

discussed in open literature yet, and avoiding them is crucial for successful operation of membrane production. This research thesis aimed to study the phase separation and rheology of the polymeric membrane dopes to address the issues described above.

To quantify the kinetics of phase separation, a microfluidic device was designed and combined with peripheral equipment to control environmental conditions. By controlling the solvent evaporation time and humidity exposure time, the kinetics of both wet phase separation and dry-wet phase separation processes could be analyzed quantitatively.

The effects of various flows on membrane morphology were investigated by extruding solid polymer fibers through a straight channel (shear) and a contraction channel (elongation) from the microfluidic device. Correlations were developed between the rheological properties of the membrane dope solutions, the spinning conditions, and resulting membrane morphology; these results are presented as so-called "flow regime maps". *In situ* observation of phase separation and macrovoid formation under different flow conditions revealed that shear stresses induce defect formation while elongational stresses suppress the effect.

One of the commonly encountered instabilities in steady-state fiber spinning is draw resonance, a periodic fluctuation of fiber diameter without breakage. Although discussions of this phenomenon in the membrane literature are limited, researchers in polymer melt spinning have demonstrated that draw resonance starts to occur when applied elongation becomes too high (i.e., high draw ratio). The role of two principle variables, phase separation and rheology, on spinning instability was tested using deliberately formulated samples with desired viscosity and PSK. It was found that faster

PSK is more effective in stabilizing the spinning flow, and many practical methods to stabilize the spinning process by promoting PSK were suggested.

CHAPTER 1

INTRODUCTION

Separation and purification technology is essential in the petrochemical industry and currently exploited in many refineries and other chemical manufacturing processes [1]. Raw materials such as crude oil and natural gas are of relatively little value and they must be separated into refined chemical species to enhance their value. Refined chemicals and gases are important feedstocks in chemical industries, and they can be processed into various products and utilized in many applications. Another important application of separation technology is water purification. In both cases, conventional separation techniques such as distillation, cryogenic distillation, and extraction have been used widely. However, these separation methods have been replaced by membrane separation technology for some applications because of a number of benefits it provides. First, production cost and energy requirement for membrane operation is much less than the thermal techniques. Also, membranes require a relatively small footprint, and operate under benign operating conditions with minimum environmental impact [2]. Because of these advantages, membrane technology is of great interest and it has been a popular option for a wide range of industrial applications, including micro-, nano-, and ultra-filtration, reverse osmosis, and gas separation.

Depending on intended use, the material and fabrication methods for membranes should be carefully chosen. In filtration membranes, the separation efficacy is mostly determined by the membrane pore size; i.e. the separation is based on size exclusion

mechanism. For example, the porosity of microfiltration membrane is between 10^{-5} ~ 10^{-7} m, and nano- or ultra-filtration membranes are in a range of 10^{-7} ~ 10^{-9} m [3]. For gas separation or reverse osmosis application, membranes with pore size less than 10^{-9} m are commonly used, but the separation mechanism differs from the filtration membranes. The gas transport in a dense matrix occurs through a solution-diffusion mechanism: first sorption of various gas species from a feed to a membrane , then diffusion of the gas species across the membrane and ultimately desorption of the gas species from the membrane on the downstream side [3, 4].

Various materials have been considered as a candidate for membranes, both organic and inorganic materials. Among them, polymers are one of the most common membrane materials, because of their low production cost and ease of processing. Polymers exhibit relatively high selectivities (preferential permeation of one component over another), but they have relatively low permeance (the flux of an individual component across the membrane) due to low free volume [2]. They also have certain drawbacks in application. For example, they are vulnerable at high temperature and in exposure to hydrocarbon or CO_2, which can cause deformation and plasticization. Another major limitation in separation performance of polymers, reported by Robeson [5], is the fact that the separation efficiency is determined by the trade-off between the selectivities and the permeabilites. For example, when polymeric membranes exhibit high selectivities, the permeance is kept low, and vice versa. As such, many inorganic materials such as ceramic, glass, metal, silica, zeolite, and carbon-based molecular sieves have been prepared to overcome polymer's drawbacks. However, the preparation of these materials into membranes is much more difficult than polymers and these materials also

have critical drawbacks such as high processing cost, low yield, mechanical brittleness, difficulty in processing [2, 3]. Recently, modified polymeric membranes were proposed, such as mixed matrix materials, in attempts to combine the easy processability of polymers with the superior separation efficiency of inorganic materials. Although theses hybrid membranes achieved excellent separation performance, the fabrication of successful mixed matrix membranes still requires more research to overcome several problems such as the weak interaction between the polymer matrix and the inorganic fillers.

Therefore, despite of the limitations in maximum separation efficiency (tradeoff between permeability and selectivity), polymers are still one of the most attractive materials. Their modest separation performance can be compensated by processing them into hollow fiber membranes with asymmetric morphology [6]. As discussed in the next section, hollow fiber membranes offer extra benefits in addition to flat sheet membranes but their fabrication has often relied on trial and error and empirical knowledge. Understanding the fundamentals of the polymeric hollow fiber fabrication process will allow us to exploit new polymers as hollow fiber membranes and further will be helpful in developing polymer-based hybrid membranes.

1.1. Ideal morphology of polymeric hollow fiber membranes

Unlike flat sheet membranes and tubular membranes, hollow fiber membranes are mechanically self-supported structures due to their small dimension, with diameters of less than 0.5 mm. Thousands of hollow fibers can be assembled to form a membrane

module, which enables convenient scale up for large-scale industrial applications [7, 8]. The self-supported structure and high membrane area per module volume lead to cost reduction and high separation capacity, which are recognized as additional advantages of hollow fiber membranes in industrial applications. The ideal morphology of hollow fiber membranes is an asymmetric structure that consists of a thin outer skin layer and porous structure as inner core (**Figure 1.1**). The dense skin layer (ideally < 1 μm) contributes to the separation while the inner porous structure functions as mechanical support.

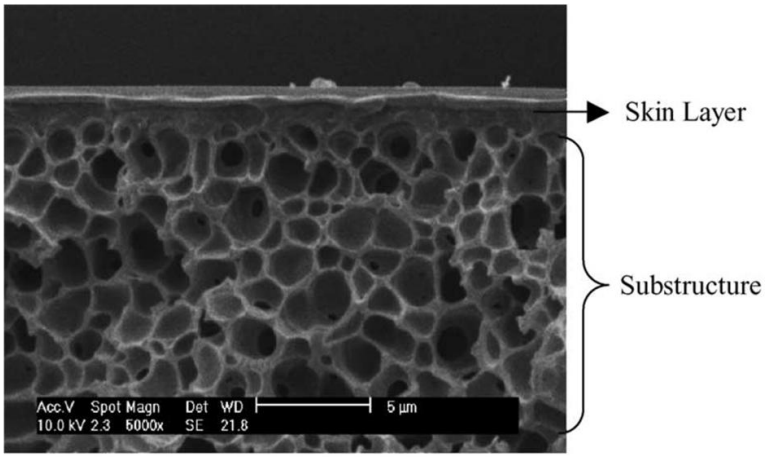

Figure 1.1 Asymmetric hollow fiber membrane structure [9].

The ideal structure should be also free from defects, which can be mainly divided into two types: microscopic and macroscopic defects. Microscopic defects are unperceivable defects on the nanoscale such as cracks or cavities in the skin layer that reduce the material's inherent gas separation performance. On the other hand, macroscopic defects, also referred to as macrovoids, are cavities of the order of tens of micrometers that reduce the mechanical strength and integrity of the membranes. The

formation mechanism of both types of defects requires further understanding and ultimately they should be avoided for successful membrane operation.

1.2. Hollow fiber membrane fabrication (spinning process)

The fabrication of hollow fiber membranes with desirable morphology is challenging as the membrane fabrication process consists of various flows as well as multi-component mass transfer. The precursor of the polymeric membranes is a “dope” solution, a liquid-state homogeneous polymer solution that consists of polymer/solvent/nonsolvent (co-solvent). The polymer solution is extruded through an annular spinneret with a bore fluid (a mixture of solvent/nonsolvent) in the middle in order to form hollow fibers (**Figure 1.2**). After being extruded, the polymer solution phase-separates (i.e. a liquid polymer solution turns into solid state hollow fibers) as it contacts the nonsolvent bath and is taken up by a rotating drum at the end of the spinning line. In the spinning process, phase separation occurs at two locations: slow phase separation occurs at the interface between the polymer solution and the bore fluid, while faster phase separation occurs at the interface between the polymer solution and the nonsolvent bath. The difference in kinetics between these phase separation processes contributes to the formation of the desired asymmetric membrane structures.

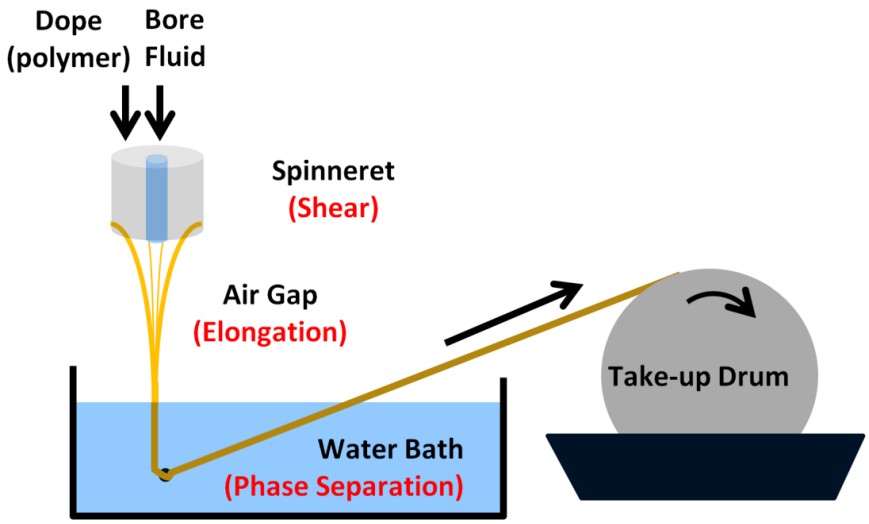

Figure 1.2. Schematic of the hollow fiber membrane spinning process.

1.3. Material selection

The choice of polymer, solvent, and nonsolvent for the membrane dope is critically important as it has significant impact on membrane morphology, separation performance and mechanical properties. The interaction between solvent and polymer is described by polymer solubility, and the interaction between solvent and nonsolvent can be described by miscibility. The polymer must be soluble in the solvent in order to form a homogenous liquid solution, and miscibility between solvent and nonsolvent is also crucial on final membrane morphology [10]. Several methods have been developed for determining polymer solubility. Flory-Huggins solution theory, which is also referred to as a lattice model, has been used to describe mixing of polymer and solvents [11-13]. It

was assumed that all the polymer segments and the solvent molecules have the same size and they can occupy a single site on a lattice. Then, the Gibbs free energy of mixing is

$$\Delta G_m = RT(n_1 ln\phi_1 + n_2 ln\phi_2 + \chi_{12} n_1 \phi_2) \quad (1.1)$$

where n_1 and n_2 are the number of molecules of component 1 (solvent) and component 2 (polymer), respectively; ϕ_1 and ϕ_2 are the volume fraction of component 1 and component 2, respectively; R is a gas constant, T is the absolute temperature, and χ_{12} is the Flory-Huggins interaction parameter. The Flory-Huggins interaction parameter can be approximated by first introducing a solubility parameter, δ, which is defined as the cohesion energy divided by the molar volume, as proposed by Hildebrand [14, 15].

$$\delta = \sqrt{\frac{E_{coh}}{V}} \quad (1.2)$$

Then, the Flory Huggins interaction parameters can be estimated from solubility parameters (δ_1 and δ_2 for solvent and polymer, respectively) via the following equation:

$$\chi_{12} = \frac{v_1}{RT}(\delta_1 - \delta_2)^2 \quad (1.3)$$

where v_1 is the molar volume of the solvent. While Hildebrand solubility only accounts for dispersive forces, Hansen proposed the concept of advanced solubility parameters that can apply to substances that interact through dipole-dipole polar forces and hydrogen bonding in addition to dispersion forces [16, 17]. Hansen solubility parameter consists of

three components: dispersive (δ_d), polar (δ_p), and hydrogen bonding (δ_h) and the difference in Hansen solubility parameter, Δδ, is a good estimate for the prediction of solvent miscibility or polymer solubility:

$$\Delta\delta_{12} = \sqrt{(\delta_{d,1} - \delta_{d,2})^2 + (\delta_{p,1} - \delta_{p,2})^2 + (\delta_{h,1} - \delta_{h,2})^2} \qquad (1.4)$$

where subscripts 1 and 2 represent component 1 and 2, respectively.

Although the Hildebrand and Hansen solubility parameters must be considered for the selection of materials and the composition, the morphology of the membrane should also be optimized in order to utilize the full potential of the materials. In the next section, the key variables in hollow fiber spinning process will be introduced.

1.4. Important variables in hollow fiber membrane spinning

The complexity of the fabrication originates from many processing parameters such as spinneret dimensions, extrusion rate, air gap distance, draw ratio (the ratio of extrusion rate and the final take-up rate), and so on. Many researchers have attempted to understand the effects of these parameters on the resulting hollow fiber membranes. In the literature, the separation performance of hollow fiber membranes is usually reported along with the used materials, solution composition, and specific spinning conditions. A comprehensive literature review of studies of individual parameters is given in **Table 1.1**. Controlling parameters are, for example, shear rate (sometimes presented as extrusion rate, or dope flow rate), air gap distance, spinneret design, and draw ratio in the

isothermal fiber spinning. As can be seen in **Table 1.1**, the literature results are often contradictory and confusing with regards to the effects of individual processing parameters.

The hollow fiber spinning process can be dissociated into two steps, pre-phase separation and the phase separation. Before phase separation, the polymeric fluid is subjected to complicated flow conditions and polymer macromolecules are likely to deform due to exerted stresses. Then, during the phase separation, the fluid transforms into a solid membrane as it enters the air gap and nonsolvent bath. The key variables governing hollow fiber membrane spinning are the dope rheology, which is related to the characteristic fluid behavior prior to the phase separation and the phase separation process, which determines the membrane morphology

Table 1.1 Review of effects of spinning parameters and characterization of hollow fiber membranes

Processing parameter	Characterization method	Results	Comments
Shear rate (flow rate or extrusion rate)	Macrovoid defect	Macrovoids at all shear rates [18-23]. No macrovoids [24]. Suppressed macrovoids with an increase of shear rates [25].	Information of phase separation kinetics is not considered.
	Dimension	Expansion of the membrane dimensions [19, 25]. Constant membrane dimensions at all shear rates [20, 22-24].	
	Ultra-filtration	Increased filtration capacity (can filter smaller particles) and decreased pure water flux with an increase of shear [20, 22, 23].	
	Gas separation	Increased permeance [24] and decreased permeance [21] with increasing shear. Fluctuation in selectivities with shear [21, 24].	
	Molecular orientation	Increased then decreased [26], Increased [27]	
Air gap	Macrovoid defect	Suppressed macrovoids [28], Increased macrovoids [29], No macrovoid [30].	Information of phase separation kinetics is not considered.
	Gas separation	Decreased permeance [28, 30]. Increased selectivities [30]	
Draw ratio (or take up speed)	Gas separation	Decreased permeance and increased selectivity [31].	Change in the residence time at the air and fiber dimensional change is not considered.
	Mechanical properties	Increased mechanical strength [31].	
	Macrovoid defect	Suppressed macrovoids [32, 33].	

1.4.1. Phase separation in hollow fiber membrane spinning

The asymmetric morphology of polymeric membranes is formed by non-solvent-induced phase separation [6, 34]. The rapid exchange of solvent and non-solvent occurs at the interface between the fiber and the bath, and through removal of solvent, the porous structure of the polymer membrane is formed.

To achieve the phase separation, the following three methods are commonly used [35]. Dry phase preparation [36], also referred to as air casting, is induced by placing the dope solution under ambient air, causing vapor/moisture-induced phase separation or the evaporation of volatile solvent. Wet phase separation [36] is caused by a change in composition because of the invasion of non-solvent. Dry-wet phase separation [35, 37, 38], which is a sequential combination of air casting and immersion casting, occurs in the outer layer on the hollow fiber membrane, and the membranes produced via this method are known to exhibit the best performance in gas separation application.

The phase separation process determines all critical elements of the membrane morphology, including the thickness of the dense outer skin layer that is responsible for most of the separation characteristics of the membrane. Understanding and manipulation of phase separation is therefore very important, not only because it determines the membrane morphology but also because macroscopic membrane defects (macrovoids) are often formed during this process. Researchers found that membrane morphology is affected by two important aspects: equilibrium thermodynamics and phase separation kinetics [39-42]. These aspects will be discussed in detail in the next few sections.

1.4.1.1. Thermodynamics of phase separation

To explain the thermodynamic change during phase separation, a ternary phase diagram of polymer/solvent/nonsolvent is used [34], as shown in **Figure 1.3**. The left side of binodal curve is one phase where the all components in the polymeric dope are well mixed to form a homogeneous solution. To the right of the binodal curve is the two-phase region where the solid polymer phase demixes from the solvent and non-solvent to start forming the characteristic membrane structure. Binodal curves can be determined by the cloud point measurement, which is typically done through the gradual addition of nonsolvent to the dope solution until the dope solution becomes turbid (cloud point).

The composition paths during the phase separation were postulated and marked on **Figure 1.3** [33]. From the characterization of the membrane morphology including the overall porosity and pore size distribution, the hypothesized composition paths are going through one phase regime (1→2) and through spinodal regime (1→3). For example, the dense skin layer formation, which is believed to be generated by the evaporation of the volatile solvent, is likely to go through one phase regime because the evaporation of solvent will increase the polymer concentration in the dope solution [33]. Meanwhile, the composition change through spinodal regime will likely occur by nonsolvent introduction, which increase the nonsolvent concentration immediately. However, it is premature to believe these hypothesized composition paths, as they lack information on the actual phase separation kinetics.

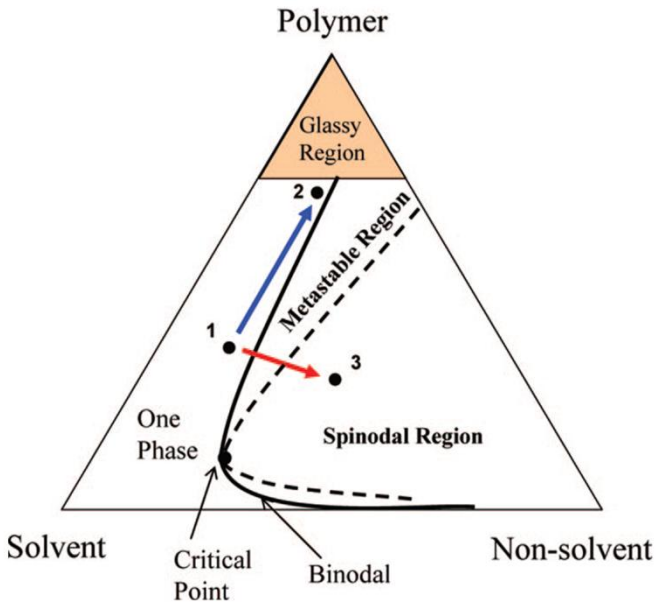

Figure 1.3. Ternary phase diagram and phase transition path during phase separation [33].

1.4.1.2. The kinetics of phase separation

Although the equilibrium thermodynamics can be utilized as a good guideline to formulate initial dope composition, it does not predict the dynamics of compositional change and structure formation during phase separation. Dynamics of phase separation is closely related to the resulting membrane morphology; empirically, it is known that the faster phase separation results in a dense structure with finger-like macrovoids, whereas the slower phase separation results in a sponge-like porous structure.

Multi-component mass transport during phase separation has been modeled by many researchers [39, 40, 43]. Reviewing the transport modeling in details is beyond the scope of this thesis. Here, we have focused more on the development of a methodology of characterizing the transport that is intuitive and straightforward. For that purpose, the

following relationship between developing thickness of the phase separated layer and time will be used as a measure of phase separation rate with an assumption that the nonsolvent molecules diffuse in one dimension without convection [43, 44]

$$\Delta d = \sqrt{2D_{eff}t} \quad (1.5)$$

where Δd is the thickness of the phase separated layer, t is the elapsed time, and D_{eff} is the effective diffusivity phase separation.

1.4.2. Dope rheology in hollow fiber membrane spinning

The hollow fiber fabrication process entails various flows and sometimes the characteristic features of polymeric dopes arise in the process. For example, die swell, a rapid expansion in fiber diameter when the dope is extruded from a narrow orifice, is commonly observed in the spinning. It is an example of the typical non-Newtonian behavior, where the polymer molecules deform and reorient themselves in effort to relax imposed stresses. In hollow fiber membrane spinning, the flow conditions are dominated by shear and elongational flows.

1.4.2.1. Shear rheology of membrane dopes and limitations in measurement

When the concentrated polymer solutions are exposed to high shear stresses, the polymer molecules deform and the solutions exhibit non-Newtonian rheological behavior, usually shear thinning with a viscosity drop at high shear rates. The range of measurable shear rate is limited by the non-Newtonian behavior, which is referred as Weissenberg effect (rod climbing effect). The value of typical upper limit of shear rate for membrane dopes is approximately 100 ~ 400 s^{-1}, which is often close to the onset of

the shear thinning on the flow curve. The viscosity measurements of highly concentrated polymer solutions at high shear rates often encounter difficulties due to instrumental limitation, and few studies have been conducted with regards to the effect of shear thinning viscosity on spinnability and membrane morphology. Instead, the simplest way to quantify the viscosity of polymer solutions is to measure the zero shear viscosity, i.e. viscosity at very low shear rates, with a conventional rotational rheometer. The zero shear viscosity of the dopes has been employed as an empirical reference for determining the spinnable dope composition. For example, it is well-known that the zero shear viscosity of dopes increases with an increase of polymer concentration and an increase of the polymer molecular weight.

Although zero shear viscosity may be an easily measurable parameter, the rheological behavior in the shear thinning regime may be more relevant to the spinning conditions, where the shear rates are very high (~1000 s^{-1}). The full flow curves (viscosity as a function of shear rate) can be employed for estimation of the shear rates in the spinnerets during the extrusion process. Some researchers attempted to estimate the shear rates using the assumption that the membrane dopes behave like a Power-law fluid [23]. The power-law viscosity model effectively captures the shear thinning behavior at high shear rates but the instrumental limitations mentioned above only allowed researchers to measure a narrow range of shear rates, so that shear rate calculations had significant errors. More specifically, their dope solution seemed mildly shear thinning over the measured range of shear rates, and as a result, their solution seemed close to Newtonian. In order to make accurate shear rate estimates for the flow in the spinneret, the viscosity profile must be determined over a wide range of shear rates.

1.4.2.2. Literature research: assessment of effect of shear

Researchers have attempted to demonstrate the effects of shear stresses on final membrane products, as shown in **Table 1.1**. The characterization methods were macrovoid density in the membranes, membrane dimensions, separation efficiency, glass transition temperature and mechanical properties of membranes spun at various shear rates [18-25]. These experiments were conducted with similar approach; to preserve the effects of shear and prevent the effects of stress relaxation, all the membranes were spun with zero air gap (wet spinning). Also, to eliminate the elongational effects, the draw ratio was kept constant at the unity by adjusting drum take-up rates. However, the results were quite confusing. In many researches, the wet-spun hollow fiber membranes exhibited a number of macrovoids regardless of the shear rates [18-23]. To contrast, in other study, no macrovoids were found in the wet-spun hollow fiber membranes and the author explained that the high dope viscosity may have suppressed the macrovoid formation [24]. However, Wang et al. found that macrovoids could be gradually reduced by an increase of shear rates (323 – 12930 s^{-1}) even with a lower viscosity dope (7.9 Pa s) [25]. In addition, some researchers reported that increasing shear sometimes induced an expansion of the membrane dimensions [19, 25] while others insisted that the membrane dimensions were kept almost constant [20, 22-24] at all shear rates. In application of ultra-filtration, the filtration capacity increased (can filter smaller particles) and the water flux (permeability) increased with an increase of shear [20, 22, 23]. In case of gas separation, the wet spun membrane fibers were post-treated (coated with another layer) and the permeance was increased [24] and decreased [21] with shear, while there is no strong tendency in selectivities [21, 24]. Contradictory results indicate that effects of a

single parameter on separation performance or morphology of membranes is not straightforward and may be complicated with other parameters.

1.4.2.3. Elongational rheology of polymeric dopes and limitations in measurement

Elongational viscosity may have strong relation to dope spinnability because elongational deformation occurs right before the phase separation and thus elongation-induced structural change is well preserved after phase separation. Nevertheless, few discussions are present in the open literature on the elongational rheology of dope solutions, probably because the assessment of elongational viscosity is much more difficult than that of shear.

Unlike the well-established measurement of shear rheology, effective measurement methods for elongational viscosity are still a matter of developments and controversy. Due to the nature of elongational flow, generation of a steady-state elongational flow is impossible to achieve. The most widely used extensional rheometers are FiSER (filament stretching extensional rheometer) and CaBER (Capillary breakup extensional rheometer). The advantage of FiSER is viscosity measurement at constant elongational rates (not steady state) in the system where the distance of the two plates increases exponentially and the fluid placed between the two plates becomes thinner as time elapses. However, the drawback of this equipment is a large special requirement to achieve the exponential displacement, and thus this equipment is not easily accessible in an individual research lab. On the other hand, CaBER requires a small space and allows measurement of moderate elongational rates. However, the measurable deformation rate

is automatically limited by the viscosity of the fluid, and only an apparent elongational viscosity is measured.

Another challenge in measuring elongational viscosity is that it is not always predictable from shear rheology. In case of Newtonian fluids, the elongational viscosity obeys the Trouton ratio and is equal to three times the shear viscosity [45]. However, typical polymer solutions deviate from the Trouton ratio and sometimes polymers that exhibit shear-thinning behavior show strain-hardening along with the elongational deformation.

1.4.2.4. Literature research: assessment of effect of elongation

In spite of instrumental limitations in elongational viscosity measurements, researchers have found that elongational stresses can lead to macrovoid suppression and improvement of separation performance. Ekiner and Vassilatos characterized the elongational viscosity change of polyaramide solution in the spinline using non-contact laser-Doppler velocimetry [31]. They calculated that the elongational viscosity of polyaramide increased three times from its initial value (strain-thickening) and the membranes spun at high draw ratio (take-up velocity/extrusion velocity) exhibited lower permeance, higher selectivity, and superior mechanical properties [31]. Also, in both pure polymeric membranes and mixed matrix membranes, the number of macrovoids was suppressed with increasing draw ratio [32, 33]. However, suppression of macrovoid formation may not entirely result from high draw ratio. Increasing draw ratio also decreases the dimensions of the membrane fibers and decreases their residence time in the air gap. In this case, complications in interpreting results arise from the fact that

thinner membranes inherently contain fewer macrovoids in studies of flat membranes even without considering elongational stresses [46]. It is also important to note that residence time in the air gap affects solvent evaporation time, which can have an impact on final morphology and separation capacity. Decoupling of elongational stresses from other effects has not been attempted systematically.

1.5.Research Objectives & thesis overview

In this thesis, the overarching goal is to understand the effects of key variables, phase separation kinetics (PSK) and rheology on the membrane morphology and the processability in the hollow fiber membrane spinning.

In Chapter 2, the research objective is quantitative analysis of the kinetics of dry wet phase separation and wet phase separation through *in situ* visualization. Large portion of this Chapter describes the fabrication of microfluidic device that can be optimized for dry wet or wet phase separation experiments. The effects of solvent evaporation in a short timescale, polymer molecular weight, and the nonsolvents on PSK and morphology in dry wet phase separation are demonstrated with a microfluidic device with enhanced controllability in air/liquid flow. Phase separation kinetics and the resulting microstructure are presented as two-tier experiments.

In Chapter 3, the research objective is to characterize the shear and elongational rheology of membrane dopes and examine the effects of dope rheology on polymer morphology. The effects shear and elongational flows on membrane morphology are demonstrated by extrusion through a straight channel for shear and a contraction channel for elongation in the microfluidic device. The materials' rheological properties, phase separation video, and accordingly resulting membrane morphology are presented onto a flow regime map. *In situ* observation of phase separation and macrovoid formation under different flow conditions clearly evidence to the fact that shear stresses induce macrovoid formation while elongational stresses suppress it.

In Chapter 4, the research objective is to investigate the instabilities in fiber spinning and determine the role of rheology and phase separation kinetics. The shear

viscosity and the phase separation kinetics of binary system (polymer/solvent) and ternary (polymer/solvent/volatile co-solvent) are investigated, and the spinnability test is performed with solid fiber spinning. This research emphasizes the importance of moisture-induced phase separation in air gap, which can lead to stabilization of the spinning flow.

In Chapter 5, the major conclusions of this thesis will be listed with recommendations for future research.

1.6. References

[1] P. Bernardo, G. Clarizia, 30 years of membrane technology for gas separation, Chemical Engineering (New York), 32 (2013).

[2] P. Bernardo, E. Drioli, G. Golemme, Membrane gas separation: a review/state of the art, Industrial & Engineering Chemistry Research, 48 (2009) 4638-4663.

[3] H. Strathmann, Introduction to membrane science and technology, John Wiley & Sons, Incorporated, 2011.

[4] J.G. Wijmans, R.W. Baker, The solution-diffusion model: a review, Journal of Membrane Science, 107 (1995) 1-21.

[5] L.M. Robeson, Correlation of separation factor versus permeability for polymeric membranes, Journal of Membrane Science, 62 (1991) 165-185.

[6] S. Loeb, S. Sourirajan, Sea water demineralization by means of an osmotic membrane, ACS Publications, 1962.

[7] D. Wallace, C. Staudtbickel, W. Koros, Efficient development of effective hollow fiber membranes for gas separations from novel polymers, Journal of Membrane Science, 278 (2006) 92-104.

[8] W.J. Koros, R.P. Lively, Water and beyond: expanding the spectrum of large-scale energy efficient separation processes, AIChE Journal, 58 (2012) 2624-2633.

[9] A.F. Ismail, P.Y. Lai, Development of defect-free asymmetric polysulfone membranes for gas separation using response surface methodology, Separation and Purification Technology, 40 (2004) 191-207.

[10] M. Mulder, Basic principles of membrane technology, Kluwer Academic, 1996.

[11] P.J. Flory, Thermodynamics of high polymer solutions, The Journal of Chemical Physics, 10 (1942) 51-61.

[12] M.L. Huggins, Some properties of solutions of long-chain compounds, The Journal of Physical Chemistry, 46 (1942) 151-158.

[13] M.L. Huggins, Theory of solutions of high polymers, Journal of the American Chemical Society, 64 (1942) 1712-1719.

[14] J. Hildebrand, The solubility of non-electrolytes; Reinhold: New York, 1936, There is no corresponding record for this reference.

[15] G. Scatchard, Equilibria in non-electrolyte solutions in relation to the vapor pressures and densities of the components, Chemical Reviews, 8 (1931) 321-333.

[16] C.M. Hansen, The three dimensional solubility parameter, Danish Technical: Copenhagen, (1967) 14.

[17] C.M. Hansen, Hansen solubility parameters: a user's handbook, CRC press, 2012.

[18] J. Ren, R. Wang, H.-Y. Zhang, Z. Li, D.T. Liang, J.H. Tay, Effect of PVDF dope rheology on the structure of hollow fiber membranes used for CO2 capture, Journal of Membrane Science, 281 (2006) 334-344.

[19] L. Shi, R. Wang, Y. Cao, Effect of the rheology of poly(vinylidene fluoride-co-hexafluropropylene) (PVDF–HFP) dope solutions on the formation of microporous hollow fibers used as membrane contactors, Journal of Membrane Science, 344 (2009) 112-122.

[20] J.-J. Qin, Investigation of shear stress effect within a spinneret on flux, separation and thermomechanical properties of hollow fiber ultrafiltration membranes, Journal of Membrane Science, 175 (2000) 197-213.

[21] T.-S. Chung, Effect of shear stress within the spinneret on hollow fiber membrane morphology and separation performance, Industrial and Engineering Chemistry Research, 37 (1998) 3930-3938.

[22] J. Qin, Effect of dope flow rate on the morphology, separation performance, thermal and mechanical properties of ultrafiltration hollow fibre membranes, Journal of Membrane Science, 157 (1999) 35-51.

[23] T.-S. Chung, J.-J. Qin, J. Gu, Effect of shear rate within the spinneret on morphology, separation performance and mechanical properties of ultrafiltration polyethersulfone hollow fiber membranes, Chemical Engineering Science, 55 (2000) 1077-1091.

[24] T.-S. Chung, Effect of shear rates on gas separation performance of 6FDA-durene polyimide hollow fibers, Journal of Membrane Science, 167 (2000) 55-66.

[25] K. Wang, The effects of flow angle and shear rate within the spinneret on the separation performance of poly(ethersulfone) (PES) ultrafiltration hollow fiber membranes, Journal of Membrane Science, 240 (2004) 67-79.

[26] A. Idris, A.F. Ismail, M. Noorhayati, S.J. Shilton, Measurement of rheologically induced molecular orientation using attenuated total reflection infrared dichroism in reverse osmosis hollow fiber cellulose acetate membranes and influence on separation performance, Journal of Membrane Science, 213 (2003) 45-54.

[27] A.F. Ismail, S.J. Shilton, I.R. Dunkin, S.L. Gallivan, Direct measurement of rheologically induced molecular orientation in gas separation hollow fibre membranes and effects on selectivity, Journal of Membrane Science, 126 (1997) 133-137.

[28] T.-S. Chung, Effect of air-gap distance on the morphology and thermal properties of polyethersulfone hollow fibers, Journal of Applied Polymer Science, 66 (1997) 1067-1077.

[29] N. Widjojo, Thickness and air gap dependence of macrovoid evolution in phase-inversion asymmetric hollow fiber membranes, Industrial and Engineering Chemistry Research, 45 (2006) 7618-7626.

[30] T.-S. Chung, Fundamental understanding of the effect of air-gap distance on the fabrication of hollow fiber membranes, Journal of Applied Polymer Science, 72 (1999) 379-395.

[31] O.M. Ekiner, G. Vassilatos, Polyaramide hollow fibers for H2/CH4 separation: II. Spinning and properties, Journal of Membrane Science, 186 (2001) 71-84.

[32] K.Y. Wang, D. Fei Li, T.-S. Chung, S. Bor Chen, The observation of elongation dependent macrovoid evolution in single- and dual-layer asymmetric hollow fiber membranes, Chemical Engineering Science, 59 (2004) 4657-4660.

[33] S. Husain, W.J. Koros, Macrovoids in hybrid organic/inorganic hollow fiber membranes, Industrial & Engineering Chemistry Research, 48 (2009) 2372-2379.

[34] H. Strathmann, K. Kock, The formation mechanism of phase inversion membranes, Desalination, 21 (1977) 241-255.

[35] I. Pinnau, W.J. Koros, Structures and gas separation properties of asymmetric polysulfone membranes made by dry, wet, and dry/wet phase inversion, Journal of Applied Polymer Science, 43 (1991) 1491-1502.

[36] R.E. Kesting, Synthetic polymeric membranes: a structural perspective, Wiley, 1985.

[37] D.R. Paul, Polymeric gas separation membranes, CRC Press, 1994.

[38] I. Pinnau, J. Wind, K.V. Peinemann, Ultrathin multicomponent poly(ether sulfone) membranes for gas separation made by dry/wet phase inversion, Industrial & Engineering Chemistry Research, 29 (1990) 2028-2032.

[39] C. Cohen, G.B. Tanny, S. Prager, Diffusion-controlled formation of porous structures in ternary polymer systems, Journal of Polymer Science: Polymer Physics Edition, 17 (1979) 477-489.

[40] A.J. Reuvers, J.W.A. van den Berg, C.A. Smolders, Formation of membranes by means of immersion precipitation : Part I. A model to describe mass transfer during immersion precipitation, Journal of Membrane Science, 34 (1987) 45-65.

[41] A.J. Reuvers, C.A. Smolders, Formation of membranes by means of immersion precipitation : Part II. the mechanism of formation of membranes prepared from the system cellulose acetate-acetone-water, Journal of Membrane Science, 34 (1987) 67-86.

[42] C.A. Smolders, A.J. Reuvers, R.M. Boom, I.M. Wienk, Microstructures in phase-inversion membranes. Part 1. Formation of macrovoids, Journal of Membrane Science, 73 (1992) 259-275.

[43] C.S. Tsay, A.J. McHugh, Mass transfer modeling of asymmetric membrane formation by phase inversion, Journal of Polymer Science Part B: Polymer Physics, 28 (1990) 1327-1365.

[44] H. Strathmann, K. Kock, P. Amar, R.W. Baker, The formation mechanism of asymmetric membranes, Desalination, 16 (1975) 179-203.

[45] C.W. Macosko, Rheology: principles, measurements, and applications, Wiley-VCH, 1994.

[46] J. Ren, J. Zhou, M. Deng, Morphology transition of asymmetric polyetherimide flat sheet membranes with different thickness by wet phase-inversion process, Separation and Purification Technology, 74 (2010) 119-129.

CHAPTER 2

MICROSCOPIC STUDIES OF WET AND DRY/WET PHASE SEPARATION KINETICS OF POLYMERIC MEMBRANE DOPES

2.1. Introduction

The ideal morphology of hollow fiber membranes is characterized by asymmetric structures, consisting of an outer selective skin layer that contributes to the separation performance, and an inner porous substructure that provides mechanical strength. This asymmetric structure is generally created by nonsolvent-induced phase inversion [1] and the formation of a dense skin layer is often enhanced by an additional solvent evaporation step in the air gap (dry casting) prior to nonsolvent-induced phase separation (wet casting) in the spinning process of hollow fiber membranes.

Phase separation determines the overall porosity and pore size distribution of the membrane; the kinetics of this process is controlled by both thermodynamics and mass transfer rates. To predict the phase behavior, a phase diagram of the dope solution (polymer/solvent/nonsolvent) during the phase separation is used (see **Figure 1.3**) and the choice of dope composition is narrowed down iteratively by assessing the morphology of the final product. The dynamics of multi-component mass transfer during phase separation is equally significant and closely related to the resulting membrane morphology. More importantly, unlike equilibrium thermodynamics, for which samples can easily be prepared and monitored, phase separation kinetics in a typical spinning

apparatus for membrane fabrication cannot readily be quantified. Therefore, an appropriate device is necessary to study the phase separation kinetics on the relevant length and time scales.

The first successful approach to measuring phase separation kinetics was the use of a light transmittance method [2-4]. After casting the dope solution onto a flat transparent substrate, the evolution of phase separation was monitored by quantifying the reduction of transmitted light intensity through the initially transparent polymer solution upon phase separation. This method is in principle applicable to both dry and wet phase separation [4, 5], but only provides relative phase separation rates between samples, because it is not straightforward to relate transmitted intensity quantitatively to the progression of the phase separation front through the solution. Moreover, this method does not enable direct visualization of the actual structure formation during phase separation, and the apparent phase separation rates can be biased by optical properties of different polymers or the length scales of inhomogeneous structure such as macrovoids. Another successful method for measuring phase separation kinetics is direct visualization through an optical microscope. Matz [6] first observed real-time phase separation by placing a drop of polymer solution between a slide glass and a cover slip and bringing the solution in contact with drops of water at the edges to initiate phase separation. The main advantage of this method is real-time visualization of phase separation across the sample, providing a clear view of both the interface between solution and nonsolvent and the moving phase separation boundary. Furthermore, by reducing the gap between the two glass surfaces and thus enhancing optical contrast, direct observation of macrovoid formation is possible. This method has since been used by many researchers [7-10] for

qualitative studies of parameters such as polymer concentration, nonsolvent concentration in the dope, polymer additives, and surfactants on phase separation kinetics and membrane morphology. Using this approach, Gullien et al. [8] demonstrated that the growth of macrovoids is proportional to the square root of elapsed time, and that these macrovoid defects grow slightly faster than the rate at which the phase separation boundary moves through the sample.

Although the parallel glass geometry is a simple method for qualitative measurement of phase separation kinetics, it is not accurate enough for quantitative analysis, as it contains several uncertainties that can lead to significant experimental errors. First of all, samples are exposed to air during the preparation, and premature phase separation may occur at the interface for moisture-sensitive samples; this is particularly relevant because water is a common nonsolvent. Also, the gap between the two glass surfaces may not be uniform, and the polymer experiences the biaxial extension during the loading. These experimental uncertainties can bias the experimental results and affect reproducibility. Therefore, as an alternative, in this study a microfluidic device will be used for a quantitative analysis of phase separation kinetics. Olanrewaju [11] developed the first version of such a device for the study of phase separation kinetics. His device yielded good reproducibility because of the precise dimensions of the geometry, in combination with the controlled environment during sample loading.

The research objective in this chapter is to quantitatively analyze the kinetics of phase separation processes that occur during the spinning of hollow fiber membranes. In a typical setup, two types of phase separation take place simultaneously: dry-wet phase separation and wet phase separation.

Dry-wet phase separation occurs at the outer wall of hollow fibers, the dry phase being induced by contact with atmospheric moisture or solvent evaporation, and the subsequent wet phase being induced by the nonsolvent bath. Many researchers have attempted to understand the impact of the evaporation step on final membrane morphology, but the evaporation time in most experimental studies was conducted at relatively long timescales in comparison to the actual residence time of a fiber in the air gap during spinning. Frommer and Messalem [10] confirmed that after longer solvent evaporation times (0.5 min. ~ 1.5 min.), the thickness of the outer macrovoid-free layer at the solution-air interface increases and the rate at which phase separation proceeds is slowed down significantly. However, when the dope solution is exposed to ambient air, humidity is more responsible for the formation of thick layer rather than evaporation, particularly in the confined experimental setup used in their research. More importantly, their results remain questionable for solvent evaporation on short time scales (< 1 s), which is more relevant to the hollow fiber spinning. In this chapter, the effect of solvent evaporation will be tested in shorter timescales, and experimental errors during sample loading will be minimized by using the microfluidic device.

The second relevant type phase of separation that occurs during the spinning process is wet phase separation at the interface between the dope solution and the bore fluid. The ideal morphology at the bore side is the porous structure so that it functions as a mechanical support but not contributes to the separation. The typical bore fluid consists of solvent/nonsolvent but the solvent concentration is maintained fairly high to ensure the phase separation kinetics is very slow and the incompressible bore fluid work as a place holder.

The polymer concentration and the dope viscosity are important factors for successful operation of the fiber spinning process. The polymer concentration in most dopes is kept in the concentrated regime to reduce defect formation and to provide sufficiently high solution viscosity to withstand the drawing tension in the spinning process. Meanwhile, relatively low molecular weight polymers are used, because of the easiness in handling and instrumental limitations (high molecular weight, high viscosity fluids require more energy for pumping). Few literature studies are available on the effect of polymer molecular weight on the kinetics of phase separation and resulting fiber morphology. Peng et al. [12] formulated their Torlon solutions with two different molecular weights and adjusted the viscosity by changing the temperature of the spinneret. Although they found that membranes spun from dope solutions of different polymers with the same viscosity (different temperatures) yield similar gas separation efficiencies, the simultaneous change of several process parameters (temperature, composition, viscosity and molecular weight) makes interpretation of the experimental data more difficult. The experiments in this chapter will focus on the effects of polymer molecular weight variations in an isothermal setting. We will also quantify the kinetics of wet phase separation induced by various non-solvents. By comparing thermodynamic parameters, the kinetics of phase separation, and the resulting morphology, we will develop correlations between these parameters.

2.2. Experimental Setup

2.2.1. Dope preparation and non-solvents

The polymers used in this chapter are polyethersulfone (PES, Veradel®) at four different molecular weights from Solvay Plastics, LLC. and polyetherimide (PEI, Ultem ®1000) from SABIC Innovative Plastics. The estimated molecular weight range of the PES samples was 62-64 kD, 52-55 kD, 42-44 kD, and 35-41 kD, respectively (information supplied by Solvay Plastics). First, PES polymers were dissolved in *N*-Methyl-2-pyrrolidone (NMP). 35 wt% of PES solutions in NMP with four molecular weights were prepared. Also, solutions of 33 wt% of 64 kD, 35 wt% of 53 kD, 39 wt% of 42 kD and 40 wt% of 38 kD PES in NMP were prepared to have the same viscosity of approximately 70 Pa s. Two PEI solutions were made with as solvent and ethanol as a co-solvent: PEI/NMP (30/70 wt%) and PEI/NMP/Ethanol solutions (30/65/5, 30/62.5/7.5, 30/60/10 wt%). All solutions were placed on a slow-roller mixer for about a week to obtain homogeneous solutions. The nonsolvents used in the phase separation experiments were a series of alcohol analogues (methanol, ethanol, isopropanol, 2-butanol, 2-hexanol) and various mixtures of NMP/water (0/100, 20/80, 30/70, 40/60, 50/50, 60/40, 70/30, 80/20, 85/15, and 90/10 wt%).

2.2.2. Viscosity measurements

The shear viscosity of polymer solutions was measured with a rotational rheometer (MCR 300, Anton Paar) at 25 ℃. A Peltier-controlled Couette geometry (inner diameter 10.0 mm and outer diameter 10.84 mm) was used as measuring system in order to minimize effects of interfacial phase separation due to atmospheric humidity.

The range of shear rates in measurements was 1 – 200 s^{-1} and the zero shear plateau of viscosity flow curves was used as the viscosity of the sample.

2.2.3. Fabrication of microfluidic device

The channel mold was fabricated with SU-8 photoresist on a silicon wafer using soft lithography techniques [13]. After printing the channel design drawn by computer aided design (CAD) on a transparency at high spatial resolution, photocurable epoxy (SU-8 photoresist) was used to transfer this channel pattern onto a silicon wafer. Then, a mixture (10:1 ratio) of uncrosslinked polydimethylsiloxane (PDMS) and a curing agent (SYLGARD® 184 silicon elastomer base kit, Dow Corning) was poured onto the patterned silicon wafer mold and cured in an oven at 72 ℃ for 8 hours. The cured PDMS channel was peeled off from the silicon wafer and attached to a microscope slide by oxygen plasma bonding. Finally, the channels were fully cured in the oven at 72 ℃ for two days. A picture of the microfluidic device is shown in **Figure 2.1**. The width and the height of channels used for the measurement of phase separation kinetics were 1500 μm and 50 μm, respectively. Most of the experiments were conducted with this channel, but a part of experiments with PES was performed with larger channel with cross-section of (4000 μm x 300 μm) due to the difficulty in fracturing. It is specified when the larger channel was used.

2.2.4. Experimental procedure

Although all experiments in this chapter were conducted with the microfluidic device depicted in **Figure 2.1**, the device was operated quite differently for wet phase inversion and dry-wet phase inversion. The common features that are shown in **Figure**

2.1: the channels on the left and right were connected to syringe pumps with water and polymer dope solution, respectively. The top channel was used as inlet for the gas flow (either dry N_2 or ethanol-saturated N_2) and the bottom channel was used as gas outlet.

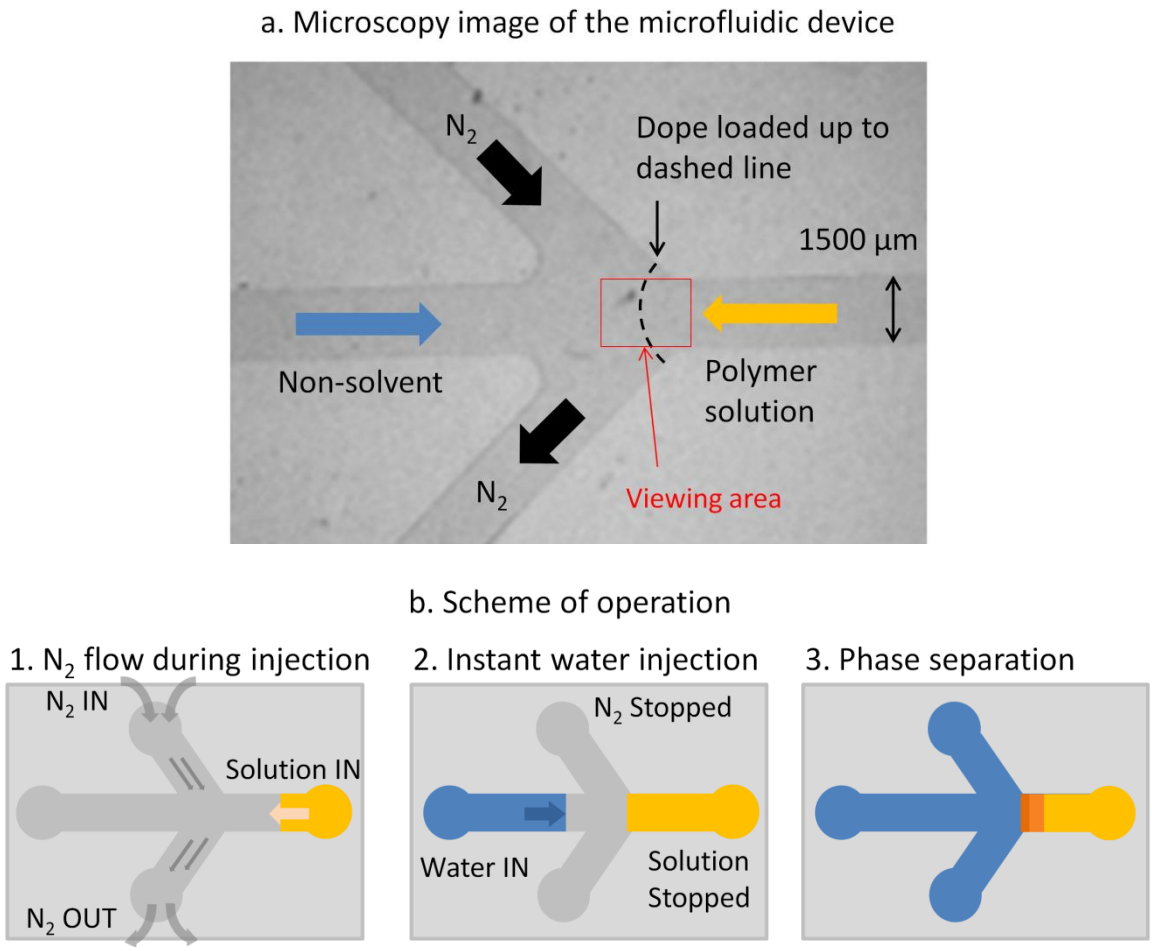

Figure 2.1 a. Microscopy image of the microfluidic device. Top and bottom channels are gas inlet and outlet, respectively, to control the environmental conditioned. b. Scheme of operation (wet phase inversion): polymer solution is loaded through the channel on the right up to the dashed line, while the atmosphere is controlled through gas flow. Finally, nonsolvent is injected through the left channel and brought in contact with the polymer solution to induce phase separation after the gas supply is stopped.

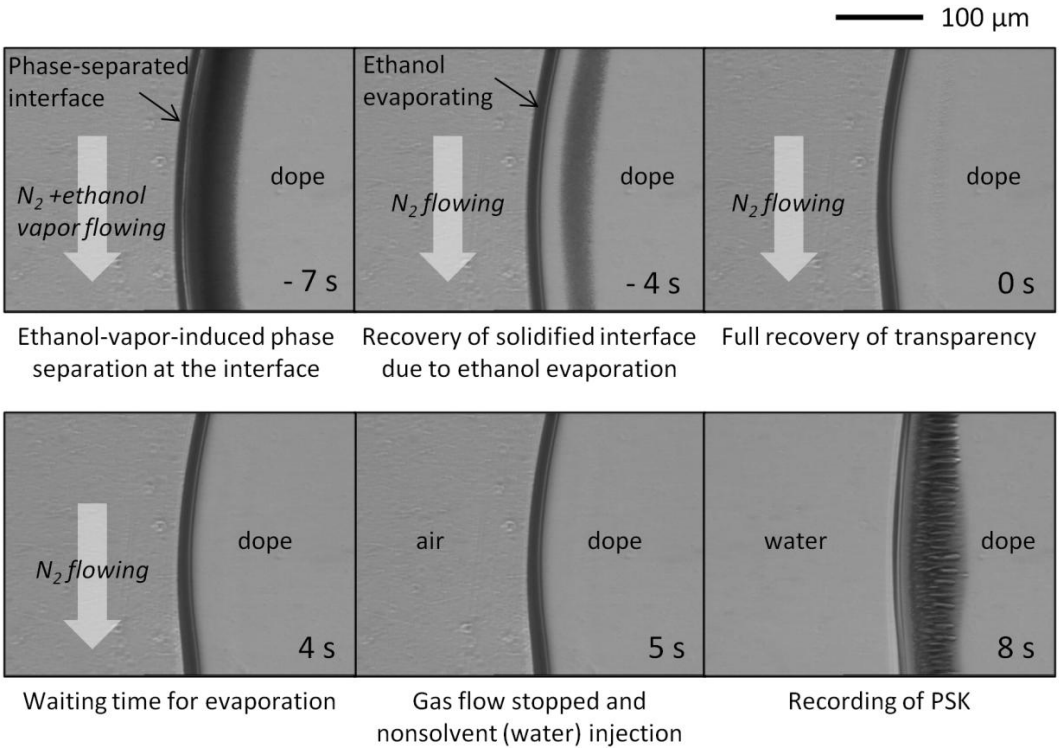

Figure 2.2 Experimental procedure of dry-wet phase separation with PEI/NMP/ethanol (30/60/10) in case of solvent evaporation time of 5 s.

2.2.4.1. Dry-wet phase inversion of PEI with water as non-solvent

PEI/NMP/Ethanol (30/60/10 wt%) was used in the dry-wet phase separation experiments. The detailed experimental procedures are described in **Figure 2.2**. Initially, dry nitrogen gas was flown through the gas inlet to remove any residual moisture from the microchannel. Then, the dry nitrogen gas was replaced with N_2/ethanol vapor mixture during PEI dope injection. After a thin phase-separated layer was generated by the ethanol vapor (-7 s in **Figure 2.2**), the gas flow was switched back to dry nitrogen to remove excess ethanol from the interface of the polymer solution (-4 s). The time at which the solution recovered its original transparency was defined as the initial time t_o (0

s). Finally, after a well-defined waiting period (5 s), during which more ethanol evaporates from the dope, the nitrogen gas flow was stopped and water was injected as nonsolvent to induce phase separation in the dope (8 s).

2.2.4.2. Wet phase inversion of PES with water as non-solvent

In these experiments, dry nitrogen gas was flown through the gas channels during dope injection through the right channel in order to prevent premature phase separation due to residual moisture (**Figure 2.1** b). After the dope solution was loaded into the solution channel, the nitrogen flow was stopped and water was injected immediately to induce phase separation. The experiments were conducted in channels with heights of 50 μm and 300 μm. The measurement of PSK was conducted in the standard channel with cross-section of 300 μm x 50 μm, and the samples for SEM morphology characterization were made by larger channel (4000 μm x 300μm) extraordinary difficulty in fracturing PES polymer.

2.2.4.3. Wet phase inversion of PEI with various non-solvents

For the wet phase inversion experiments with PEI, the general procedure is the same as for PES (section 2.2.4.2) except for the fact that different nonsolvents were used: a series of alcohol analogues (methanol, ethanol, isopropanol, 2-butanol, 2-hexanol) and several mixtures of NMP/water at varying compositions (0/100, 20/80, 30/70, 40/60, 50/50, 60/40, 70/30, 80/20, 85/15, and 90/10 wt%).

2.2.4.4. Fiber extrusion through straight channel with rectangular cross-section

All the solutions were extruded through a slit channel (cross section of 300 μm x 50 μm) to observe the phase separation behavior under conditions that mimic the fiber spinning process more closely. The fabrication process of the device used for these experiments is described in detail in Chapter 3 (see section 3.2.3, 3.2.4, and 3.2.5).

2.2.4.5. Video acquisition with optical microscope and video analysis

The phase separation process was recorded by CCD camera (Cohu 4920 for PEI and Hamamatsu for PES) and an optical microscope (DM-IRB, Leica) with a 10x objective. The phase-separated polymer layer appears dark in the microscope images and the evolution of this layer was monitored and analyzed at randomly chosen five different locations across the channel width as a function of time. For the selected areas, intensity profiles were created by averaging pixel intensities in the transverse direction, perpendicular to the direction of phase separation in every frame of the video, a threshold function was then used to determine the thickness of the dark, phase-separated region. The cut-off pixel brightness value for this threshold was defined as follows:

$$\text{(Cut-off pixel brightness)} = [\text{(max. brightness)} - \text{(min. brightness)}] \times a \quad (2.1)$$

For PEI solutions, the value of a was set to 0.75.

The characteristic optical properties of polyethersulfone (PES) solutions enabled a more detailed analysis, independently tracking the progression of phase separation and macrovoid growth (**Figure 2.3**). When the PES solution was fully phase-separated

(solidified), it appeared dark in the microscope images, while the initially forming macrovoids appeared brighter than the surrounding solution. Since the liquid-liquid demixing occurs heterogeneously, the analysis area was manually picked to contain the demixed droplets (blue-colored area). By using different cut-off pixel brightness values as a threshold, the thicknesses of the phase separated layer (a = 0.2) and preceding bright layer of macrovoids (a = 0.75) were measured.

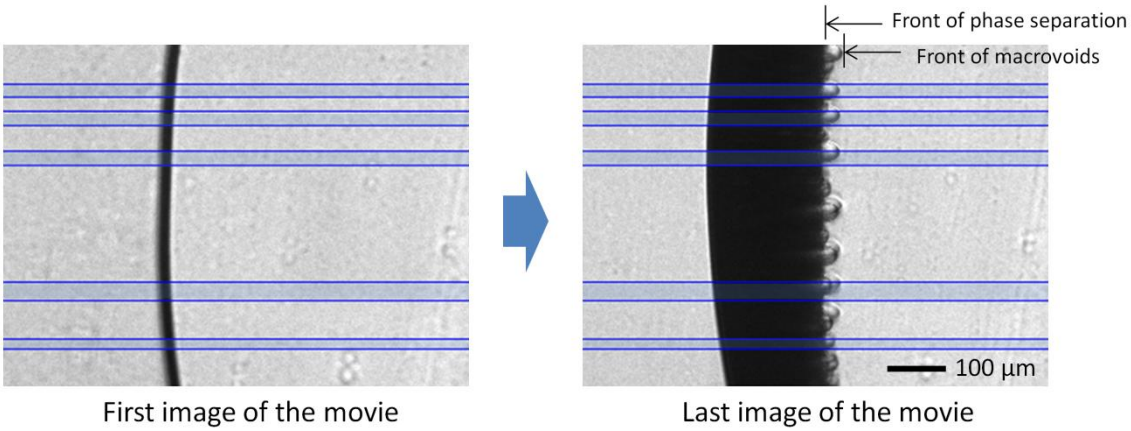

Figure 2.3 Different tracing technique for phase separated layer and macrovoid layer in wet phase separation with PES.

2.2.4.6. Morphology analysis via scanning electron microscope

The microfluidic device with solidified polymer was immersed in a water bath for a day. Then, the solidified polymer strips were removed from the PDMS devices and soaked in a water bath to achieve complete phase separation for two days. After that, they were dried in oven overnight and immersed in liquid nitrogen and snapped immediately using tweezers. Then, the snapped cross-sections were gold-coated with a thickness of

approximately 10 nm with a sputterer (Q150T, Quorum Technologies). Cross-sectional images of the polymers were taken by a scanning electron microscope (LEO 1550).

2.3. Results and Discussion

2.3.1. Dry/wet phase separation: effect of solvent evaporation on PSK

2.3.1.1. Evaporation of volatile solvent in controlled environment

The evolution of water-induced phase separation in PEI/NMP/Ethanol (30/60/10 wt%) is shown in **Figure 2.4** a for different values of the evaporation time. The solution in which phase separation was induced by injecting immediately after the solution recovered its original optical transparency (evaporation time 0 s) showed the fast phase separation rates. We found that PEI/NMP solution become turbid when 15% of ethanol was added (cloud point method), and this critical concentration would be the good estimation of the ethanol concentration at the sample interface when it has just recovered transparency. As more evaporation time was allowed, the phase separation rates slowed down gradually.

The effective diffusion coefficient of phase separation is defined with Equation 1.5 and was presented as a measure of progression speed of phase separation. In dry wet phase separation experiment, the data points at initial stage (~ 1.5 s) were used for the estimation of the effective diffusion coefficient and shown in **Figure 2.4** b. While the effective diffusivity decreases as evaporation time increases, the decreasing rate also decreases. The last data point (evaporation time ∞) is for a PEI/NMP solution with

composition of 33/67, the final composition of the initial sample when all ethanol in the 30/60/10 PEI/NMP/ethanol has evaporated. The error bar was defined with the standard deviation of two measurements for each sample. The fairly large experimental errors are likely the result of uneven solvent evaporation; after the optical transparency was recovered, there was variation in recovery speed in different sites.

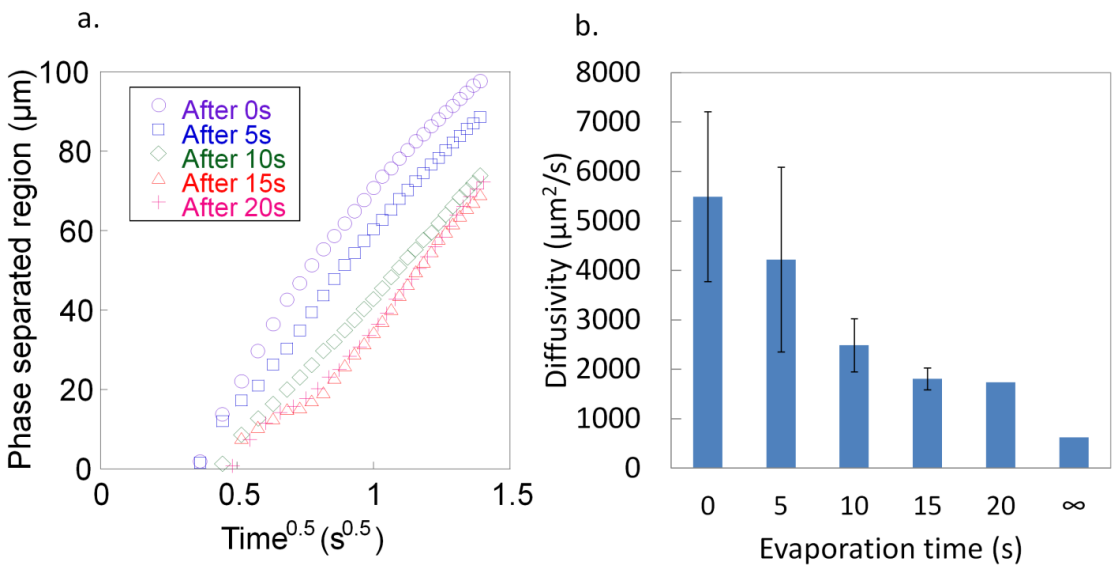

Figure 2.4 Phase separation kinetics of PEI/NMP/ethanol solution (30/60/10 wt%) for various evaporation times. a: evolution of thickness of phase separated region as a function of time, b: effective diffusivity of phase separation.

The resulting morphology of PEI polymer strips formed after different ethanol evaporation times is presented in **Figure 2.5**. **Figure 2.5** a shows the microscopic view of the evolution of phase separation of PEI; images were taken 0.66 s after water injection and after different durations of ethanol evaporation from the sample (0 ~ 20 s). These

microscope images clearly show that the macrovoids are longer and bigger in samples with short evaporation times and that their growth is suppressed by ethanol evaporation, even though ethanol evaporation moves the sample composition further away from the binodal. **Figure 2.5** b shows the corresponding SEM images of the cross-section of the phase-separated fibers, which were cut along the direction of phase separation. Although the macrovoids become smaller and shorter as more solvent evaporation is allowed prior to nonsolvent injection, they were found in all phase separated polymer samples. It should be noted that the effect of macrovoid suppression only appears after a fairly long evaporation time (~ 10 s), and it is therefore not likely that the evaporation of volatile solvents in the air gap of a spinning set-up (< 1 s) affects the dense skin layer formation or macrovoid suppression. The solvent evaporation rate is fairly slow and no layer formation or optical change (turbidity) was observed at the gas/solution interface during the evaporation process. It is important to note, however, that in this microfluidic experimental setup, the humidity of the gas phase was kept low (dry nitrogen saturated with ethanol vapor) during the solvent evaporation. In Chapter 4, it will be discussed which role the air humidity can play during fiber spinning.

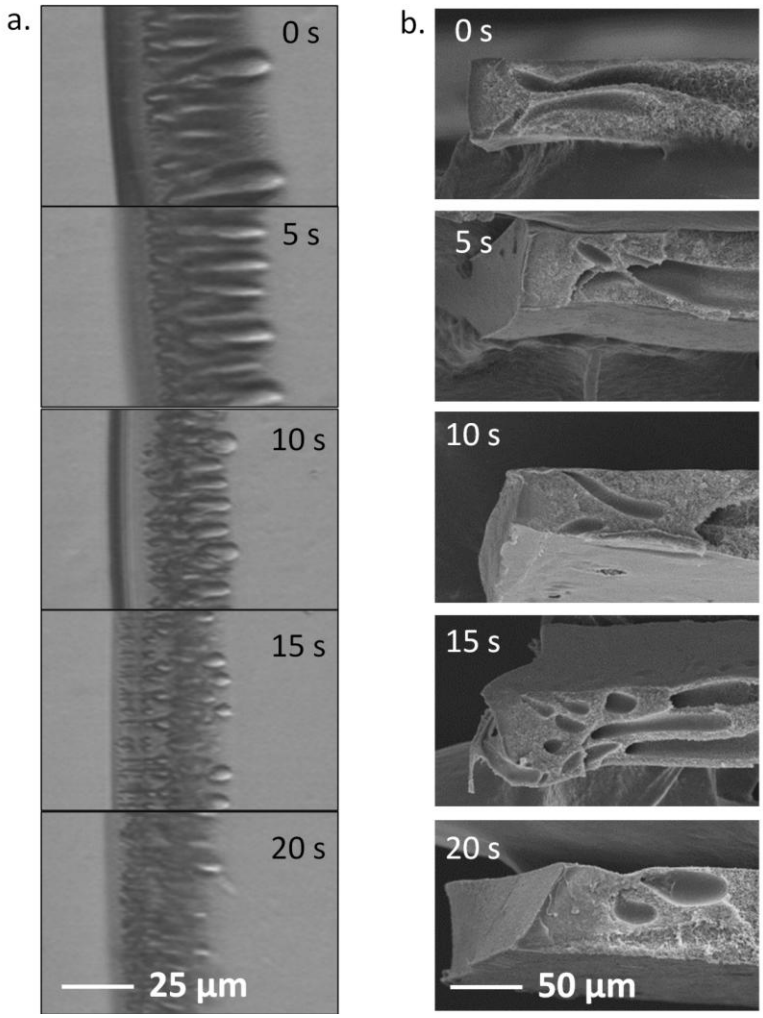

Figure 2.5 a: microscopic view of phase separation of PEI/NMP/ethanol (30/60/10); all images were taken 0.66 s after water injection with variable ethanol evaporation times prior to injection (0-20 s), b: resulting cross-sectional SEM images of PEI polymer strips.

2.3.1.2. Fiber extrusion through a rectangular channel

In order to see how these polymer solutions phase separate after being exposed to flow conditions that can affect the microscopic polymer configuration, wet extrusion experiments were conducted. For this purpose, PEI 30% solutions with 0, 5, 7.5 and 10

wt % ethanol concentrations in NMP were extruded at a shear rate of 150 s^{-1} through a slit die with cross-sectional dimensions of 300 μm x 50 μm directly into a water bath. The extruded polymer strips were collected and prepared for SEM. High magnification images of the cross-sections of these fibers (perpendicular to extrusion direction) are shown in **Figure 2.6**. The rectangular cross-sectional shape of the extruded fibers is an indication that there was no die swell in these samples at this moderate shear and direct extrusion into water (wet phase separation) prevents compositional change of the dope prior to phase separation. As the ethanol concentration in the dope increases, the starting point of macrovoid growth moves further away from the fiber surface. In combination with atmosphere-controlled experiments described in the previous section, this result implies that instead of the evaporation of the ethanol in dope solutions, changes in dope's inherent thermodynamics caused by the addition of ethanol to the dope solution may mostly be responsible for suppression of macrovoid formation. In other words, even without evaporating ethanol, the altered thermodynamics is enough to form macrovoid-free outer layers, which is where the separation properties are defined for hollow fiber membranes.

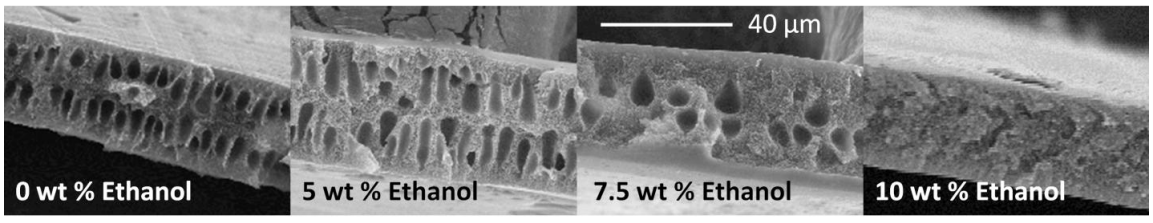

Figure 2.6 Macrovoid-free outer layer evolution in PEI solution with different ethanol concentration. Fibers were extruded at a shear rate of 150 s^{-1}.

2.3.2. Wet phase separation: effect of polymer molecular weight on phase separation

The goal of research in this section is to investigate the effects of molecular parameters (e.g. molecular weight) and bulk dope properties (e.g. viscosity and concentration) on the phase separation kinetics. Characteristic optical properties of PES made progression of phase separation and macrovoid growth distinguishable and using different molecular weight polymer decoupled the effects of molecular parameter from bulk dope properties.

2.3.2.1. Effect of MW in solutions with same concentration

The evolution of thicknesses of phase separation (PS) layer and macrovoid growth (MG) layer in 38 kD 35 wt% PES solution is shown in **Figure 2.7** a, as an example of a typical data set. The plots consist of thousand data points for each sample but only 15 interpolated data points are shown. While the PS layer growth is approximately proportional to the square root of time over the entire range of time scales, large fluctuations are found in the MG rate. After the macrovoids quickly grow up to 40 μm, their expansion was paused until the general PS layer caught up, probably due to insufficient supply of the nonsolvent to sustain macrovoid growth. From that point on, macrovoids evolve at a similar rate as the overall phase separation, albeit slightly faster.

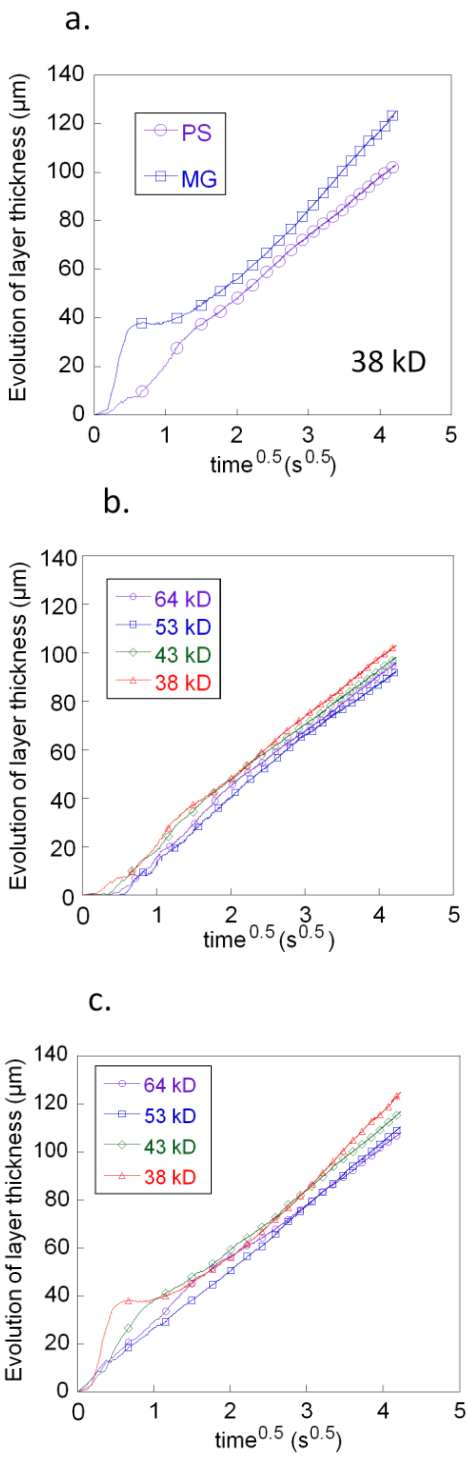

Figure 2.7 Evolution of layer thickness in PES solutions as a function of square root of time a: layers of complete phase separation and of macrovoids in PES 38 kD solution, b: layer of complete phase separation, c: layer of macrovoids.

These results agree with the data from literature. Independent research groups have reported that the phase separation [14-16] and macrovoid growth [8] are proportional to the square root of the elapsed time, which means that an effective diffusion coefficient can be used to quantify these processes (Equation 1.5). Our observation that the macrovoids grow faster than the proceeding of phase separation is also in a good agreement with previous research [8].

In solutions with the same polymer concentration, polymers with different molecular weights have different degrees of polymer chain entanglement; as a result, the viscosities of these solutions are not constant, as shown in **Table 2.1**. The evolution of phase separation and macrovoid growth in PES 35 wt% solutions with different molecular weights were monitored and the results are plotted in **Figure 2.7** b and c. As other researchers have observed, the thickness of phase separated layer increases linearly along with square root of time. Surprisingly, despite the differences in molecular weight and viscosity, the effective diffusion coefficients of the phase separation front in solutions at constant polymer concentration were constant within experimental errors (**Figure 2.8** a). The fact that a constant effective diffusivity of phase separation was found in these same solutions can be explained by the fact that the mesh size in these solutions is the key parameter that determines the hindrance effect that nonsolvent (water) and solvent (NMP) molecules experience when they diffuse through the solution. According to the De Gennes scaling theory, the characteristic blob size (mesh size) of unperturbed polymer molecules is independent of polymer chain length in highly concentrated polymer solutions [17], but only depends on the density of polymer chains in solution (i.e. overall concentration).

Table 2.1 PES concentration and viscosities of solutions that were prepared to obtain a: same concentration, b: same sample viscosity

a. same concentration	64 kD	53 kD	43 kD	38 kD
Polymer (wt%) in NMP	35	35	35	35
Viscosity (Pa·s)	128	80.8	23.4	19.9
b. same viscosity	**64 kD**	**53 kD**	**43 kD**	**38 kD**
Polymer (wt%) in NMP	33	35	39	40
Viscosity (Pa·s)	70.0	80.8	68.5	73

In this study, we only used the initial macrovoid growth rate, which is more relevant to the macrovoids formed near the interface, which are of interest. The rate of macrovoid growth (MG) in these solutions is, however, very different. Large variations were found in initial MG rates in solutions with identical concentrations (**Figure 2.8** a). By comparing the dope viscosity in **Table 2.1** a and the effective MG diffusivity in **Figure 2.8** a, it is clear that in low viscosity samples, the macrovoids grow faster than in the high viscosity samples.

Images at the left hand side in **Figure 2.9** shows SEM images of the resulting morphology of polymer strips formed from these PES solutions with different MW at the fixed concentration of 35%. Although the overall phase separation kinetics is very similar, the macrovoid formation is clearly affected by MW (or viscosity). The lowest viscosity solution contains the largest macrovoids (bottom left in **Figure 2.9**), whereas the highest viscosity solution contains the smallest, shortest macrovoids (top left in **Figure 2.9**).

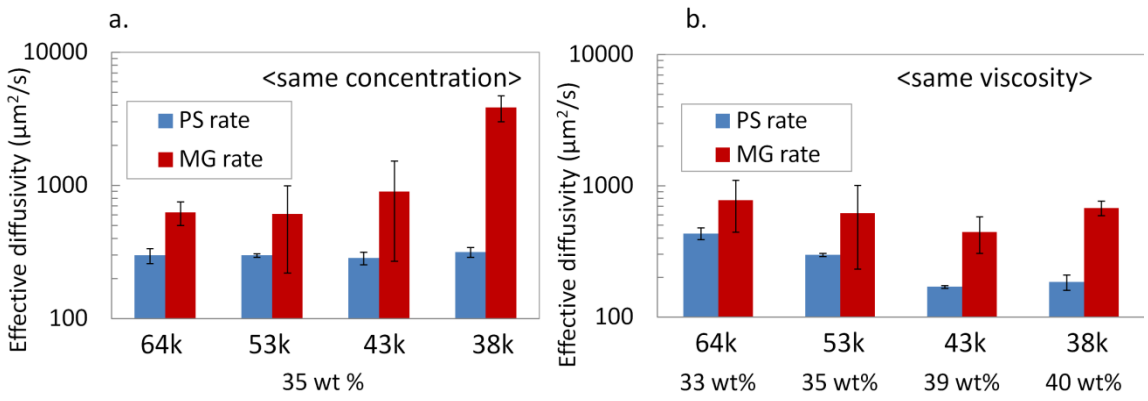

Figure 2.8 Effective diffusivity of phase separation in a: PES solutions at 35% and b: PES solutions with similar viscosity but different concentrations.

The dependence of macrovoid growth rate on macroscopic (viscosity) rather than microscopic (polymer mesh size) properties of the samples can be explained by the length scale of the process. In our observation, liquid-state macrovoids form and proceed into the solution before overall phase separation occurs. In other words, liquid-liquid demixing occurs before the phase separation forms solid membrane structure. In this heterogeneous, two-phase liquid mixture (liquid in macrovoids and dope solution), the convective expansion of macrovoids should be hindered by the bulk viscosity of the dope solution. In the solutions at constant PES concentration, high MW samples have a higher viscosity due to a larger degree of chain entanglement.

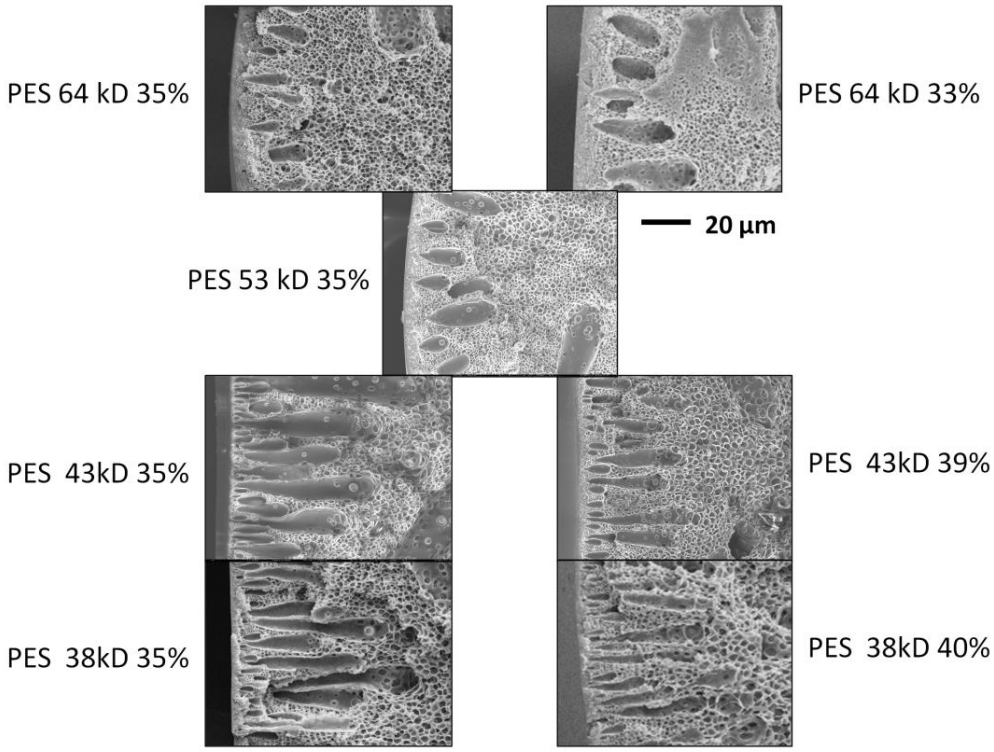

Figure 2.9 Cross-sectional SEM images of phase separated PES polymer, cut in the direction of water injection.

2.3.2.2. Effect of MW in solutions with same bulk viscosity

To further investigate the observations of the previous section, PES solutions were also prepared with similar viscosities at different MW by adjusting the polymer concentrations. The target viscosity was around 70 Pa s, and the actual viscosities and compositions are shown in **Table 2.1** b; because viscosity varies very strongly as a function of concentration, it was not easy to obtain perfectly matched viscosities, but the values we achieved are sufficiently close to limit viscosity effects. The range of polymer concentrations was 33-40%, 33 wt% for the longest polymer and 40 wt% for the shortest polymer. The effective diffusion coefficients of phase separation and macrovoid growth

for these solutions are shown in **Figure 2.8** b**.** As the polymer concentration increases, the PS rate decreases. In PES 43 kD solution, the PS rate seemed a little slower than in PES 38 kD, but this can be regarded as experimental error, since the phase separation in these two samples are too slow, compared to other samples. The effective diffusion coefficients of macrovoid growth in all samples were roughly 750 $\mu m^2/s$, constant within experimental errors.

Although various researchers have claimed that increasing the polymer concentration in the dope solutions slows down the phase separation and suppresses macrovoid formation [8, 10, 18], our data clearly shows that the overall phase separation rate is solely determined by the microstructure of the polymer solution (characteristic mesh size), while the macrovoid growth rate and the macrovoid size are influenced mainly by the bulk viscosity of the polymer solution, which determines the resistance against bulk flow. In **Figure 2.9**, the number and the length of the macrovoids increased as polymer MW decreased, even in more concentrated solutions. This indicates that the growth of heterogeneous liquid-liquid demixed regions can occur even in very concentrated solutions, as long as the viscosity is sufficiently low.

As can be seen in **Figure 2.9**, the porosity of the resulting polymer strips increases with decreasing polymer MW, although PES 38 kD has the highest polymer concentration. Porosity of the phase separated polymer depends on the phase separation rate regardless of polymer concentration.

2.3.2.3. PES fibers extruded from rectangular channel

The effect of differences in phase separation rate on polymer morphology becomes even more prominent in flowing conditions. The cross-sectional area of extruded polymer fibers of PES 64kD (33 wt%), and PES 38kD (40 wt%) are shown in **Figure 2.10**. In both fibers, the vertical dimension of the fibers expanded as the applied shear increased. The fibers of 38kD become more round at high shear. Even subtle differences in phase separation rate (433 versus 185 $\mu m/s^2$) can allow more time for die swell to occur and change the dimensions of the fibers. The results show that a slower phase separation rate can be a problem in actual spinning process and the choice of MW is as important as other material parameters.

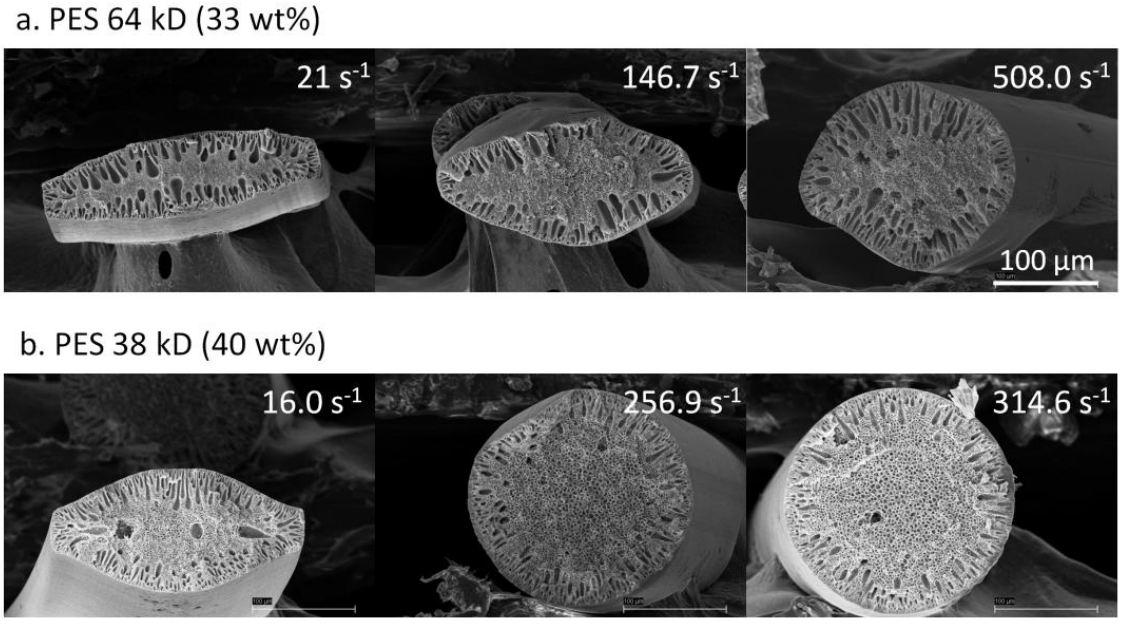

Figure 2.10 Extrusion of two PES solutions with similar viscosity but different molecular weight a: PES 64 kD (33 wt%) b: PES 38 kD (40 wt%).

2.3.3. Wet phase separation: effects of nonsolvents

2.3.3.1. Solubility parameter differences

As discussed in Chapter 1, Hansen solubility parameters are widely used for determining the choice of polymer, solvent, and nonsolvents. Hansen solubility parameters (dispersive (δ_d), polar (δ_p), and hydrogen bonding (δ_h)), molar volume, and surface tension for various pure nonsolvents are obtained from available literature [19], and shown in **Table 2.2**. The solubility parameter of polyetherimide (PEI) was calculated by group contributions [20]. The Hansen solubility parameters for NMP/water mixtures were calculated by using volume fraction of each component, as following [21].

$$\delta_{12} = \delta_1\phi_1 + \delta_2\phi_2 \qquad (2.2)$$

δ is a solubility parameter and ϕ is volume fraction of each species. Subscript 1 and 2 represents component 1 and 2. The molar volume of NMP/water mixtures were calculated similarly, considering volume fraction contribution from each solvent [22]. Solubility parameter differences (Δδ) between nonsolvent and PEI were calculated by Equation 1.4. The surface tension is at 25 ℃.

Table 2.2 Hansen solubility parameter, solubility parameter difference between PEI and various nonsolvents, molar volume, surface tension of solvent and various nonsolvents [19].

	δ_{Dipole} [$MPa^{0.5}$]	δ_{Polar} [$MPa^{0.5}$]	δ_{Hydro} [$MPa^{0.5}$]	δ_{Total} [$MPa^{0.5}$]	$\Delta\delta$ [$MPa^{0.5}$]	V_m [cm^3]	σ [mJ/m^2]
PEI	21.1	7.4	7.1	23.5	0	-	-
Methanol	15.1	12.3	22.3	29.6	17.06	40.70	22.1
Ethanol	15.8	8.8	19.4	26.5	13.47	58.50	22
IPA	15.8	6.1	16.4	23.6	10.78	76.80	23.3
2-Butanol	15.8	5.7	14.5	22.2	9.26	92.00	22.6
2-Hexanol	15.9	3.3	11.8	20.1	8.12	156.60	27.7
NMP/water							
0/100	15.6	16	42.3	47.8	36.65	18	72.7
20/80	16.08	15.26	35.28	42.84	29.68	33.7	-
30/70	16.32	14.89	31.77	40.36	26.22	41.55	-
40/60	16.56	14.52	28.26	37.88	22.78	49.4	-
50/50	16.8	14.15	24.75	35.4	19.38	57.25	-
60/40	17.04	13.78	21.24	32.92	16.04	65.1	-
70/30	17.28	13.41	17.73	30.44	12.79	72.95	-
80/20	17.52	13.04	14.22	27.96	9.76	80.8	-
85/15	17.64	12.855	12.465	26.72	8.40	84.73	-
90/10	17.76	12.67	10.71	25.48	7.21	88.65	-

2.3.3.1. Effective diffusivity of phase separation

Solubility parameter difference between PEI and alcohol analogues decreases in order of methanol → 2-hexanol, as shown in **Figure 2.11** a. It shows the solubility of PEI polymer in various nonsolvent i.e. PEI does not dissolve in methanol but is more likely to dissolve in 2-hexanol. Similarly, solubility parameter different between PEI and mixtures of NMP/water also decreased as the NMP concentration increased in the mixture, because the PEI is more favorable to higher NMP concentrated mixture.

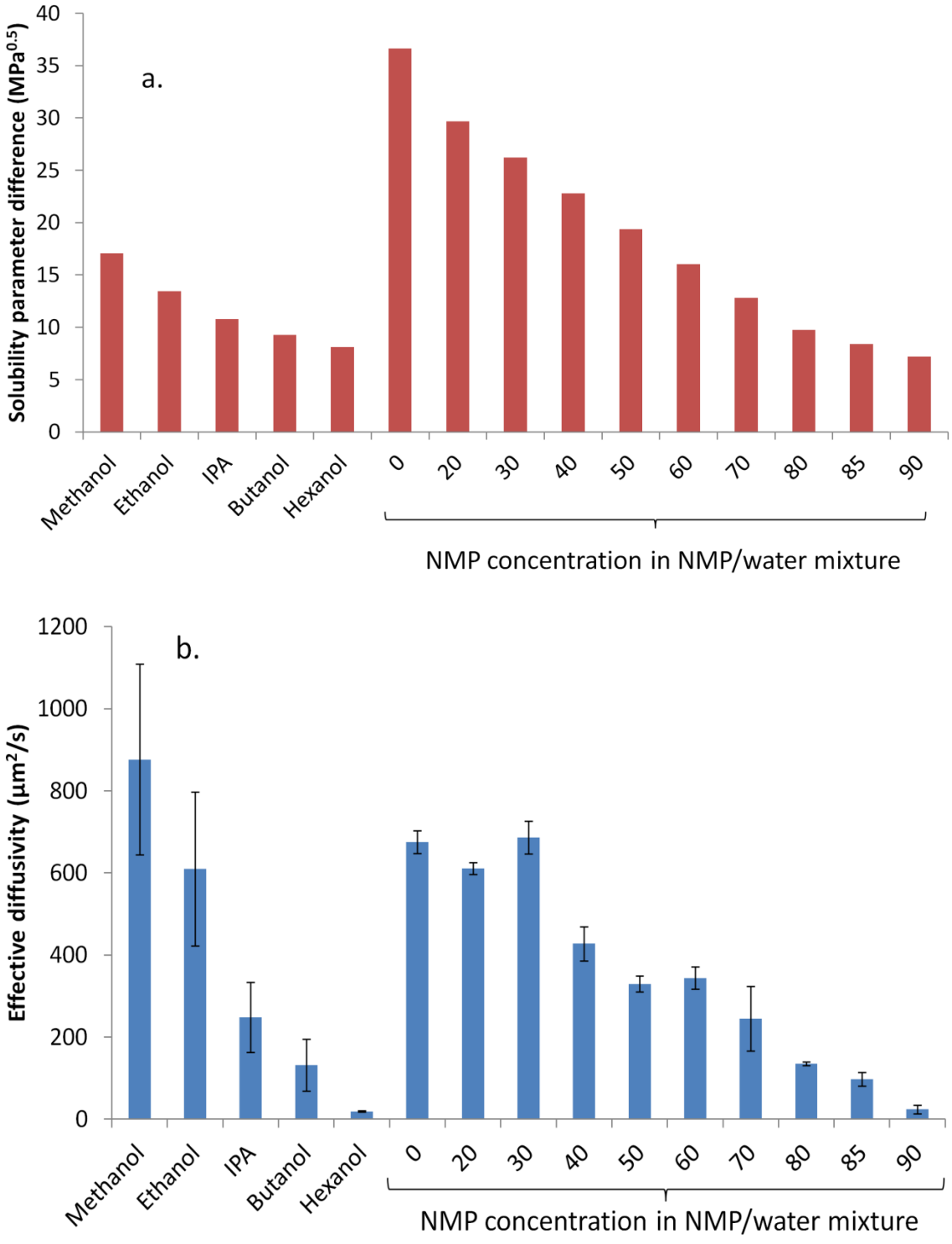

Figure 2.11 Comparison of a: solubility parameter difference and b: effective diffusivity of phase separation of PEI/NMP (30/70) solution and various nonsolvents.

Wet phase separation was induced by various nonsolvents, listed in **Table 2.2** and the effective diffusivity, obtained by tracking the thickness of the phase separated layer, is plotted in **Figure 2.11** b. The effective diffusivity of phase separation decreased as the solubility parameter difference between PEI and nonsolvent decreased. The hypothesis is that during phase separation the nonsolvent molecules invade into PEI solution and the nonsolvent contact both polymer molecules and NMP solvent molecules. If the nonsolvent molecules have high affinity with polymer molecules (low $\Delta\delta$), it takes more time for nonsolvent to penetrate further into the solution. As a result, the phase separation is likely to be delayed. In addition to the phase separation kinetics based on microscopy images, SEM images were also obtained for the cross-sections of the polymer strips that were formed in this process; the fibers were cut along the direction of nonsolvent penetration. **Figure 2.12** a presents optical microscopy images for the various alcohols; these images were all obtained once the thickness of the phase separated layer had grown to roughly ~60 μm. **Figure 2.12** b shows the resulting polymer morphology. Slow phase separation induced a coarse structure (big pore sizes), and macrovoid formation was also suppressed in such samples. In the case of 2-hexanol, the phase-separated polymer is deformed due to the very slow phase separation rates in this sample.

Figure 2.13 shows the morphology of polymer that is formed through phase separation induced by NMP/water mixtures with different compositions. Higher NMP concentrations in the nonsolvent mixture lead to more porous structures. Interestingly, macrovoids were found even when phase separation was induced by nonsolvents containing quite a lot of NMP (NMP concentrations of 80, and 85 wt%).

Effective diffusion coefficients of phase separation for both the NMP/water mixtures and alcohol analogues were plotted as a function of Hansen solubility parameter differences (between PEI polymer and nonsolvents) in **Figure 2.14**. Linear correlations were found for both data sets, but the correlation coefficient was different between the sets. This discrepancy likely results from the molar volume or the size of the molecules. Since the phase separation process can be assumed as a diffusion process of nonsolvent molecules, the molar volume or the size of the nonsolvent molecules as well as interfacial properties cannot be ignored.

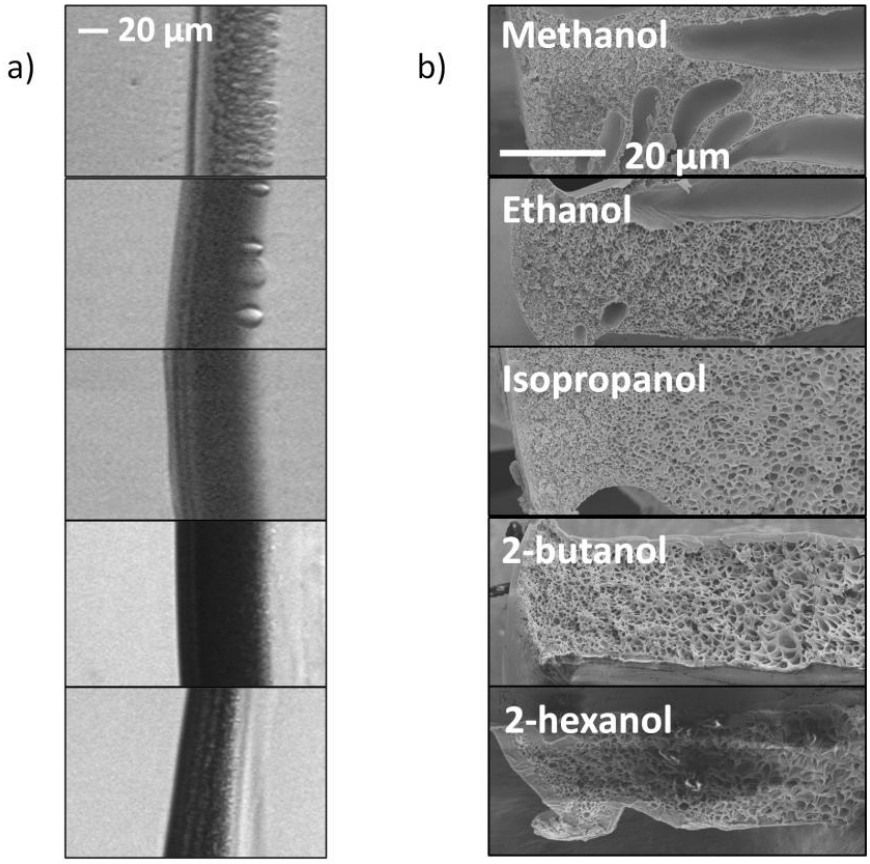

Figure 2.12 a) Microscopic view of phase separated PEI polymer induced by various alcohol analogues, b) resulting cross-sectional images of solidified PEI polymer.

The formation of macrovoids seemed uncorrelated with phase separation kinetics: isopropanol and an NMP/water mixture with 80/20 wt% have similar solubility parameter difference, diffusivity, and morphology, but macrovoids are formed with the mixture of NMP/water (80/20) and not with isopropanol (**Figure 2.12** and **Figure 2.13**). Extrusion experiments could not be carried out with some of the nonsolvents due to too slow phase separation.

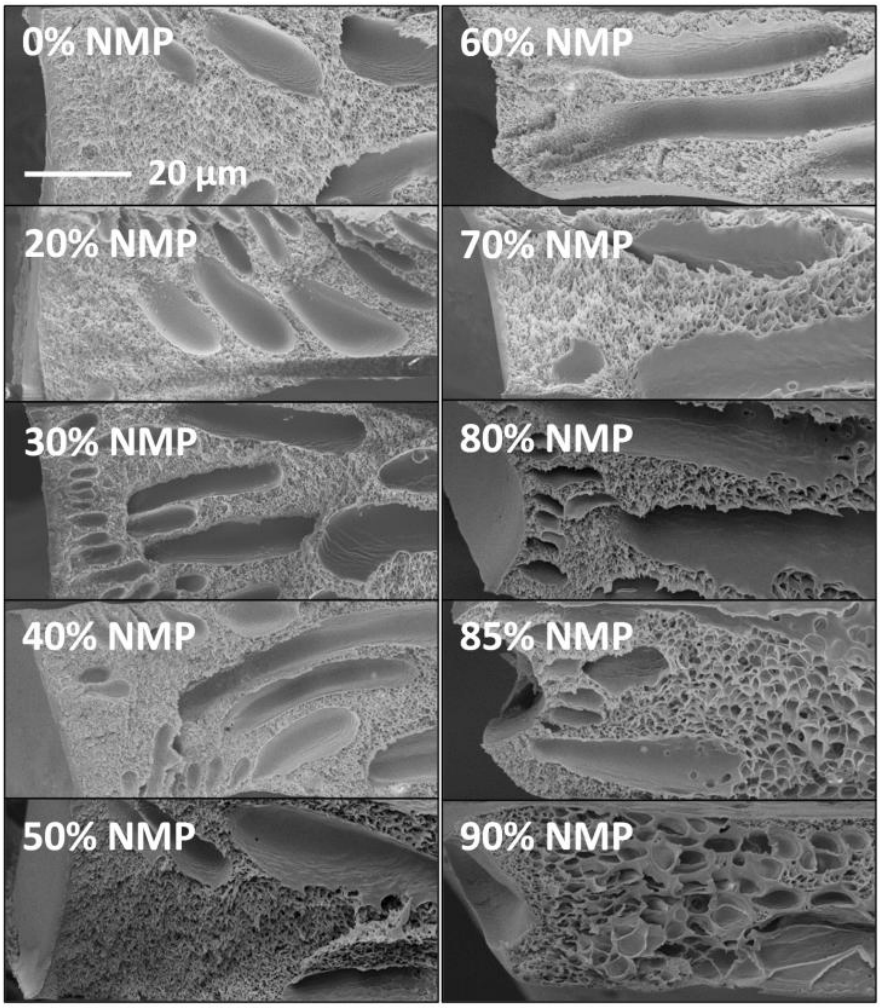

Figure 2.13 Cross-sectional images of the phase separated PEI polymer, induced by NMP/water mixtures as nonsolvents.

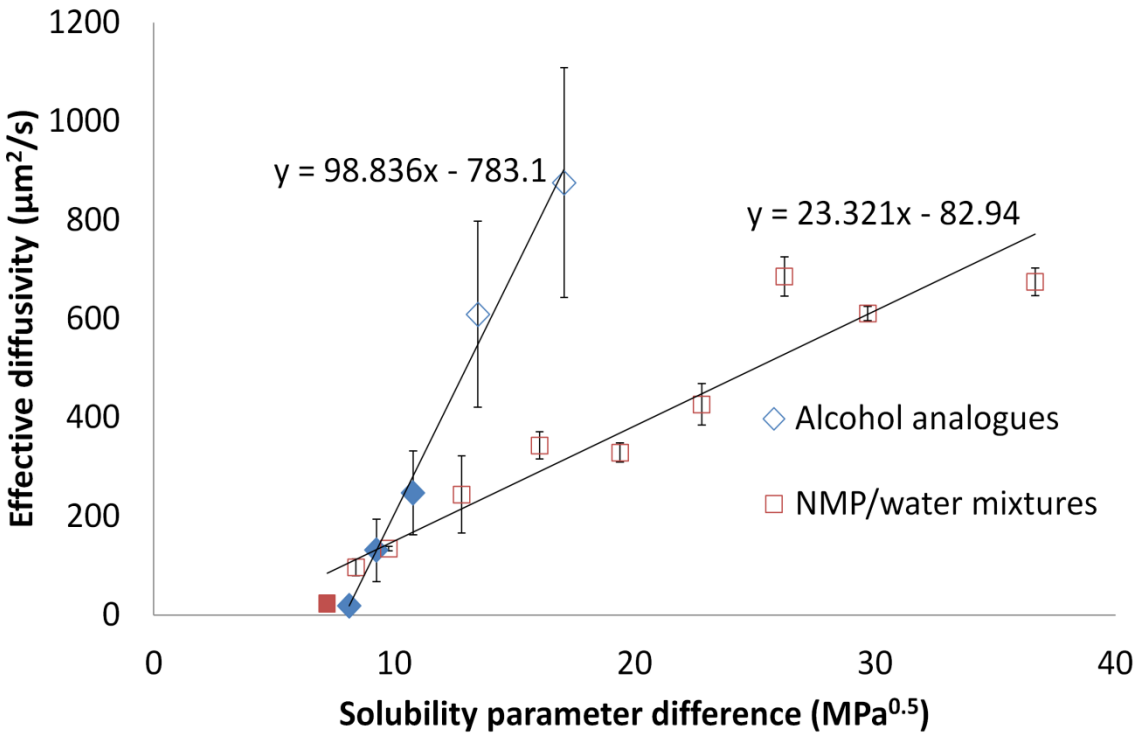

Figure 2.14 Correlation between the solubility parameter difference and effective diffusivity of phase separation of a 30% PEI solution and various non-solvents (hollow symbols: samples with macrovoid defects, solid symbols: samples without macrovoid defects).

2.4. Conclusions

Microfluidic devices offer a controlled experimental environment with outstanding reproducibility in measuring the kinetics of phase separation for a range of experimental conditions. The kinetics of dry-wet phase separation and wet phase separation were measured quantitatively. The effect of co-solvent evaporation time was tested on shorter timescale (evaporation times as short as 5 s) than in any other literature study and the phase separation rate was found to decrease as more time is allowed for

evaporation. However, macrovoid defect formation could not be suppressed completely even after long co-solvent evaporation times when the air humidity was kept minimal. The effect of polymer molecular weight on phase separation kinetics and macrovoid formation was also investigated and it was found that the phase separation rates are determined by the polymer concentration regardless of polymer molecular weight. On the other hand, the macrovoid growth rate is mostly affected by the bulk viscosity of the fluids, and therefore very sensitive to both polymer concentration and molecular weight.

Delayed phase separation was achieved by using various nonsolvents that have a variety of solubility including NMP/water mixtures with different composition ratio. The comparison was made between the diffusion coefficient of phase separation, and solubility parameter difference and linear correlation was found between them. The discrepancy is likely result from the different interfacial properties and the size molecules.

The cross-sectional images of the resulting solidified polymer showed that the polymer porosity is affected by the diffusion coefficient (and thus by thermodynamic parameters), but that the formation of macrovoids is uncorrelated. Even for cases with the same solubility parameter difference and the same effective phase separation diffusivity, one nonsolvent (isopropanol) does not create macrovoids, while the other (80/20 NMP/water mixture) does.

Fiber extrusion experiments showed how differences in phase separation kinetics can affect the morphology of extruded fibers. If phase separation rate is fast, the fibers extruded from rectangular channel will more closely resemble the shape of the rectangular channel cross-section. However, if the phase separation rate is not fast enough, fibers have time to deform after exiting the channel and the shape of the fiber

become very irregular and even change from rectangular to circular, due to die swell (normal stress) effects.

2.5.References

[1] S. Loeb, S. Sourirajan, Sea water demineralization by means of an osmotic membrane, ACS Publications, 1962.

[2] A.J. Reuvers, C.A. Smolders, Formation of membranes by means of immersion precipitation : Part II. the mechanism of formation of membranes prepared from the system cellulose acetate-acetone-water, Journal of Membrane Science, 34 (1987) 67-86.

[3] P.S.T. Machado, A.C. Habert, C.P. Borges, Membrane formation mechanism based on precipitation kinetics and membrane morphology: flat and hollow fiber polysulfone membranes, Journal of Membrane Science, 155 (1999) 171-183.

[4] S.H. Yoo, J.H. Kim, J.Y. Jho, J. Won, Y.S. Kang, Influence of the addition of PVP on the morphology of asymmetric polyimide phase inversion membranes: effect of PVP molecular weight, Journal of Membrane Science, 236 (2004) 203-207.

[5] I. Pinnau, W.J. Koros, Structures and gas separation properties of asymmetric polysulfone membranes made by dry, wet, and dry/wet phase inversion, Journal of Applied Polymer Science, 43 (1991) 1491-1502.

[6] R. Matz, The structure of cellulose acetate membranes 1. The development of porous structures in anisotropic membranes, Desalination, 10 (1972) 1-15.

[7] M.R. Pekny, J. Zartman, W.B. Krantz, A.R. Greenberg, P. Todd, Flow-visualization during macrovoid pore formation in dry-cast cellulose acetate membranes, Journal of Membrane Science, 211 (2003) 71-90.

[8] G.R. Guillen, G.Z. Ramon, H.P. Kavehpour, R.B. Kaner, E.M.V. Hoek, Direct microscopic observation of membrane formation by nonsolvent induced phase separation, Journal of Membrane Science, 431 (2013) 212-220.

[9] D.-M. Wang, F.-C. Lin, T.-T. Wu, J.-Y. Lai, Formation mechanism of the macrovoids induced by surfactant additives, Journal of Membrane Science, 142 (1998) 191-204.

[10] M.A. Frommer, R.M. Messalem, Mechanism of membrane formation. VI. Convective flows and large void formation during membrane precipitation, Industrial & Engineering Chemistry Product Research and Development, 12 (1973) 328-333.

[11] K.O. Olanrewaju, The rheology and phase separation kinetics of mixed-matrix membrane dopes, in, Georgia Institute of Technology, 2011.

[12] N. Peng, T. Chung, J. Lai, The rheology of Torlon® solutions and its role in the formation of ultra-thin defect-free Torlon® hollow fiber membranes for gas separation, Journal of Membrane Science, 326 (2009) 608-617.

[13] J.C. McDonald, D.C. Duffy, J.R. Anderson, D.T. Chiu, H. Wu, O.J.A. Schueller, G.M. Whitesides, Fabrication of microfluidic systems in poly(dimethylsiloxane), Electrophoresis, 21 (2000) 27-40.

[14] H. Strathmann, K. Kock, P. Amar, R.W. Baker, The formation mechanism of asymmetric membranes, Desalination, 16 (1975) 179-203.

[15] C. Cohen, G.B. Tanny, S. Prager, Diffusion-controlled formation of porous structures in ternary polymer systems, Journal of Polymer Science: Polymer Physics Edition, 17 (1979) 477-489.

[16] S.K. Yong, J.K. Hyo, Y.K. Un, Asymmetric membrane formation via immersion precipitation method. I. Kinetic effect, Journal of Membrane Science, 60 (1987) 219-232.

[17] P.G. De Gennes, Dynamics of entangled polymer solutions. I. The Rouse model, Macromolecules, 9 (1976) 587-593.

[18] M.R. Kosuri, W.J. Koros, Defect-free asymmetric hollow fiber membranes from Torlon®, a polyamide–imide polymer, for high-pressure CO2 separations, Journal of Membrane Science, 320 (2008) 65-72.

[19] Diversified Enterprises, Surface tension, Hansen solubility parameters, molar volume, enthalpy of evaporation, and molecular weight of selected liquids, http://www.accudynetest.com/solubility_table.html.

[20] D.W. Van Krevelen, K. Te Nijenhuis, Properties of polymers: their correlation with chemical structure; their numerical estimation and prediction from additive group contributions, Elsevier, 2009.

[21] A.F. Barton, Solubility parameters, Chemical Reviews, 75 (1975) 731-753.

[22] J. Thimmasetty, C. Subramanyam, B. Vishwanath, P. Satesh Sabu, Solubility parameter estimation of celecoxib by current methods, Asian J Res Chem, 2 (2009) 188-195.

CHAPTER 3

IN SITU OBSERVATION OF PHASE SEPARATION AND MORPHOLOGY OF POLYMERIC MEMBRANE DOPES IN SHEAR AND ELONGATIONAL FLOW

3.1.Introduction

Controlling the formation of macrovoids during hollow fiber membrane spinning is challenging because of the complexity of the process: The spinning process involves coextrusion of a homogeneous, viscous polymer solution (dope) through an annular spinneret, and a bore fluid inside. The polymeric dopes can either be extruded into air (dry phase separation), directly into a non-solvent bath (wet phase separation), or first into air and then after a well-defined distance (air gap) into a non-solvent (dry-wet phase separation); in all cases, solvent is removed from the dope to initiate phase separation. Macrovoid defects are typically formed during this phase separation step, when the liquid-state solution transforms into a solid membrane. As discussed in Chapters 1 and 2, the phase separation process usually determines critical elements of the membrane morphology, including the thickness of the dense outer skin layer that defines most of the separation characteristics of the membrane.

The formation mechanism of macrovoid defects in polymeric dopes has been studied extensively. Although no universal theory has been developed so far, many hypotheses have been suggested with regards to potential driving forces for macrovoid

formation, including surface-tension-induced interfacial instabilities [1], concentration-gradient-induced interfacial instabilities [2], formation of convective flows [3], spinodal decomposition [4], and osmotic pressure [5]. We will not discuss these hypotheses here in more detail; reviewing the literature on the origin of macrovoid defects is beyond the scope of this study and thorough descriptions and discussions of limitations of the various hypotheses are available [6, 7]. From a practical viewpoint, the main objective in prior research has mostly been to avoid or circumvent macrovoid formation, rather than fully understanding the process.

One common approach to suppress macrovoid formation is by fine tuning the solution composition. Researchers have found that the occurrence of macrovoids can be reduced by increasing the polymer concentration [3, 8, 9], adding surfactants to the solution [10], adding nonsolvent to the dope solution [3], inducing solvent evaporation from the dope solution in the air gap after extrusion [11, 12], adding polymeric additives to the solution [13, 14], using solvents for the dope with lower affinity to the nonsolvent in the phase separation bath [3, 15], and adding solvent to the nonsolvent bath [9]. Although the fundamentals of the formation mechanism are still open to speculation, these methods all attempt to counteract previously suggested driving forces. For example, adding surfactants to the dope changes interfacial properties of the dope, and using dope solvents with a lower affinity to the nonsolvent in the quench bath reduces the initial mass transfer rate of nonsolvent into the dope by decreasing osmotic pressure. Often, a combination of the methods listed above is used to suppress macrovoids in fiber spinning processes.

Aside from the compositional parameters of the spinning dope and nonsolvent bath, the morphology of membranes can be modified by optimizing spinning parameters like the draw ratio and the dimensions of the spinneret from which the fibers are extruded. A summary of the effect of various spinning parameters on hollow fiber membrane properties is provided in Chapter 1 (**Table 1.1**). For example, it has been found empirically that macrovoid formation can be suppressed by utilizing high draw ratios in hollow fiber membrane spinning [6, 16]. In these studies, researchers purposely changed the draw ratio across a large range of values and found that as they increased the draw ratio, the resulting fibers gradually contained fewer macrovoids. In general, however, it must be pointed out that systematically varying process parameters in a spinning process is more challenging than adjusting the dope composition, since many processing parameters are coupled and cannot easily be adjusted independently. In the previously mentioned studies that examined the effect of draw ratios [6, 16], for example, dramatic dimensional changes of the polymer fibers occurred in the air gap as well. As a result, membranes spun at higher draw ratios have smaller dimensions, and thinner membranes are known to inherently have fewer macrovoids, both in flat sheet and hollow fiber membrane geometries [17-19]. Specifically, Ren and coworkers [17] found that PEI (polyetherimide) membranes with thicknesses smaller than 10 μm contained no macrovoids and formed a sponge-like substructure; above this critical thickness, macrovoids were detected. It is therefore unclear if the effect of draw ratio on macrovoid formation is purely the result of dimensional changes, or if the extensional flow itself suppresses macrovoid formation.

Another example of coupled spinning parameters associated with changing draw ratios is the occurrence of minor compositional changes at the outer skin of nascent fibers in the air gap, where elongation takes place. Premature phase separation due to the presence of water vapor near the surface of the water bath has been observed, causing fibers to become turbid before actually entering the nonsolvent bath [20]. Consequently, the resulting fiber is likely to contain fewer macrovoids because the solidified outer layer acts as a transport barrier and hinders the rapid exchange of solvent and nonsolvent once the fiber enters the quench bath. Moreover, if the polymer solution dope contains a volatile co-solvent, evaporation in the air gap tends to produce concentration gradients in the spun filament prior to entering the bath; the resulting fibers have been found to have fewer macrovoids. To our knowledge, decoupling the effects of the various spinning parameters on macrovoid formation has not been attempted, and enhanced understanding of the role of individual parameters on macrovoid formation would help to optimize the spinning process for new membrane dope formulations.

In this study, we developed a new methodology utilizing microfluidics and video-microscopy. Our device provides improved macrovoid defect detection capabilities as it enables *in situ*, high-resolution visualization of steady-state phase separation and macrovoid formation that occur when a polymer solution is exposed to non-solvent. The dimensions of the microfluidic channels were chosen to closely mimic the actual fiber dimensions in a typical spinning process. Experiments with microfluidic device enable us to decouple the effects of flow conditions (shear and extensional flow) from concentration gradients and dimensional changes in the fibers. The new methodology provides extra benefits in the form of direct visualization of macrovoid formation

dynamics. In most reports on the effect of spinning parameters such as air gap distance [19, 21, 22], draw ratio [6, 16], and shear rates in the spinneret [23, 24], the presence of macrovoids in the membranes was revealed only by post-spinning characterization methods of the resulting fibers, usually via cross-sectional imaging by scanning electron microscopy. That approach, however, only provides localized information and does not provide any insights into the macrovoid formation process. Real time observation of membrane formation at steady state will be useful for confirming the validity of the SEM characterization and improve the fundamental understanding of the formation mechanism of macrovoids.

3.2. Experimental setup

3.2.1. Sample preparation

PEI (Polyetherimide, Ultem® 1000; SABIC Innovative Plastics) was chosen as a model polymer. PEI, supplied as a powder, was first oven-dried to remove residual moisture before making solutions, using NMP (*N*-Methyl-2-pyrrolidone, 99%, Sigma Aldrich) as solvent and ethanol (anhydrous, 99%, VWR) as co-solvent. Based on literature reports about fiber spinning from PEI solutions [25, 26], PEI solutions were formulated at three different compositions by weight: PEI/NMP (30/70wt%), PEI/NMP/Ethanol (30/62.5/7.5 wt%), and PEI/NMP/Ethanol (30/60/10 wt%); these samples are referred to as U30N70, U30N62.5E7.5, and U30N60E10, respectively, in this Chapter. After mixing all components, the solutions were placed on a slow roller for about a week to ensure complete dissolution of the PEI into homogeneous solutions.

3.2.2. Rheological characterization

The shear viscosity of polymer solutions at low shear rates (1 - 200 s^{-1}) was measured with a rotational rheometer (MCR 300, Anton Paar). A Peltier-controlled Couette geometry (inner diameter 10.00 mm and outer diameter 10.84 mm) was used as measuring system in order to minimize effects of interfacial phase separation due to atmospheric humidity, which was also suppressed by using a solvent trap. The viscosity of the polymer solutions at high shear rates (>200 s^{-1}) was measured in a capillary rheometer with capillary length of 20 mm and die diameter of 0.5 mm (LCR 7001, Dynisco). All rheological measurements were performed at 25 ℃.

The apparent elongational viscosity was measured with a capillary breakup extensional rheometer (CaBER, Thermo Scientific), using 6 mm sample plates. The initial gap between two plates in which the sample was loaded was set to 3.01 mm and the two plates were instantly separated to the final gap position, which was 15.51 mm. After instantaneous separation of the two plates, the evolution of the mid-point diameter of the liquid thread was monitored and the applicable elongational rate is determined by the viscosity of the sample fluid. For the PEI solutions, the maximum elongational rate was approximately 10 s^{-1}. During the measurements, the sample chamber was purged with dry nitrogen in order to prevent phase separation of the stretched filament due to atmospheric humidity. For samples containing ethanol, the sample chamber was purged with a nitrogen/ethanol vapor mixture to suppress compositional changes due to ethanol evaporation.

3.2.3. Fabrication of microfluidic channels

To generate shear flow, a straight microfluidic channel (length 5 mm) with rectangular cross-section (300 μm x 50 μm) was fabricated, as shown in **Figure 3.1**a. The height of 50 μm was chosen based on several experimental considerations, including the tradeoff between the desire to reduce the thickness for improved visualization of macrovoid formation and the need to allow sufficient space for macrovoids to form. A mold of the microchannel was fabricated via soft-lithography methods [27]. The channel design was drawn by computer aided design (CAD) and it was printed on a transparency at high spatial resolution. The, photocurable epoxy (SU-8 photoresist) was used to transfer this channel pattern onto a silicon wafer. A mixture of uncrosslinked polydimethylsiloxane (PDMS) and a curing agent with 5:1 ratio was poured onto the silicon wafer and cured in an oven overnight. After curing, the PDMS channel was removed from the silicon mold and attached to a flat PDMS piece by oxygen plasma bonding to create a rectangular channel with PDMS walls on all sides. Finally, these PDMS channels were fully cured in the oven at 72 ℃ for two days.

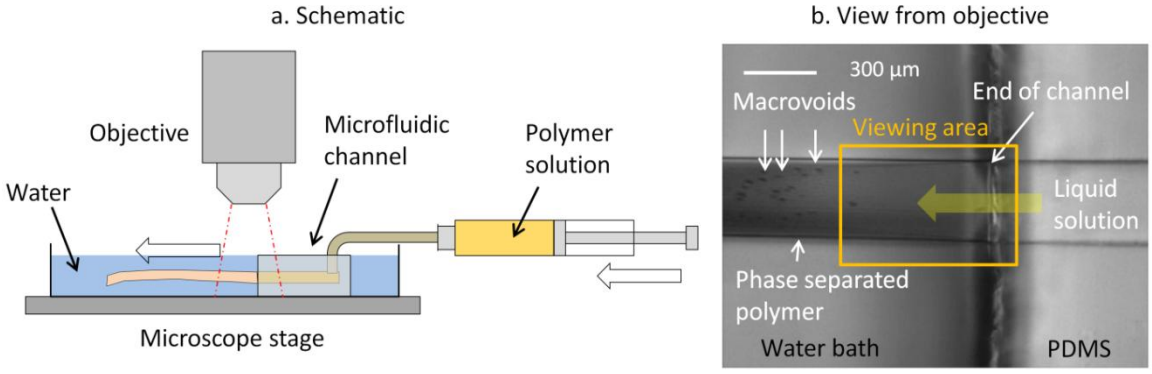

Figure 3.1. Experimental setup. a: Schematic of microfluidic device on a microscope stage b: low magnification view from objective, showing the extraction of the liquid polymer solution from the PDMS device into the water bath.

The pressure drop that is required to generate extensional flow in a microfluidic channel is much larger than for shear flow. Therefore, we could not use the PDMS-based channels, which tend to deform and delaminate at high pressures. Instead, microfluidic channels had to be created from alternative materials for the high-pressure elongational flow experiments. Sollier et al. [28] reviewed the performance of several polymers for their application of rapid prototyping and reported that thermosetting polyester resins (TPE) provide a good alternative to PDMS because of their convenient fabrication, high mechanical strength and moderate optical transparency. Therefore, instead of using PDMS, a hyperbolic contraction channel was prepared with TPE, polyester resin and methyl ethyl ketone (MEK) peroxide as a curing agent (purchased from Fiberglass Supply Depot). The TPE channel fabrication process requires a few more steps in addition to the PDMS channel fabrication process described above. After fabrication of a fully cured PDMS channel, this was used as a stamp to create a positive PDMS mould, which was then used to create a TPE replica of the original PDMS device. Uncured TPE (the mixture of polyester resin and MEK peroxide with a ratio of 10 ml: 0.1 ml) was poured onto the PDMS mould and partially cured, after which the TPE piece was peeled off the PDMS mould and attached to a flat TPE surface to form a channel. Finally, the channel walls inside were coated with Teflon-AF (low refractive index Teflon amorphous fluoropolymers) by filling Teflon-AF solution in the channel and cleaning the residual by blowing dry nitrogen gas to prevent wall swelling and solvent absorption[29].

The channel design was inspired by prior work of Oliveira et al. [30]. The exit dimensions of the contraction channel were kept at 300 μm x 50 μm, the same as for the

shear flow channels, while the entrance measured 2100 μm x 50 μm to generate a 7:1 contraction (Hencky strain $\varepsilon = 2$).

3.2.4. Device operation and acquisition of *in situ* phase separation video

After a dope solution was loaded into a 1 ml syringe at constant uptake rate (0.29 cm/s), 20 cm of tubing was attached to the tip of the syringe and the dope solution was pumped through the tubing and into the microchannel with a syringe pump (KDS210C, KD Scientific). The dope solution was extruded directly from the microchannels into a Petri-dish filled with water, i.e. wet phase separation. The process of extrusion and phase separation at the exit of the microchannel was observed and analyzed by video-microscopy (Cohu 4920 CCD camera with 30Hz sampling rate mounted on an inverted Leica DM-IRB optical microscope with a 10x objective, as illustrated in **Figure 3.1** a. **Figure 3.1** b provides a low-magnification overview of the images obtained for fiber extrusion and phase separation at the exit of one of the straight microchannels. The polymer fiber is extruded from right (PDMS channel) to left (water bath). The liquid polymer solution appears transparent, while phase-separated fibers look darker with droplet-shaped macrovoids. The boxed area marks the viewing area using the 10x objective that was used for video-microscopy, from which snapshots of phase separation videos are presented throughout this Chapter. Polymer solutions were extruded at various flow rates in random sequences to suppress systematic experimental errors. At each flow rate, enough time was allowed for the flow to stabilize before movies were recorded and extruded fibers were collected for further analysis. The wall shear rates were calculated

from the average velocity of the extruded fibers, which was measured manually by analyzing the trajectories of dust particles and other visible impurities in the dope solution in the extrusion video.

3.2.5. Characterization of extruded fibers

Extruded polymer fibers were immersed in water for two days to achieve complete phase separation and then dried overnight in the oven at 75˚C. After being fully dried, the polymer fibers were immersed in liquid nitrogen, snapped and sputter-coated with gold (Q150T, Quorum Technologies, West Sussex, UK). Cross-sectional images of the fibers were taken with a scanning electron microscope (SEM; JEOL JSM-6400 and Zeiss Ultra60 FE-SEM).

3.3.Results and Discussion

3.3.1. Rheological properties of the dope solutions and deformation rate evaluation in rectangular and contraction microchannels

Flow curves were obtained over a broad range of shear rates (1 - 100,000 s^{-1}) by combining the results of viscosity measurements using rotational (1 - 200 s^{-1}) and capillary (200 - 100,000 s^{-1}) rheometers; the results for U30N70 are shown in **Figure 3.2**. Flow curves from the capillary rheometer were adjusted through the Weissenberg-Rabinowitsch correction to correct for non-Newtonian fluid characteristics [31]. All three polymer solutions exhibited similar flow curves, with a Newtonian low shear plateau, followed by shear thinning starting at shear rates near 100 s^{-1}. Flow curves for each

sample were fitted with various models: Newtonian (low shear data points only), power law (high shear data points only), and Carreau viscosity model (Equation 3.1); all data points). The flow curve data and fitted model results for U30N70 are presented in **Figure 3.2**. In most research studies of polymeric membrane dopes reported in literature to date, the rheological properties are quantified either in terms of low-shear Newtonian viscosity, or in the form of the power law coefficient that characterizes the shear thinning regime. However, as **Figure 3.2** clearly shows, for accurate assessment of the effect of shear on membrane spinning, the low-shear plateau regime and on-set of shear thinning at intermediate shear rates cannot be neglected. Therefore, we used the Carreau model, which accurately captures the characteristic flow curve across the entire range (four decades) of relevant shear rates in our study. Parameters obtained from the Carreau model fit for each polymer solution are listed in **Table 3.1**; the high-shear viscosity (η_∞) was fixed at 0.00166 Pa·s, the viscosity of the solvent (NMP) at 25 ˚C, because the experimental data did not provide accurate estimates for this parameter.

$$\frac{\eta-\eta_\infty}{\eta_0-\eta_\infty} = (1+(\lambda\dot{\gamma})^2)^{\frac{n-1}{2}} \qquad (3.1)$$

Table 3.1 Carreau viscosity model parameters for PEI polymer solutions.

	U30N70	U30N62.5E7.5	U30N60E10
η_0(Pa s)	44.66	48.707	53.10
η_∞ (Pa s)	0.00166	0.00166	0.00166
n	0.504	0.528	0.531
λ (s)	0.00478	0.00359	0.00437

The Carreau model parameters were then used to numerically calculate the velocity profile and shear rate distributions in a rectangular channel (COMSOL Multiphysica). Due to the finite aspect ratio of the rectangular channel (1:5), the geometry cannot be approximated as an infinite slit; as a consequence, the wall shear rates are not uniform along the channel wall. **Figure 3.3** presents the velocity profile and shear rate profile for U30N70 across the channel the cross-section (300 μm x 50 μm) at extrusion speed (average velocity) 5000 μm/s (or 4.5 μl/min). As expected, the simulation results show that shear rates are zero in the corners and at the center of the channel, and reach a maximum along the longer channel wall; this maximum shear rate value was used as wall shear rate and will be reported in the rest of this paper to quantify shear rates under various flow conditions in the rest of this paper.

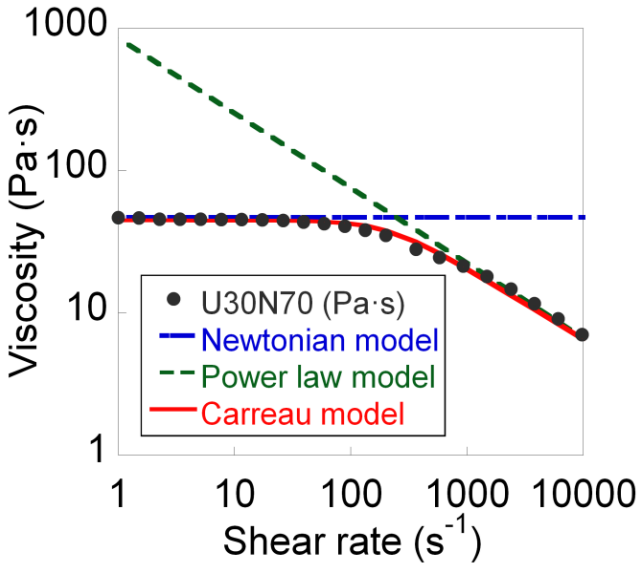

Figure 3.2. Model fitting results of U30N70 viscosity data for Newtonian, power law and Carreau models.

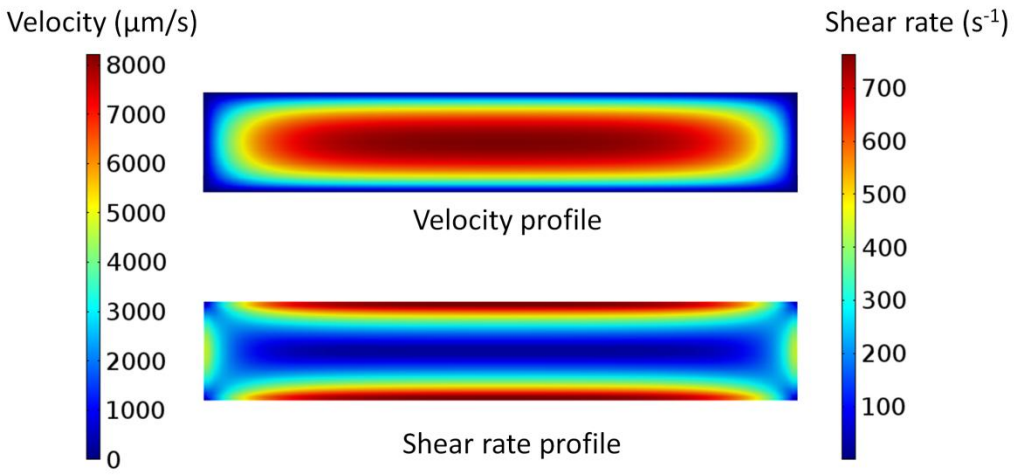

Figure 3.3. Velocity profile and shear rate profile of U30N70 in a rectangular channel with cross-section of 300 μm x 50μm. Calculations were based on the Carreau viscosity model parameters in **Table 3.1** with the average extrusion velocity of 5000μm/s.

The elongational viscosity is more difficult to measure than the shear viscosity and the methodology still requires instrumental improvements. The CaBER measures an apparent elongational viscosity over a narrow range of deformation rates, which is determined by the fluid's viscosity and cannot be controlled explicitly. Moreover, viscosity measurements with the CaBER are not steady-state measurements (filament stretching) and may contain systematic errors (e.g. interfacial instabilities). Nevertheless, the apparent elongational viscosity measured by CaBER is the best available for characterization of elongational rheology of these samples and should be interpreted with caution. For Newtonian, the elongational viscosity is three times larger than its shear viscosity ($\eta_e = 3\eta$). The apparent elongational viscosities of all three PEI solutions (U30N70, U30N62.5E7.5, U30N60E10) seem to follow this rule at low elongational

rates, but exhibit slight strain-thickening behavior with an increase of deformation rate over the rather limited experimentally accessible range of elongational rates (0.1~10 s^{-1}). As was found for shear viscosity (**Table 3.1**), solutions containing ethanol showed higher elongational viscosities.

3.3.2. Flow regime map of U30N70 (PEI/NMP, 30/70) in a rectangular channel

Dope solutions were extruded into a water bath (see **Figure 3.1**) for a wide range of extrusion rates; corresponding wall shear rates were calculated as described above. For all extrusion conditions, we found that the structural features observed in the low-magnification phase separation videos were in good agreement with the high-resolution cross-sectional images of the fibers taken by SEM. This implies that the structures and macrovoids formed during initial phase separation were well preserved during the subsequent process of immersion in water for prolonged times, drying, and fracturing for SEM microscopy. By combining the viscosity profile, phase separation videos, and corresponding cross-sectional images of the fibers, we were able to construct a flow regime map that correlates the dope rheology, phase separation kinetics and fiber morphology. **Figure 3.4** presents such a flow regime map for U30N70, including snapshots from the phase separation videos, cross-sectional SEM images of the extruded fibers, and the viscosity profile as a function of wall shear rate. Four distinct regimes were identified, based on the nature of the macrovoid defects that could be observed: axial macrovoids, transitional (from axial macrovoids to radial macrovoids), radial macrovoids, and secondary macrovoids. The key characteristics of these four regimes can be summarized as follows:

- Axial macrovoids: at low shear rates, a few long macrovoids grow along the axis of the fiber opposite to the extrusion direction. In cross-sectional images, these axial macrovoids appear almost circular with diameters of ca. 10 μm.
- Radial macrovoids: at the onset of shear thinning, many smaller tear–drop shaped macrovoids (1-5 μm) are evenly distributed along the outside of the long edge of the fiber; these macrovoids have a fairly uniform size distribution.
- Transitional regime: both types of macrovoids coexist: axial macrovoids near the outer edges of the fiber and radial macrovoids evenly distributed along the entire perimeter.
- Secondary macrovoids: at the highest shear rates, a new type of macrovoid forms near the center of the fiber; their size, shape and orientation is similar to the radial macrovoids, but they form much further away from the fiber surface. Also, in this regime, the cross-sectional shape of the fibers deviates from the channel shape; instead of the rectangular cross-section of the channel, fibers take on oval shapes with a maximum thickness that exceeds the channel height.

3.3.2.1. Axial macrovoids: effects of mass transfer

The low speed extrusion regime is characterized by axial macrovoids growing along the axis of the fibers. In this regime, wall shear rates are in the Newtonian plateau with constant viscosity; this scenario is not commonly seen in actual spinning processes, where higher shear rates (100-1000 s^{-1}) are usually maintained. As a result, axial

macrovoids are not usually reported in literature. Nevertheless, a discussion of their origin enhances understanding of the entire spinning process.

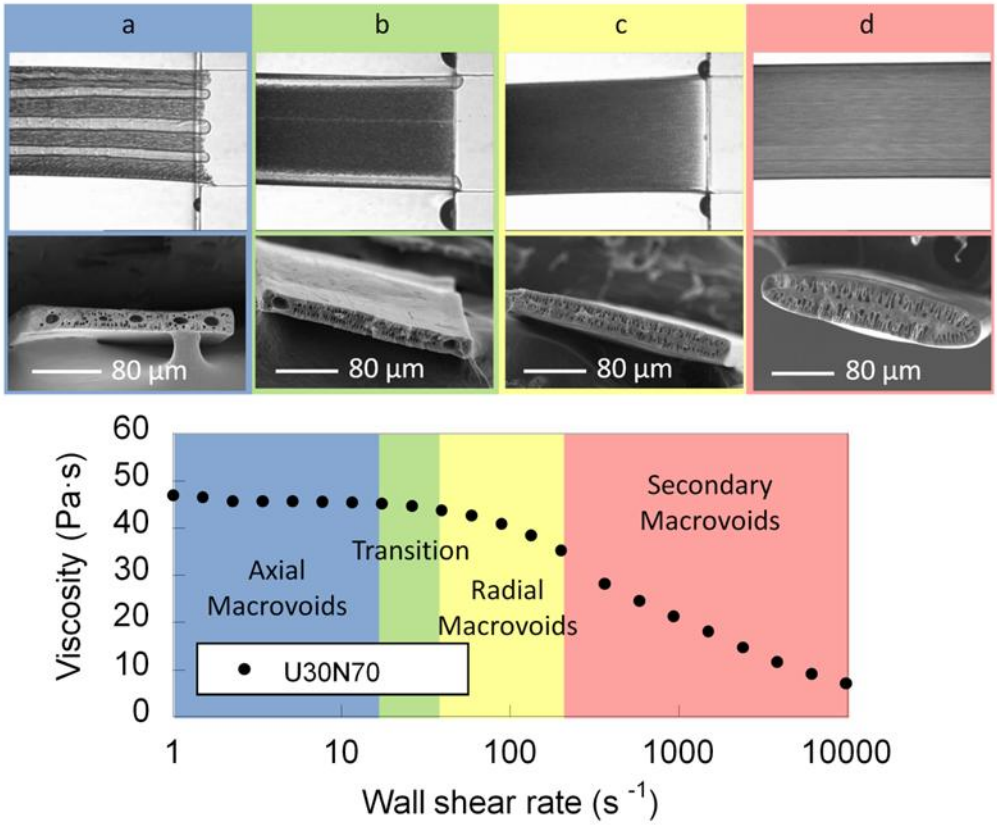

Figure 3.4. Flow regime map of U30N70 fibers extruded through a rectangular straight channel. Images at the first row represent microscopic view and images at the second row represent cross-sectional SEM images. Blue (a), green (b), yellow (c), and red color (d) represent axial macrovoid, transition, radial macrovoid and secondary macrovoid regime, respectively.

The axial macrovoids only appear in developed flow. At the initiation of the extrusion process, the polymer fibers start off with tear-drop-like macrovoids at the

leading edge of the fiber (not shown here). As extrusion continues, these smaller macrovoids coalesce to form long, axial macrovoids; once the flow reached steady state, axial macrovoids were always observed at these low extrusion rates (**Figure 3.4** a). Shear is not likely the dominant factor for axial macrovoid formation, because increased shear rates lead to a transition morphology, where the number of axial macrovoids is reduced and macrovoids migrate toward the edges of the fiber and merge until only two axial macrovoids are observed near the edges (**Figure 3.4** b). If the shear rate is further increased, the axial macrovoids disappear entirely. Our hypothesis was that mass transfer limitations with regards to exchange of solvent and non-solvent played a key role. To test this hypothesis, we designed a new microfluidic channel with enhanced control of non-solvent flow.

The side view of this second experimental set-up is depicted in **Figure 3.5**a. The channel was designed to purposely start and stop nonsolvent (water) counterflow, thus controlling the thickness of the mass transfer boundary layer between the fiber and the surrounding nonsolvent bath independently from the boundary later that is inherent to the moving fiber. The detailed design of the device and operating procedure for the experiments are depicted in **Figure 3.5**. The cross-channel design has injection sites for the polymer solution and nonsolvent, as well as an inlet and outlet for gas flow (in this case pure nitrogen). The polymer solution channel was loaded while dry nitrogen was flowing to remove moisture from the channel and suppress premature phase separation due to water vapor. As soon as the polymer solution filled the channel on the right side (**Figure 3.5** b), the nitrogen flow was stopped and water was injected to fill the channel instantly; we then had the choice to either stop the water flow (stagnant bath) or maintain

a steady nonsolvent counterflow (flowing bath). **Figure 3.6** a show images from an experiment in which nonsolvent flow was switched on after steady state had been achieved in a stagnant bath. Without counterflow of water, the polymer solution is extruded into a stagnant water bath. As expected, the result is similar to what was observed in the original setup (see **Figure 3.4** b): axial macrovoids are found under these conditions (image for 0 s in **Figure 3.6** a). When the counterflow of water is started, the axial macrovoids immediately stop growing and disappeared from the viewing area with the extruded fiber (1 s, 2 s, 3 s in **Figure 3.6** a). Upon cessation of the water counterflow, axial macrovoids reappeared (images not shown here). These experiments support the hypothesis that this intriguing phenomenon is caused by mass transfer limitations. Solvent (NMP) escaping from the fiber during phase separation forms a thick boundary layer around the fiber, which hinders the supply of fresh water to the fiber surface. The forced counterflow of fresh water reduces the boundary layer thickness, thus removing redundant solvent around the solidified fiber and enhancing mass transfer. To provide further support for this hypothesis, the same experiment was also carried out with an NMP/water (15/85 wt%) mixture as the nonsolvent. The addition of NMP to the bulk phase suppresses exchange rates of solvent and nonsolvent, because of the reduced concentration driving force. Even under counterflow conditions (**Figure 3.6** b), the surface concentration of NMP cannot be sufficiently reduced to enhance mass transfer rates and suppress axial macrovoid formation; the mass transfer enhancements due to flow are insufficient in this case to overcome the reduced concentration gradient. These experiments provide strong proof that axial macrovoid formation results from insufficient mass transfer due to residual solvent in the boundary layer around the fiber.

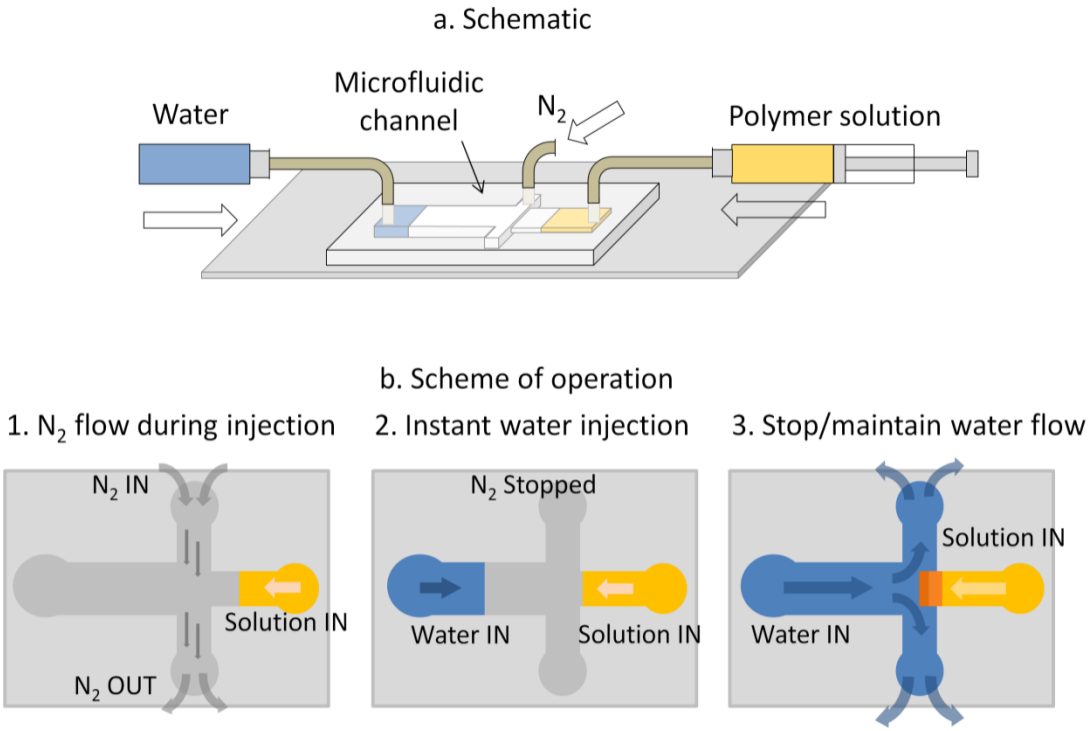

Figure 3.5. Modified microfluidic setup for axial macrovoid studies. a: schematic of modified microfluidic device, b: schematic of operational protocol.

Based on the these results, it is not surprising that axial macrovoids were not observed at intermediate and high shear rates, where the increased velocity difference between the extruded fiber and the stagnant bath also reduces the boundary layer thickness, thus eliminating mass transfer limitations during phase separation. Because they form only at low shear rates, axial macrovoids may not be a direct concern in most practical spinning processes. Nevertheless, these experiments underscore that inadequate solvent removal may be problematic and highlight the importance of controlling

composition and flow conditions of the nonsolvent bath during continuous membrane spinning processes.

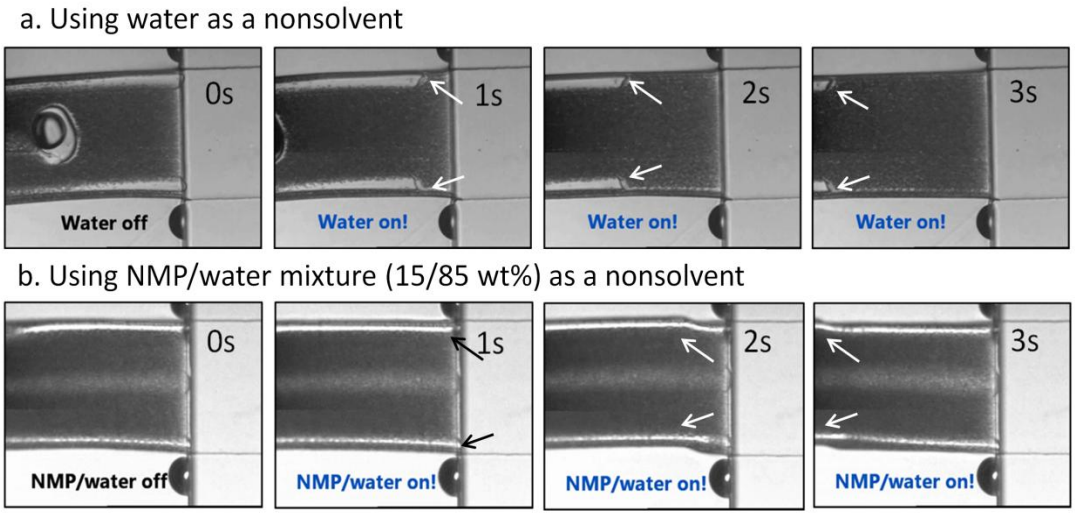

Figure 3.6. Change in axial macrovoid development with and without nonsolvent counterflow for different nonsolvents (a: water, b: NMP/water (15/85 wt%)). The counterflow was initiated at 1 second by injecting water from the left. Arrows trace the end of the axial.

3.3.2.2. Radial macrovoids: effects of thermodynamics

At shear rates where the flow curve begins to show shear-thinning effects, axial macrovoids disappeared entirely, i.e. mass transfer effects were no longer significant. In this regime, the shape of the polymer fiber remained rectangular and characteristic tear-drop-shaped macrovoids along the surface of the fibers, pointing radially inward (**Figure 3.4** c), dominated the fiber morphology. In this regime, which is well-documented in the fiber spinning literature [23, 24, 32, 33], phase separation and fiber morphology are

mostly affected by the inherent thermodynamic properties of the original dope solution, i.e. the equilibrium phase diagram. If the dope composition is too far from the binodal decomposition boundary, large amounts of nonsolvent are needed to initiate phase separation, leading to macrovoids. This phenomenon will be discussed in more detail in section 3.3.3, where a flow regime map is presented for a dope solution with a different composition.

3.3.2.3. Secondary macrovoids: effects of shear (die swell)

Further into the shear-thinning regime, the polymer solution experiences high shear stress and the viscosity decreases. Two noticeable features of the fibers that are formed in this regime are dimensional changes and secondary macrovoid formation (**Figure 3.4** d); both of these effects can be attributed to die swell. The cross-sectional area of the extruded fibers remains constant until roughly 150 s^{-1} and then starts to increase with increasing shear rates; in addition, the shape of the fibers changes from rectangular to oval. Dimensional changes in the extruded fibers at various shear rates were analyzed quantitatively with the image analysis software package Image J (freeware developed by the National Institutes of Health) [34]. Dimensional parameters of the fibers that were analyzed are the width, the ratio of center height to edge height and the area of fiber cross-sections in SEM images, as illustrated in **Figure 3.7** a**.** Specifically, the long dimension of the fiber cross-section is referred to as its width, while the short dimension at the center of the fiber is referred to as "center height"; the term "edge height" is used to refer to the average fiber height in the outer 10% of the fiber. The cross-sectional area was simply determined by counting all pixels within the fiber cross-

section. **Figure 3.7** b, c, d present the full quantitative dimensional analysis for three dope formulations (U30N70, U30N62.5E7.5 and U30N60E10) as a function of shear rate. In all cases, no prominent changes were found in width (**Figure 3.7** b), and we believe that this is because the applied shear rates at the side walls of the rectangular channel are relatively small, approaching zero in the corners (see **Figure 3.3**). A significant shape change, as quantified by changes in the ratio of center height to edge height, occurred for shear rates above 150 s^{-1}, as shown in **Figure 3.7** c. Some fibers that were extruded at low shear rates exhibit values of this height ratio below 1, which corresponds to a slightly concave shape. We believe that this can be attributed to difficulties in snapping fibers with axial macrovoids; these large voids (see **Figure 3.4** a) weaken the structure at the edges and fibers are easily bent or twisted. The bottom right plot in **Figure 3.7** d shows that the cross-sectional area of the fibers showed a similar trend; the area remained constant until shear rates of 150 s^{-1} but then increases drastically (from near 7000 μm^2 to 14000 μm^2 for U30N70, for example). It should be pointed out here that even the largest measured fiber cross-sectional area is still smaller than the actual channel cross-sectional area of 15000 μm^2; this apparent discrepancy can easily be explained by the fact that the fibers shrink during phase separation since the process involves solvent removal from the dope solution.

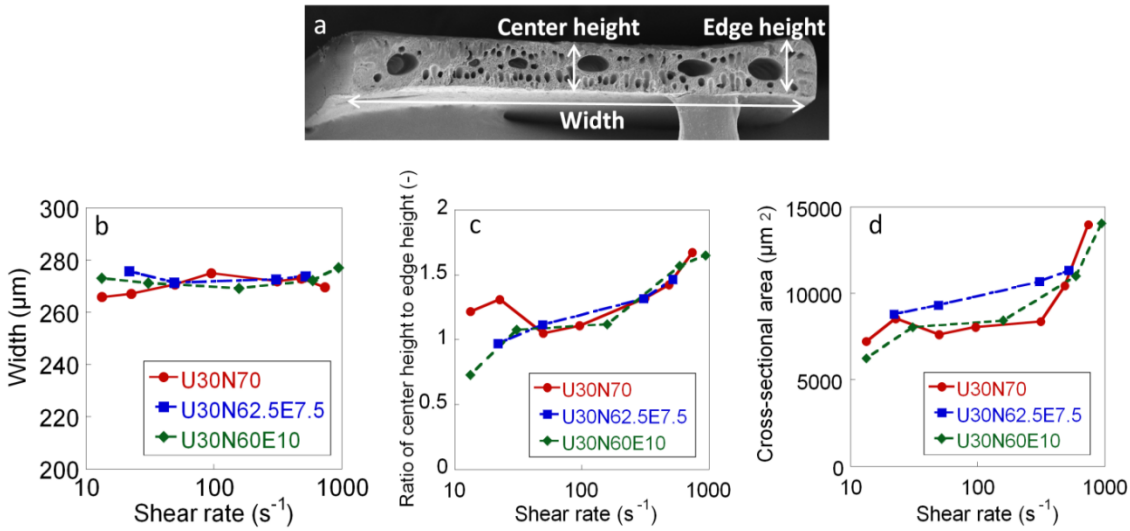

Figure 3.7. Dimensional change of extruded fibers as a function of shear rate for three dope formulations. a: definition of dimensions, b: width, c: ratio of center height to edge height, d: cross-sectional area.

The fact that fiber dimensions change with increasing shear has been reported before [35]. Ren and coworkers measured the cross-sectional dimensions of wet-spun hollow fiber membranes at different shear rates and found that the thickness of the hollow fiber wall increased with the shear rate (820 to 8200 s^{-1}). Although their work lacks a detailed analysis of the dope rheology, their applied shear rates are high enough to be in the regime that we refer to as secondary macrovoid regime. Our data and Ren's data [35] imply that the dimensions increase as shear rate increases, but always remain smaller than the channel dimensions of the spinneret.

Another interesting feature in this regime is secondary macrovoid formation: an area of circular cavities toward the center of the fiber, in addition to the radial macrovoids

near the surface. This phenomenon was seen in all three dope formulations, as we will discuss below in more detail for U30N60E10, as well as in other studies [23, 32].

These two features, dimensional change and secondary macrovoid formation, are both related to die swell. As the polymer solution exits the channel, the solution relaxes the shear and normal stresses. The diameter of the solution stream expands suddenly (die swell) when high normal stresses are present, as is the case for many concentrated polymer solutions at high shear rates. Simultaneously occurring phase separation then solidifies the enlarged fiber shape from the outer surface inward and consequently, the solution underneath the surface becomes more polymer-lean, which is likely causing more macrovoids to form.

3.3.3. Flow regime map of U30N60E10 (PEI/NMP/ethanol, 30/60/10) in a rectangular channel

The measurements above were carried out with PEI/NMP solutions. Although clear regimes could be identified regarding fiber shape and macrovoids as a function of shear rate, no conditions could be found at which macrovoid-free fibers were formed, which is the ultimate goal in a spinning process. As explained in the introduction, it is common to use dope solutions with co-solvent in an actual membrane fabrication process, because the resulting fibers contain fewer macrovoids. We therefore repeated the flow regime characterization for U30N60E10, which contains 10 wt% ethanol; the result is shown in the upper half of **Figure 3.8** (shear only). At all shear rates, macrovoid formation was suppressed significantly in comparison with U30N70. Axial macrovoids became much shorter in both the axial macrovoid and transitional regimes, as is clearly

seen in the upper left image. Most importantly, radial macrovoids disappeared entirely with this dope composition and a macrovoid-free regime was found at shear rates near the onset of shear-thinning. In fact, a gradual transition was observed from radial macrovoids to macrovoid-free fibers with an increase of ethanol concentration (U30N70 → U30N62.5E7.5 → U30N60E10), as shown in **Figure 2.6**. These results agreed with Ren and researchers [17], whose data also show that the macrovoid-free layer increases as more co-solvent added to the dope solutions.

Although radial macrovoids could be eliminated by using proper dope composition and moderate shear rates, secondary macrovoid formation and dimensional change were still noticeable in the high shear regime for the ethanol-containing dopes. This is not surprising because the occurrence of die swell is not affected significantly by the changes in dope composition. However, the morphological changes (axial macrovoid → macrovoid-free → secondary macrovoid) with increasing shear rate are more noticeable in U30N60E10 than in U30N70. It implies that shear stress affects the morphology of the polymer solution most noticeably when the solution composition is close to the binodal boundary. Effects of shear on membrane morphology were tested by several other researchers [23, 24, 32, 33], but in most studies, neither macrovoid-free conditions nor noticeable changes in morphology were found in the cross-section of the spun fibers. This can probably be explained by the fact that their dope composition is far from the phase boundary (all of the fibers contained macrovoids).

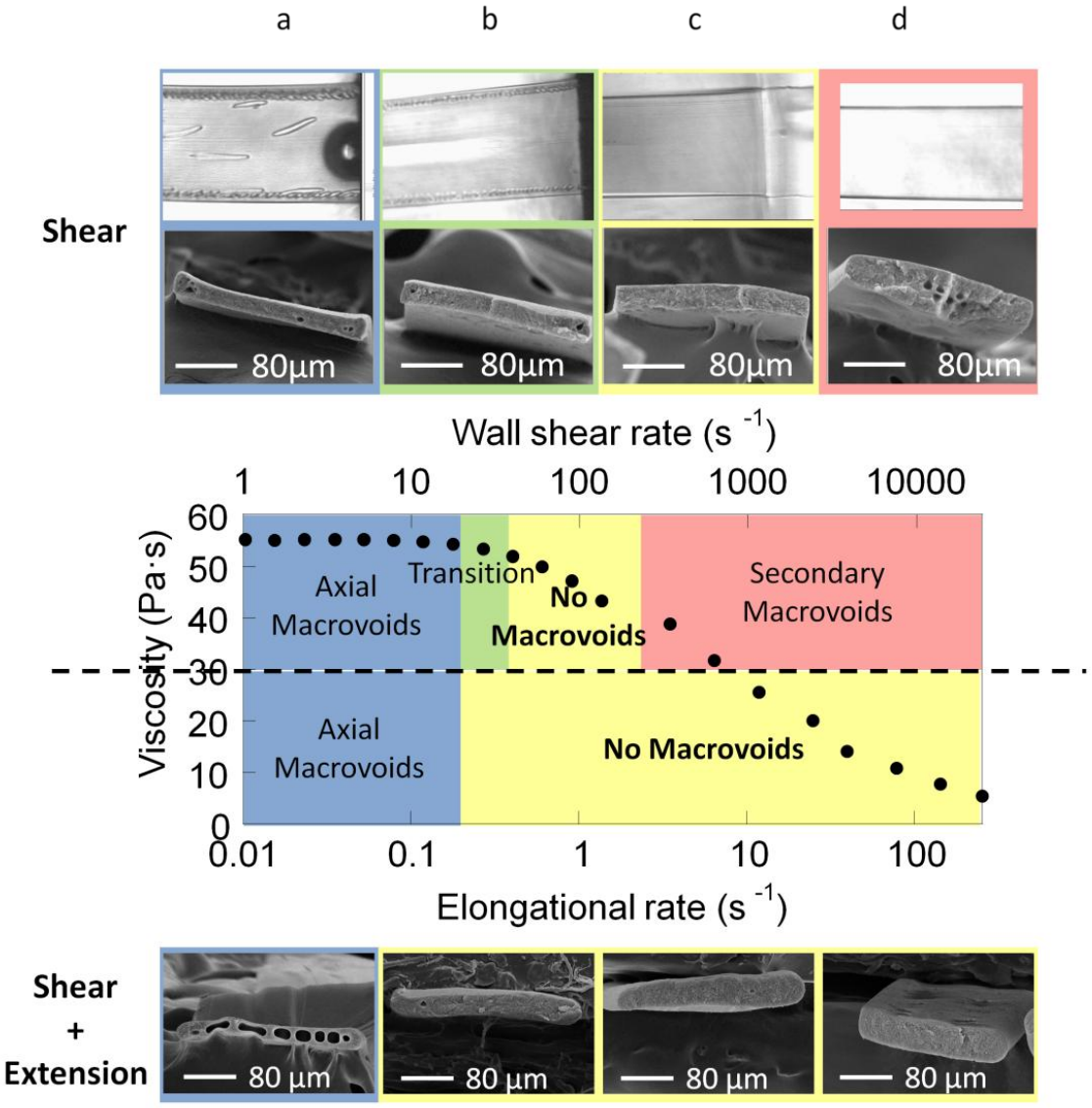

Figure 3.8. Flow regime map of U30N60E10 fibers extruded from a straight channel (upper half from the dash line) and a 7:1 contraction channel (bottom half from the dash line). Images at the first row represent microscopic view and images at the second row represent cross-sectional SEM images from a straight channel. Images at the bottom row represent cross-sectional SEM images from contraction channel. Blue (a), green (b), yellow (c), and red color (d) represent axial macrovoid, transition, no macrovoid and secondary macrovoid regime, respectively.

3.3.4. Flow regime map of U30N60E10 (PEI/NMP/ethanol, 30/60/10) in a contraction channel

The U30N60E10 solution was also extruded through a contraction channel of Hencky strain 2 to apply elongational stress prior to phase separation in addition to shear. In this channel, shear stresses are mostly confined near the wall (see **Figure 3.3**), while elongational stresses are applied across the entire cross-sectional area. In this geometry, each extrusion rate corresponds to both a shear rate and an elongational rate; the double axis in **Figure 3.8** represents shear and elongational rates. The flow regime map for these elongational experiments is presented in the bottom half of **Figure 3.8,** in order to facilitate direct comparison with the shear experiments discussed above. Only two regimes were found in this case; axial macrovoids at very low extrusion rates, and a macrovoid-free regime at high rates. These results clearly show that macrovoids were suppressed by elongational stresses even at shear rates in secondary macrovoid regime for pure shear flow. The enlarged shape of macrovoid-free fibers indicates the presence of normal stresses (die swell), but the elongation apparently successfully reduces macrovoid defect formation. Moreover, the fact that macrovoid formation is suppressed in the contraction channel where shear and elongation coexist, implies that the macrovoids will also effectively removed by extension when the dope is exposed to shear-free conditions in the dry-wet spinning process.

As mentioned in the previous section, macrovoids are suppressed by elongational stresses, only when the dope composition is close enough to binodal curve (in our case, adding more ethanol). It implies that the shear or extensional stress only contributes to a subtle change in phase behavior of the dope solutions compared to the compositional

parameters. For example, in the case of U30N70 fibers, we found that macrovoids remained regardless of the extrusion speed and regardless of the type of channel. On the other hand, the effect of shear and extension was maximum in U30N60E10, which is the composition closest to the binodal curve. Therefore, in order to take the full advantages of the elongational stresses in eliminating macrovoids, the dope composition must be optimized first.

3.4. Conclusion

Although the *in situ* observation of phase separation and macrovoid formation in solutions at rest has been reported extensively, our study is the first attempt to visualize these processes in the presence of flow. Utilizing the advantages of microfluidics and video-microscopy, we visualized the phase separation and macrovoid formation processes under different flow conditions. The effect of shear and elongation on macrovoid formation was demonstrated by extruding the polymer solution through a straight channel and a contraction channel into a non-solvent bath (wet phase separation). The morphology of phase-separated polymer fibers correlates with the rheological properties of the dope and is affected by: 1) mass transfer at low extrusion rates, 2) dope thermodynamics at intermediate rates, and 3) shear and elongational stresses at high extrusion rate. Macrovoid defects at low shear rates can be eliminated by facilitating mass transfer. In the intermediate regime, most macrovoids can be eliminated by changing the dope composition. The macrovoids at a high extrusion speed, which relates

most closely to actual spinning conditions, can be removed by elongational stresses in nascent fibers prior to phase separation.

Our results may help understand the confusing experimental results listed in **Table 1.1**. Many researchers have attempted to examine the effect of a single spinning parameter on fiber formation from specific dope solutions, and their findings were not always in good agreement to each other. For example, increasing shear rates sometimes suppressed formation of macrovoids, but sometimes no effects were found. This can be explained with our observation that increasing shear influenced different effects on fiber morphology according to the shear rates.

One might think that our wet extrusion experiment through the contraction channel has weak relevance to actual air-gap extension and dry-wet phase separation. However, for fundamental understanding of shear and elongational stresses, devices like ours are essential to simplify the process and eliminate undesirable coupling between effects such as compositional and dimensional change during phase separation, which occur simultaneously in actual dry-wet spinning. Moreover, from the fact that macrovoid formation is suppressed in the contraction channel where shear and elongation coexist, it is also expected that the macrovoids would be effectively removed when the dope is exposed to shear-free elongation in the dry-wet spinning process.

3.5. References

[1] R. Matz, The structure of cellulose acetate membranes 1. The development of porous structures in anisotropic membranes, Desalination, 10 (1972) 1-15.

[2] R.J. Ray, W.B. Krantz, R.L. Sani, Linear stability theory model for finger formation in asymmetric membranes, Journal of Membrane Science, 23 (1985) 155-182.

[3] M.A. Frommer, R.M. Messalem, Mechanism of membrane formation. VI. Convective flows and large void formation during membrane precipitation, Industrial & Engineering Chemistry Product Research and Development, 12 (1973) 328-333.

[4] C. Cohen, G.B. Tanny, S. Prager, Diffusion-controlled formation of porous structures in ternary polymer systems, Journal of Polymer Science: Polymer Physics Edition, 17 (1979) 477-489.

[5] S.A. McKelvey, W.J. Koros, Phase separation, vitrification, and the manifestation of macrovoids in polymeric asymmetric membranes, Journal of Membrane Science, 112 (1996) 29-39.

[6] S. Husain, W.J. Koros, Macrovoids in hybrid organic/inorganic hollow fiber membranes, Industrial & Engineering Chemistry Research, 48 (2009) 2372-2379.

[7] M.R. Pekny, J. Zartman, W.B. Krantz, A.R. Greenberg, P. Todd, Flow-visualization during macrovoid pore formation in dry-cast cellulose acetate membranes, Journal of Membrane Science, 211 (2003) 71-90.

[8] M.R. Kosuri, W.J. Koros, Defect-free asymmetric hollow fiber membranes from Torlon®, a polyamide–imide polymer, for high-pressure CO2 separations, Journal of Membrane Science, 320 (2008) 65-72.

[9] G.R. Guillen, G.Z. Ramon, H.P. Kavehpour, R.B. Kaner, E.M.V. Hoek, Direct microscopic observation of membrane formation by nonsolvent induced phase separation, Journal of Membrane Science, 431 (2013) 212-220.

[10] D.-M. Wang, F.-C. Lin, T.-T. Wu, J.-Y. Lai, Formation mechanism of the macrovoids induced by surfactant additives, Journal of Membrane Science, 142 (1998) 191-204.

[11] F.G. Paulsen, S.S. Shojaie, W.B. Krantz, Effect of evaporation step on macrovoid formation in wet-cast polymeric membranes, Journal of Membrane Science, 91 (1994) 265-282.

[12] L. Zeman, T. Fraser, Formation of air-cast cellulose acetate membranes. Part I. Study of macrovoid formation, Journal of Membrane Science, 84 (1993) 93-106.

[13] S.H. Yoo, J.H. Kim, J.Y. Jho, J. Won, Y.S. Kang, Influence of the addition of PVP on the morphology of asymmetric polyimide phase inversion membranes: effect of PVP molecular weight, Journal of Membrane Science, 236 (2004) 203-207.

[14] J.-H. Kim, K.-H. Lee, Effect of PEG additive on membrane formation by phase inversion, Journal of Membrane Science, 138 (1998) 153-163.

[15] R. Bloch, M.A. Frommer, The mechanism for formation of "skinned" membranes I. Structure and properties of membranes cast from binary solutions, Desalination, 7 (1970) 259-264.

[16] K.Y. Wang, D. Fei Li, T.-S. Chung, S. Bor Chen, The observation of elongation dependent macrovoid evolution in single- and dual-layer asymmetric hollow fiber membranes, Chemical Engineering Science, 59 (2004) 4657-4660.

[17] J. Ren, J. Zhou, M. Deng, Morphology transition of asymmetric polyetherimide flat sheet membranes with different thickness by wet phase-inversion process, Separation and Purification Technology, 74 (2010) 119-129.

[18] D. Li, Thickness dependence of macrovoid evolution in wet phase-inversion asymmetric membranes, Industrial and Engineering Chemistry Research, 43 (2004) 1553-1556.

[19] N. Widjojo, Thickness and air gap dependence of macrovoid evolution in phase-inversion asymmetric hollow fiber membranes, Industrial and Engineering Chemistry Research, 45 (2006) 7618-7626.

[20] D.T. Clausi, W.J. Koros, Formation of defect-free polyimide hollow fiber membranes for gas separations, Journal of Membrane Science, 167 (2000) 79-89.

[21] T.-S. Chung, Effect of air-gap distance on the morphology and thermal properties of polyethersulfone hollow fibers, Journal of Applied Polymer Science, 66 (1997) 1067-1077.

[22] T.-S. Chung, Fundamental understanding of the effect of air-gap distance on the fabrication of hollow fiber membranes, Journal of Applied Polymer Science, 72 (1999) 379-395.

[23] T.-S. Chung, J.-J. Qin, J. Gu, Effect of shear rate within the spinneret on morphology, separation performance and mechanical properties of ultrafiltration polyethersulfone hollow fiber membranes, Chemical Engineering Science, 55 (2000) 1077-1091.

[24] T.-S. Chung, Effect of shear stress within the spinneret on hollow fiber membrane morphology and separation performance, Industrial and Engineering Chemistry Research, 37 (1998) 3930-3938.

[25] Y. Dai, J.R. Johnson, O. Karvan, D.S. Sholl, W.J. Koros, Ultem®/ZIF-8 mixed matrix hollow fiber membranes for CO2/N2 separations, Journal of Membrane Science, 401–402 (2012) 76-82.

[26] S. Husain, W. Koros, Mixed matrix hollow fiber membranes made with modified HSSZ-13 zeolite in polyetherimide polymer matrix for gas separation, Journal of Membrane Science, 288 (2007) 195-207.

[27] J.C. McDonald, D.C. Duffy, J.R. Anderson, D.T. Chiu, H. Wu, O.J.A. Schueller, G.M. Whitesides, Fabrication of microfluidic systems in poly(dimethylsiloxane), Electrophoresis, 21 (2000) 27-40.

[28] E. Sollier, C. Murray, P. Maoddi, D. Di Carlo, Rapid prototyping polymers for microfluidic devices and high pressure injections, Lab on a Chip, 11 (2011) 3752-3765.

[29] C. Sung Hwan, J. Godin, L. Yu-Hwa, Optofluidic waveguides in Teflon AF-coated PDMS microfluidic channels, Photonics Technology Letters, IEEE, 21 (2009) 1057-1059.

[30] M.N. Oliveira, M. Alves, F. Pinho, G. McKinley, Viscous flow through microfabricated hyperbolic contractions, Experiments in Fluids, 43 (2007) 437-451.

[31] R. Eisenschitz, B. Rabinowitsch, K. Weissenberg, Zur Analyse des Formänderungswiderstandes, Springer Berlin Heidelberg, 1929.

[32] T.-S. Chung, Effect of shear rates on gas separation performance of 6FDA-durene polyimide hollow fibers, Journal of Membrane Science, 167 (2000) 55-66.

[33] J. Qin, Effect of dope flow rate on the morphology, separation performance, thermal and mechanical properties of ultrafiltration hollow fibre membranes, Journal of Membrane Science, 157 (1999) 35-51.

[34] W.S. Rasband, ImageJ, National Institutes of Health, Bethesda, Maryland, USA, http://imagej.nih.gov/ij/, 1997-2012.

[35] J. Ren, Z. Li, F.-S. Wong, D. Li, Development of asymmetric BTDA-TDI/MDI (P84) co-polyimide hollow fiber membranes for ultrafiltration: the influence of shear rate and approaching ratio on membrane morphology and performance, Journal of Membrane Science, 248 (2005) 177-188.

CHAPTER 4

INSTABILITY IN SPINNING: ROLES OF RHEOLOGY AND PHASE SEPARATION KINETICS

4.1. Introduction

Attempts to understand of the effects of complicated parameters such as phase separation kinetics, shear and elongational stresses on the polymer morphology were demonstrated in the previous chapters. In addition to the complexity from various parameters, spinning instabilities such as necking, capillary break-up, and draw resonance often observed in the spinning process and become obstacles to a continuous operation or production. The first two examples can be negligible in steady-state process with the use of viscous fluids and the details of this discussion are described in review [1-3]. The latter, draw resonance is a periodic fluctuation in the diameter of the fiber when the liquid filament is spun at a constant extrusion rate and at a constant take-up rate. This phenomenon is observed when the take-up rate becomes too fast, i.e. the draw ratio becomes too high.

The discussion of draw resonance in hollow fiber membrane spinning (using concentrated polymer solution in solvents as a spinning dope) was received less attention compared to the conventional fiber spinning with polymer melts [4]. The occurrence of draw resonance (often referred to as “pulsing”) or the specification of spinnable regime in membrane spinning has been hardly discussed in most of the literature. Based on

available literature, the typical draw ratio used in hollow fiber membrane spinning remained relatively low 2~10 [5-11]. Some achieved very high draw ratio up to 36 [6, 11], although no comments were made on the instabilities. Nevertheless, it is undoubtedly important that the successful steady state process of hollow fiber membrane with high draw ratio leads to improvement in the productivity.

Fortunately, extensive research has been accomplished regarding instabilities in the polymer melt spinning [12-20]. First observation of draw resonance was reported in early 1960s [21, 22] and soon after that, Bergonzoni and Dicresce showed experimentally that the onset of draw resonance is related to the draw ratio [17]. According to them, the liquid fiber is stable at low draw ratio and transits to instability as the draw ratio increase. Then, the onset of draw resonance in melt spinning was predicted theoretically and proven by experiments [23]; the mechanics of the spinning was analyzed by setting up mass and momentum balance equations assuming isothermal process with no inertia, gravity, and surface tension. The linearized stability analyses predicted that the process becomes unstable when the draw ratio becomes larger than 20.21 in Newtonian fluids with a constant viscosity [24-26] and the experimental results was consistent with the theoretical value [27]. These theoretical analyses were expanded to power law fluids and Upper Convected Maxwell (UCM) fluids [23, 28]. **Figure 4.1** shows the stability diagram of power law and UCM fluids. In both plots, the vertical axis is the draw ratio and the horizontal axes are power law exponent of power law viscosity model (left) and the dimensionless parameter that represents the viscoelasticity of the material (right). When the power law exponent is 1 (i.e. Newtonian fluids), the onset of draw resonance is

20.21. If the fluids exhibit shear-thinning behavior (n<1), the onset of draw resonance decreases and the spinning flow becomes unstable at lower draw ratio.

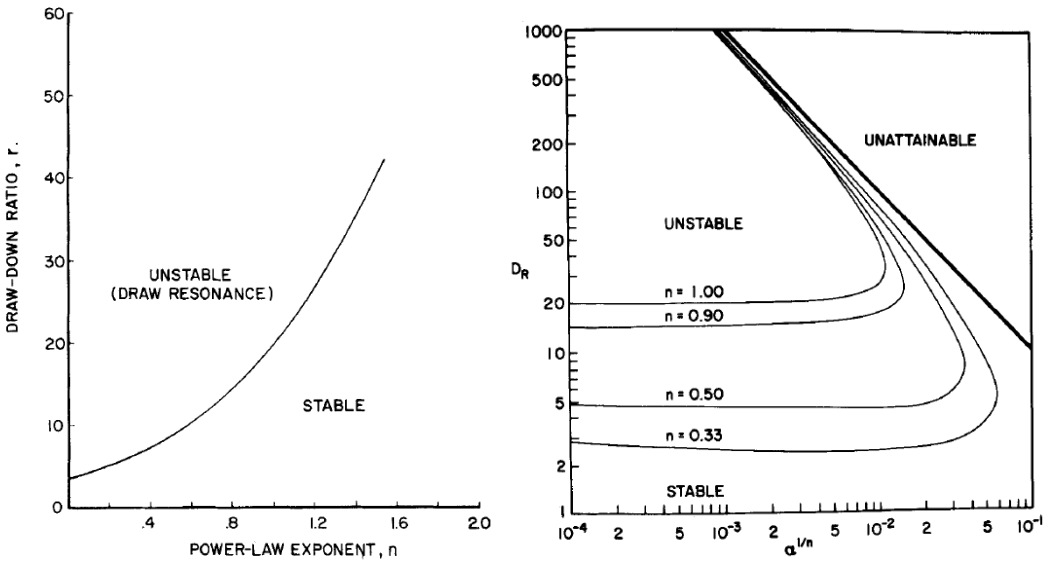

Figure 4.1 Right: Stability diagram of power law fluids [28] and Upper Convected Maxwell fluids [23]. Unstable region is where the draw resonance occurs. In unattainable region, no steady state exists and the spinning is theoretically impossible.

Although the hollow fiber spinning is inherently different from solid fiber spinning (plane extensional flow vs. uniaxial extensional flow), the theory of critical draw ratio is also valid for hollow fiber spinning [3]. The author demonstrated that the critical draw ratio of 20.21 in Newtonian fluids is also valid for hollow fiber spinning, in case that the air and a Newtonian fluid with constant viscosity were used as a bore fluid (internal coagulant). Assumptions are made to simplify the system including no reaction or no temperature gradient between the dope and the bore fluid. This same assumption

can be applied in hollow fiber membrane spinning as we have already confirmed in Chapter 2, that the phase separation rate at the interface between bore fluid and the dope solution is sufficiently slow. For example, our results in Chapter 2 suggested that the phase separated layer during the air gap residence time of 1second is less than 5 μm in case of using NMP/water 85/15 mixture as a bore fluid and PEI/NMP 30/70 as a dope solution. It indicates that the inner bore fluid functions as a place holder and will have minimal effects on the occurrence of the instability.

As a practical way to stabilize the spinning flow, cooling the air was theoretically suggested and the experimental results showed good agreement [25, 29]. In the melt spinning, the solidification is typically achieved by quenching, an abrupt temperature change that occurs in the quench bath. By allowing the mild cooling in the air while the fibers are pulled, they found that the fluids in the spinline remain stable even at higher draw ratio than in isothermal setting. The same effects can be expected in hollow fiber membrane fabrication by manipulating the rate of phase separation (solidification). Adding volatile nonsolvent to the dope solution is commonly used to increase the susceptibility to the thermodynamic disturbance and faster the kinetics of phase separation. Also, evaporation of volatile component during the air gap was hypothesized and often considered as a cause of dense skin layer formation for enhancing membrane performance. However, the residence time in the air is very short (~1 s) and whether the solvent evaporation in this short timescale affects the membrane properties has not been clearly understood.

In this Chapter, the effects of rheology of the dopes and the phase separation kinetics on the stability in the spinning process will be demonstrated. Although our

ultimate application is to understand the instability in the hollow fiber membrane spinning, the experiments will be done in solid fiber spinning apparatus in hope that the experimental data can be utilized in hollow fiber membrane spinning.

4.2. Experiments

4.2.1. Materials

The polymer used was PEI (Polyetherimide, Ultem® 1000; SABIC Innovative Plastics). The PEI, provided as powder, was first dried in the oven to remove residual moisture before making solutions. NMP (*N*-Methyl-2-pyrrolidone, 99%, Sigma Aldrich) and ethanol (anhydrous, 99%, VWR) were used as a solvent and a co-solvent. Binary solutions (PEI/NMP) were made with following compositions: 24/76, 26/74, 28/72, 30/70, and 31/69 wt%. And then PEI with multiple solvents were also made with following compositions; PEI/NMP/ethanol (30/60/10 wt%) and PEI/NMP/ethanol (30/57.5/12.5 wt%). After mixing all components, the solutions were placed on a slow roller for about a week to ensure complete dissolution of the PEI into homogeneous solutions.

4.2.2. Measurement of dope viscosity

The shear viscosity of polymer solutions was measured with a rotational rheometer (MCR 300, Anton Paar). All the samples were measured with a Peltier-controlled Couette geometry (inner diameter 10.0 mm and outer diameter 10.84 mm),

which minimize the contact with the air to prevent the humidity-induced phase separation.

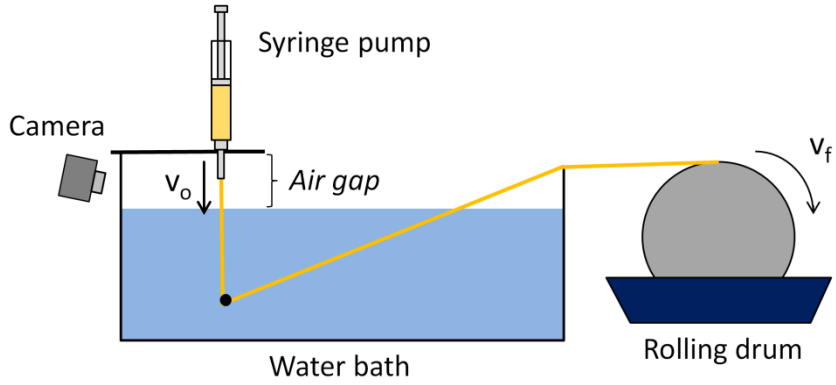

Figure 4.2 The scheme of fiber spinning apparatus.

4.2.3. Measurement of phase separation kinetics and video analysis

The kinetics of phase separation was measured with the microfluidic device invented in Chapter 2. The same experimental apparatus as well as the channel dimensions was used in this chapter. For PEI/NMP system, dry nitrogen was blown prior to solution injection, to prevent premature phase separation by removing moisture in the channel. Then, the water was injected immediately after the cessation of nitrogen flow. For PEI/NMP/ethanol system, the mixture gas of nitrogen and ethanol vapor was provided after supply of pure nitrogen, to prevent aggressive solvent evaporation during sample injection. In all cases, phase separation was induced by the invasion of water as a nonsolvent, and the process of phase separation was recorded.

The video of phase separation kinetics was analyzed by tracking the growing thickness of the solidified layer, as described in Chapter 2. The phase separation rate of

PEI/NMP/ethanol (30/60/10 wt%) was determined to be equal to the effective diffusivity of 15 s (see **Figure 2.4**), where the long term and short term slopes are constant through the elapsed time. The phase separation rate of PEI/NMP/ethanol (30/57.5/12.5 wt%) was determined by interpolation between PEI/NMP/ethanol (30/60/15 wt%), which is hypothetically saturated sample (0 s in **Figure 2.4**), and PEI/NMP/ethanol (30/60/10 wt%).

4.2.4. Fiber spinning apparatus and spinning conditions

The scheme of spinning apparatus is described in **Figure 4.2**. The syringe pump was mounted in vertical direction on the top of the water bath and the dope solution was extruded through 18G needle tip (ID 0.038" and OD 0.050"), attached to a 3ml syringe. Camera was mounted to record the flow behavior of the fiber at the air gap. **Figure 4.3** shows spinning conditions with the extrusion velocity (v_o) and take-up velocity (v_f) tested in this study. As introduced in Chapter 1, the draw ratio is defined as the ratio of take-up velocity to extrusion velocity and as such, a specific draw ratio at each spinning condition was calculated from a pair of v_o and v_f by following equation.

$$Draw\ Ratio = \frac{v_f}{v_o} \tag{4.1}$$

The draw ratios tested were 45 conditions, from maximum value of 90 to minimum of 2, as marked in **Figure 4.3** a. Three air gap distances were used 1.5 cm, 3 cm, and 6cm with these draw ratios. The residence time at the air gap was calculated by following equation [30]

$$t_{gap} = \frac{(ln\frac{v_f}{v_o})\cdot(\mathrm{Air\ Gap})}{v_f - v_o} \quad (4.2)$$

and residence time in air gap of 1.5 cm are shown in **Figure 4.3** b. The residence time at the air gap increases toward the bottom right corner and decreases toward upper left corner. At each air gap condition, the range of residence time (t_{gap}) was 0.05 - 0.21 s, 0.10 - 0.77 s, and 0.20 - 1.54 s, respectively. It is important to note that by changing the air gap distance, only residence time varies and draw ratio is independent of air gap.

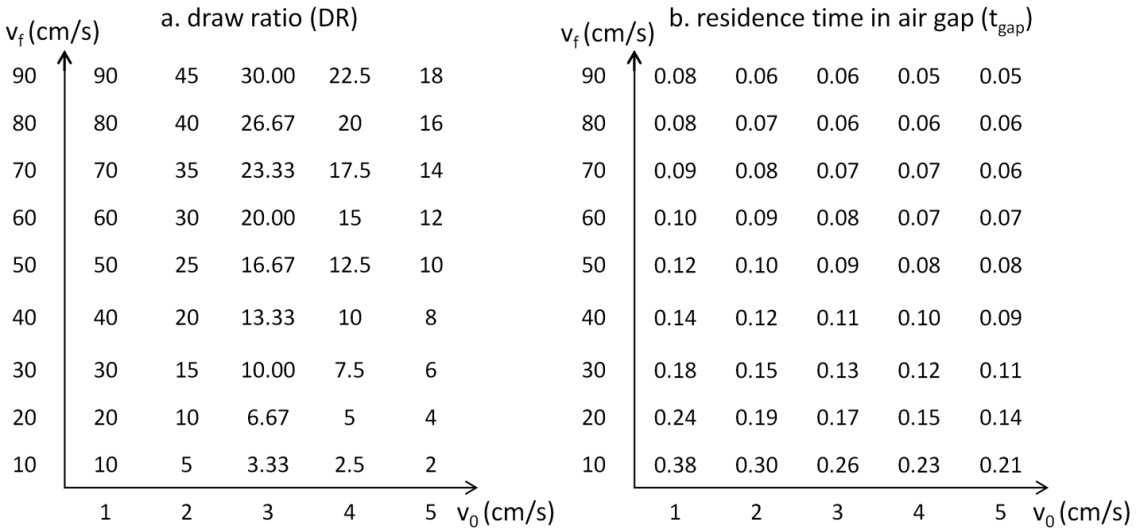

Figure 4.3 Spinning conditions. a. draw ratio and b. residence time in air gap distance of 1.5 cm.

4.2.5. Scanning electron microscope analysis

Spun polymer fibers were immersed in water for two days for complete phase separation and dried overnight in the oven at 75˚C. After being fully dried, the polymer fibers were immersed in liquid nitrogen, fractured and sputter-coated with gold (Q150T,

Quorum Technologies). Cross-sectional images of the fibers were taken by a scanning electron microscope (SEM; LEO 1550).

4.3. Results and Discussion

4.3.1. PEI/NMP system

4.3.1.1. The dope viscosity and the phase separation kinetics

The viscosity of PEI/NMP solutions with polymer concentration 24-31 % is shown in **Figure 4.4** a. The viscosity increases exponentially with an increase of polymer concentration, as commonly reported in other literature. The progression of water-induced phase separation was presented with the effective diffusion coefficient from the Equation 1.5, as introduced in Chapter 2. **Figure 4.4** b shows the effective diffusivity of phase separation in different concentration solutions. As the polymer concentration increases, the diffusivity decreased and reached a plateau near a concentration on 30 wt%. The same tendency in diffusivity has been reported elsewhere [31], indicating that the rapid increase in viscosity reduce phase separation rate.

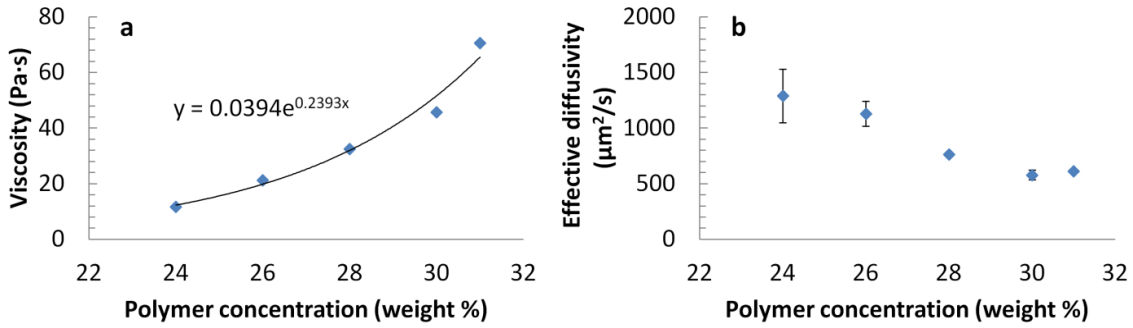

Figure 4.4 PEI/NMP solutions characterization. a: viscosity and b: effective diffusivity of water-induced phase separation of PEI/NMP solutions as a function of PEI polymer concentration.

4.3.1.2. Characteristic flow classification and spinnability diagram

The camera monitored the flow from the outlet of the needle tip through air gap to sub water-air interface (see **Figure 4.5** a). Several characteristic flows were observed in various spinning conditions in the fiber spinning with polymer solutions. These flows were referred as dripping, jetting, draw resonance, sagging, and break-up. Among them, jetting, dripping, and draw resonance are shown in **Figure 4.5**.

In dripping regime (**Figure 4.5** b), the liquid filament forms discontinuous droplets above the water-air interface and in this regime, continuous steady state operation is impossible. Jetting regime (**Figure 4.5** a) is where the liquid filament is pulled and forms continuous flow with the smoothly decreasing fiber diameter. Starting from jetting regime, the periodic pulsation begins to occur as the take-up rate increases, and this is referred as draw resonance (**Figure 4.5** c). The boundary between jetting and draw resonance was determined by magnified view at the air gap. We found that even at jetting regime, draw resonance can be occurred by any vibration or rapid pulling at start-

up flow and thus, the investigation was always started at low value of draw ratio and gradually increased to higher ones. If the fibers are pulled at higher draw ratio, the amplitude of the pulsation becomes larger and eventually, the liquid filament breaks up due to high drawing tension. This condition was defined as the boundary between draw resonance and break-up regime. Although dripping and break-up both indicates the breakage of the fiber, the difference was whether the fluid flows continuously when no drawing force is applied. Sagging occurs when the take-up velocity is slower than the extrusion velocity, which is additionally accelerated by gravity. In sagging conditions, the flow at the air gap is stabilized similar to jetting regime but the mismatch of velocity causes accumulation of solidified fibers at the bottom of water bath and eventually leads to the failure in operation.

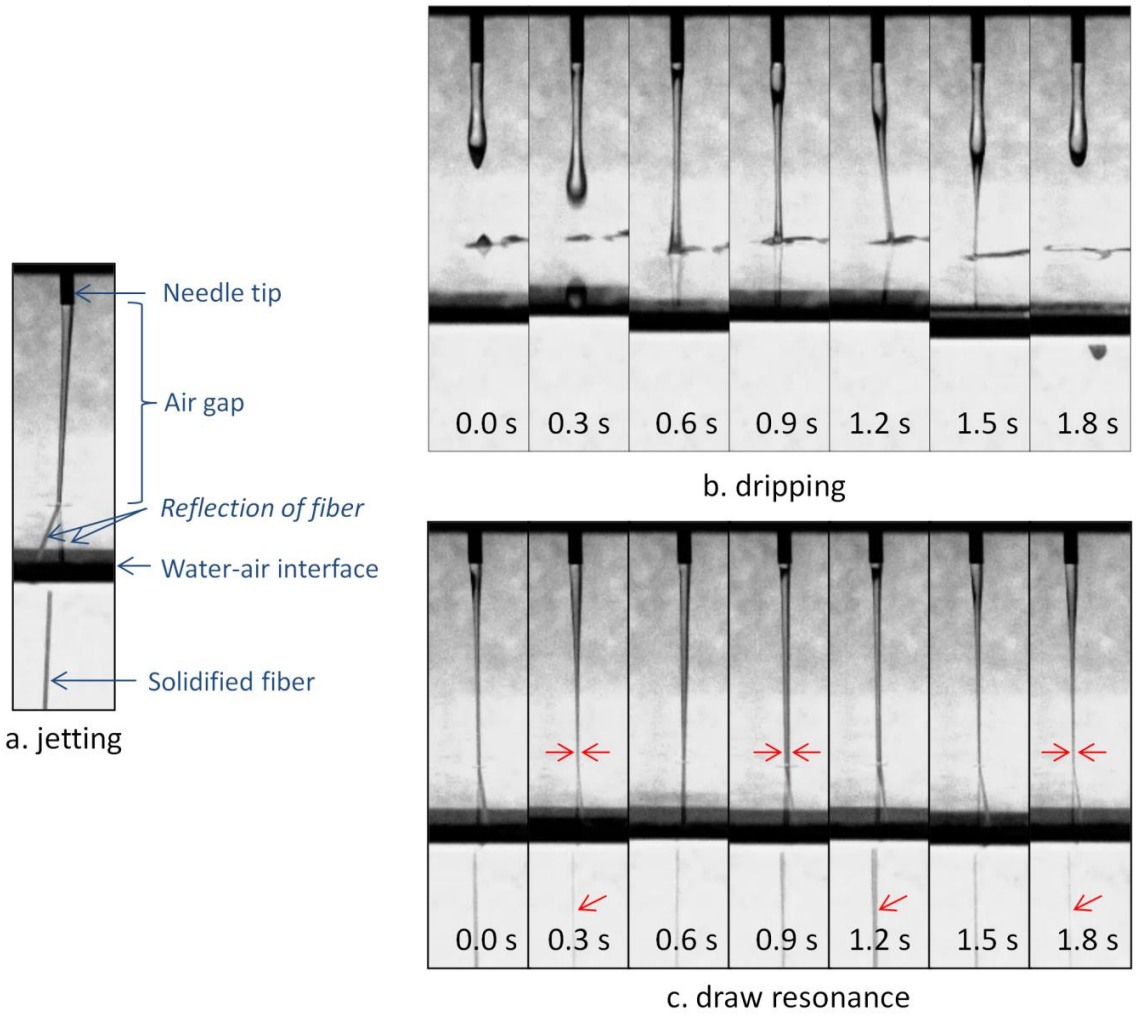

Figure 4.5 Characteristic flow behaviors at air gap of 1.5 cm. a. jetting regime: v_o = 1cm/s, DR = 10, t_{gap} = 0.38 s. b. dripping: v_o = 1cm/s, DR = 10, t_{gap} = 0.38 s. c. sagging: v_o = 1cm/s, DR = 20, t_{gap} = 0.24 s.

After the characteristic flow behaviors were categorized into five different regimes and this same procedure was repeated at three air gap distance 1.5 cm, 3 cm, and

6 cm, 135 conditions (45 x 3) in total. These data points were plotted in **Figure 4.6**, with axis of draw ratio versus t_{gap}, from PEI 24 to 31 wt% in NMP.

In general, sagging (green colored area with a symbol of trapezoid) was observed at draw ratios lower than 5 with long t_{gap} (top right corner) in all solutions, in all spinnability diagrams in **Figure 4.6**. In low viscosity samples, the regime of sagging was bigger than in high viscosity samples as the solution quickly flows (falls) down without a lingering moment for rearrangement of polymer chains. Dripping regime, which occurs due to low viscosity, is positioned on the corner of top right (grey colored area with a symbol of cross). As polymer concentration increases (viscosity increases), the dripping regime shrinks and totally disappears at PEI concentration of 30%.

Jetting regime (yellow colored area with a symbol of circle) is a desired stable regime and throughout **Figure 4.6**, the boundary between the jetting regime and draw resonance moves towards higher draw ratio as PEI concentration increases. In the PEI 24% and 26% solutions, the boundary of the transition is not sharp, located approximately at draw ratio of 8. One of the noticeable outlier is the long line of yellow dots at the t_{gap} about 0.2-0.3 s and at the draw ratio near 10-20, placed in the draw resonance regime (blue colored area with a symbol of square). These data points were from the air gap distance of 6 cm and extruded at fastest extrusion rate (v_o = 5cm/s). Although the absolute extrusion velocity is not the primary factor in this study, it is likely that the fast extrusion velocity stabilizes the flow by generating more inertia to the flow.

Another major factor that caused the unclear boundary of jetting and draw resonance in PES 24% and 26% is likely the counter effects of viscosity and phase separation kinetics. As shown in **Figure 4.4**, PEI 24% solutions have the fastest phase

separation rate and it is likely that the moisture-induced phase separation occurred faster in this sample during the residence time. The moisture-induced solid sheet at the outer surface stabilized the flow and prevented the draw resonance occurrence. Meanwhile, the low viscosity results in weak resistance to the drawing tension and more likely leads to the fiber breakage. The coupled effects of the viscosity and PSK exist through the rest of the samples, but the boundary of each regime became more distinguishable as PEI concentration increased because the phase separation rate decreases. The stable jetting regime expands as the PEI concentration is added and the critical boundary of the jetting and the draw resonance regime shifts from around 8 to 12.

4.3.1.3. Effect of dope viscosity on spinnability diagram

Comparison of the spinnability diagrams of PEI 30% and 31% in **Figure 4.6** explicitly presents the effect of dope viscosity since PEI 30% and PEI 31% solutions have diffusion coefficients of same order but different viscosities (**Figure 4.4**). In PEI 31% diagram, the sagging regime expands because of the face that more viscous solutions shows delay falling. The boundary between jetting and draw resonance remain almost same; higher viscosity of PEI 31% contributes to expansion of the spinning stability only at the longer air gap. Although the increase in dope viscosity was not effective on stabilizing the spinning flow, it has great impact on reducing break-up regime. The break-up regime in PEI 31% shrunk compared to the one in PEI 30%.

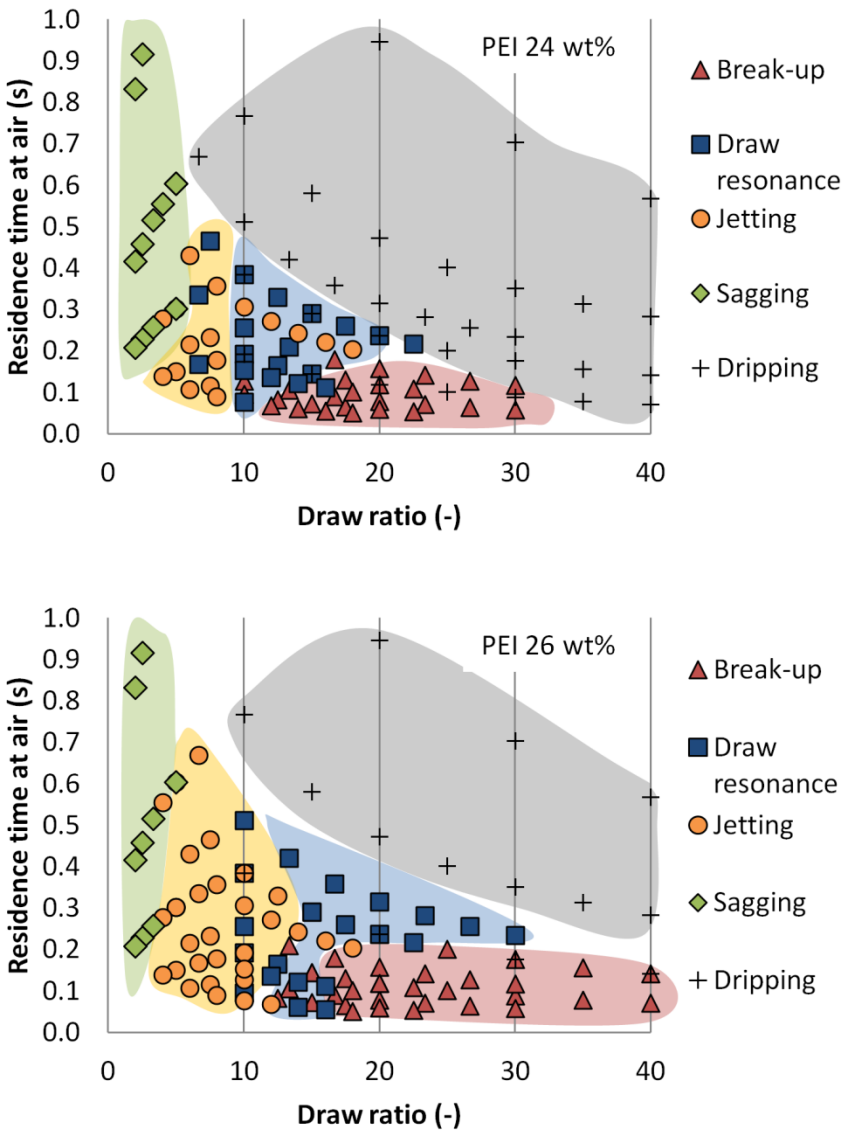

Figure 4.6 Spinnability diagram of PEI/NMP system with different PEI concentrations. From top to bottom 24, 26, 28, 30, and 31 wt% (continued).

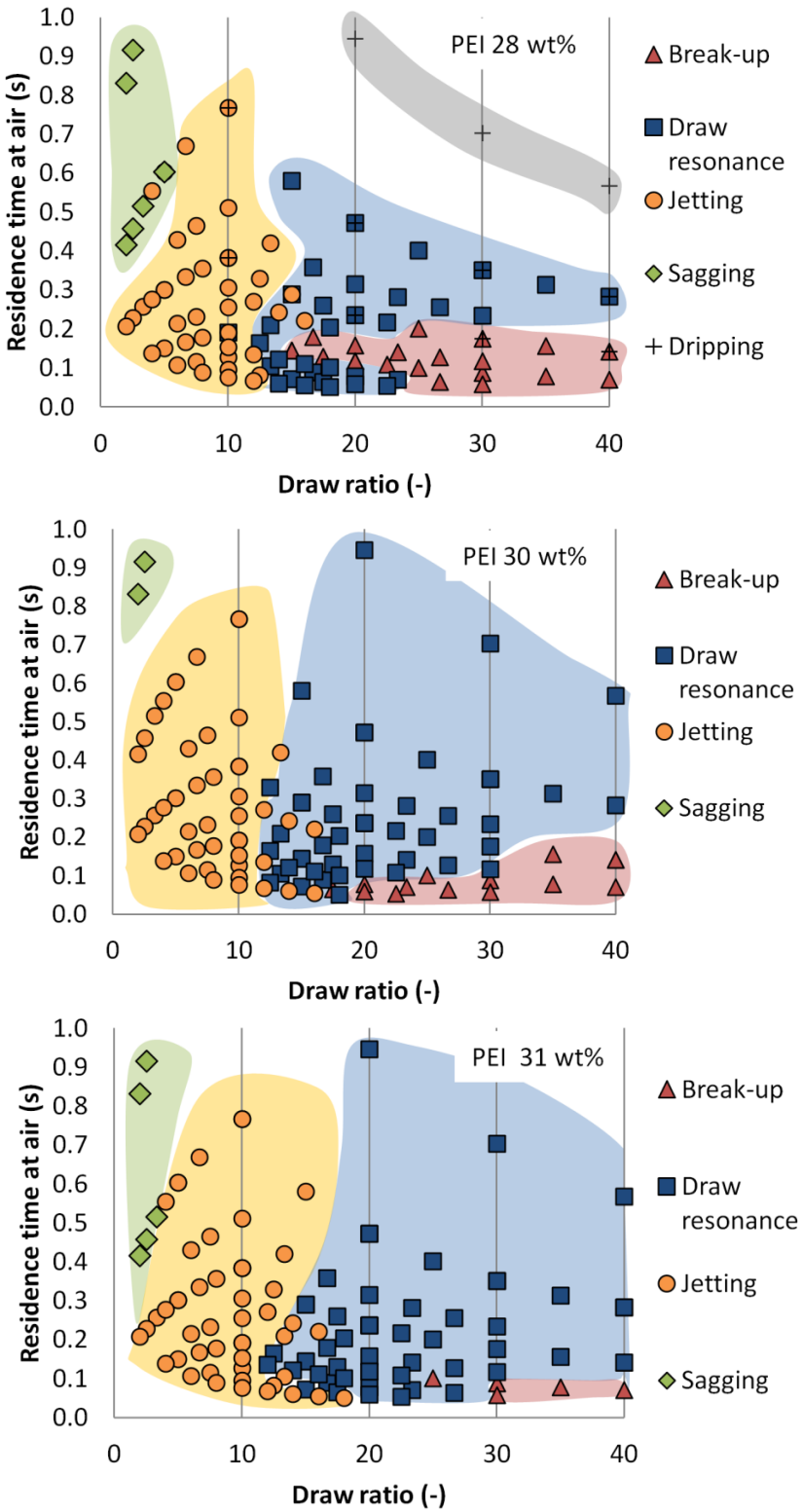

Figure 4.6 Spinnability diagram of PEI/NMP system with different PEI concentrations. From top to bottom 24, 26, 28, 30, and 31 wt%.

4.3.2. PEI/NMP/ethanol system

4.3.2.1. PEI 30% solution with ethanol

Adding ethanol into the solution increases both the solution viscosity and the phase separation rate, shown in **Figure 4.8**. In particular, addition of 10% ethanol enhanced the rate of phase separation three times faster. However, it should be also noted that the data of effective diffusivity should not be overanalyzed since the moisture-induced and nonsolvent-induced phase separation is essentially not the same. Moisture-induced phase separation is likely to occur slowly, forming denser structures than the nonsolvent-induced phase separation. Thus, the rate of phase separation should be used as a semi-quantitative guideline for the sensitivity or susceptibility to external thermodynamic change such as moisture or concentration gradients.

The spinnability diagrams the PEI dopes with and without ethanol were compared in **Figure 4.7**. Most noticeable change is the expansion of jetting regime, particularly at longer air gap residence time. The transition between the jetting and draw resonance regimes was near draw ratio of 16 at short residence time and expands up to almost 30 as the residence time increases.

The higher viscosity and the fast phase separation rate both works positively in stabilizing the fluid, the jetting regime was expanded. The effects of viscosity on stabilizing the spinning flow and expanding jetting regime is shown in PEI/NMP systems previously (**Figure 4.6**). Although the ethanol contained solution expanded the favorable jetting regime, the effect of changing phase separation rate need to be proved more clearly.

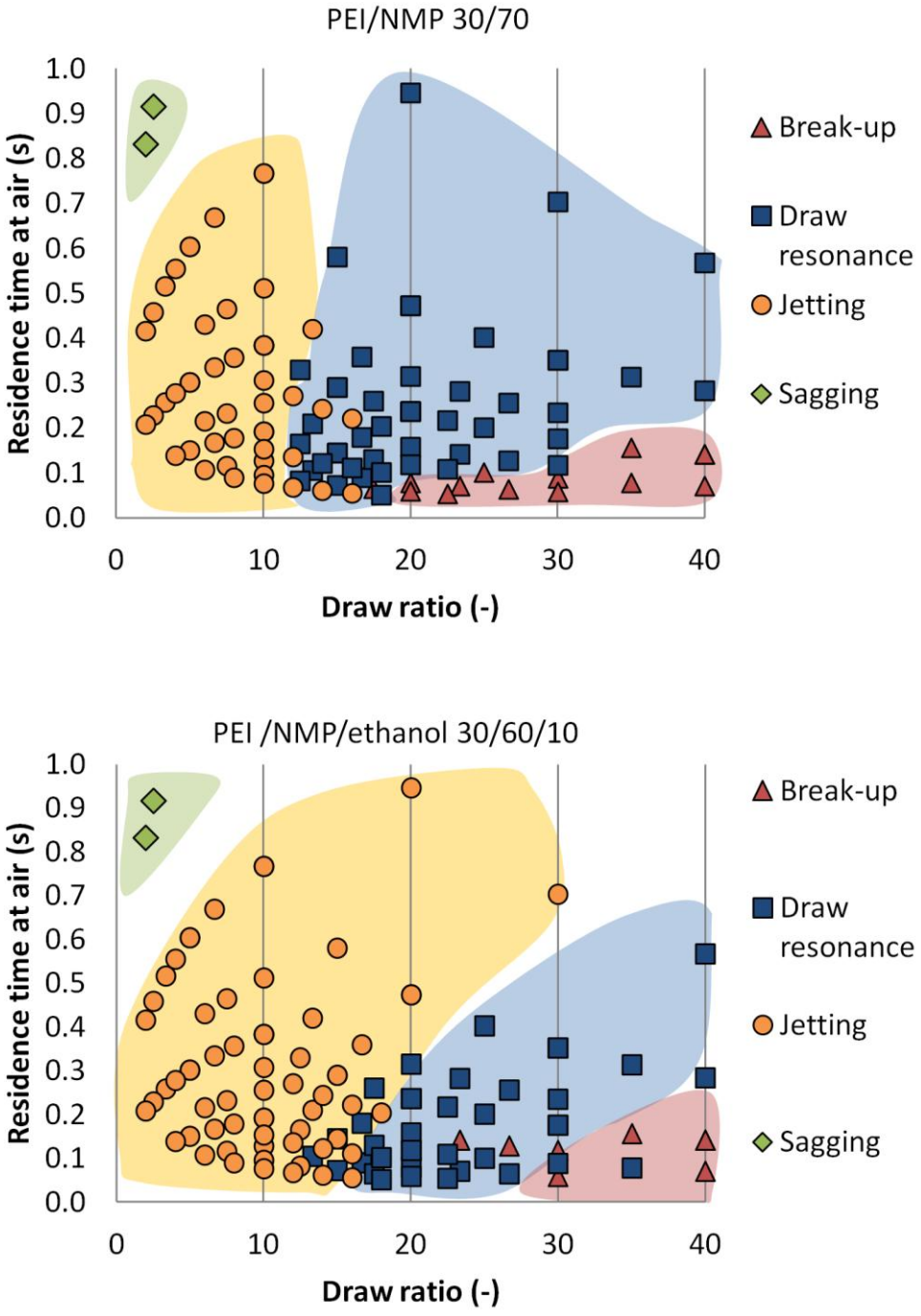

Figure 4.7 Spinnability diagram of PEI/NMP vs. PEI/NMP/ethanol system with PEI 30%.

4.3.2.2. Effect of PSK on spinnability diagram

PEI/NMP/ethanol (30/57.5/12,5) solution was formulated to have same viscosity (71 Pa s) as PEI/NMP (31/69) and but different phase separation rate, as shown in **Figure 4.8**. **Figure 4.9** shows the spinnability diagram of these two polymer solutions. In the diagram of PEI/NMP/ethanol (30/57.5/12.5), the jetting regime was expanded to draw ratio of 18 at short residence time (< 0.3 s) and larger than 20 at long residence time (> 0.3 s). It indicates that because of enhanced susceptibility of phase separation, the moisture-induced phase separation or solvent evaporation occurs more in the air gap and help stabilize the spinning flow even at more aggressive elongational conditions. Interestingly, the break-up regime increased because local solid formation reduced the liquid's deformability.

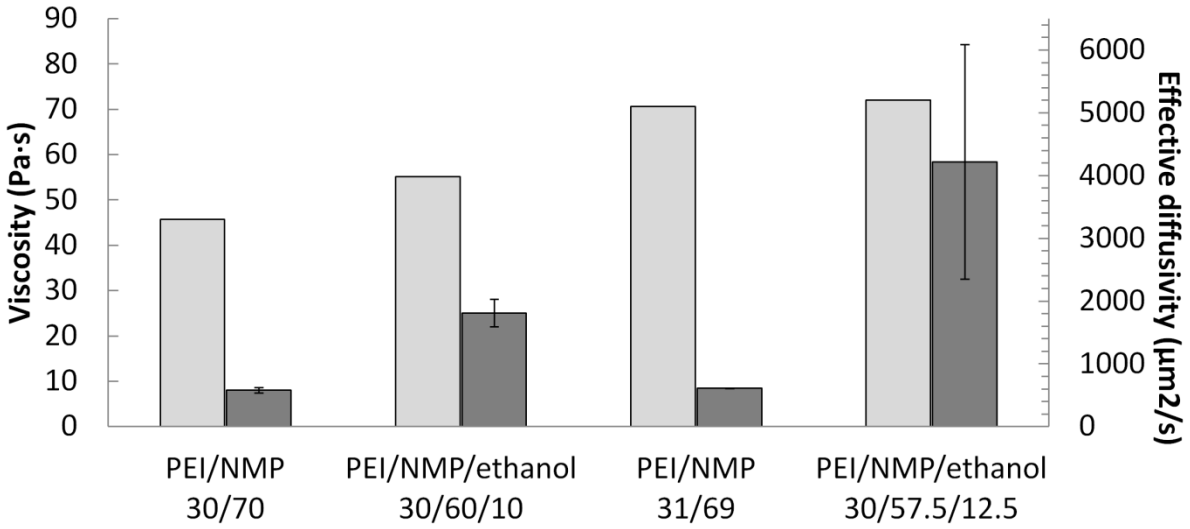

Figure 4.8 The comparison of viscosity and the phase separation rate of PEI/NMP solutions and PEI/NMP/ethanol solutions.

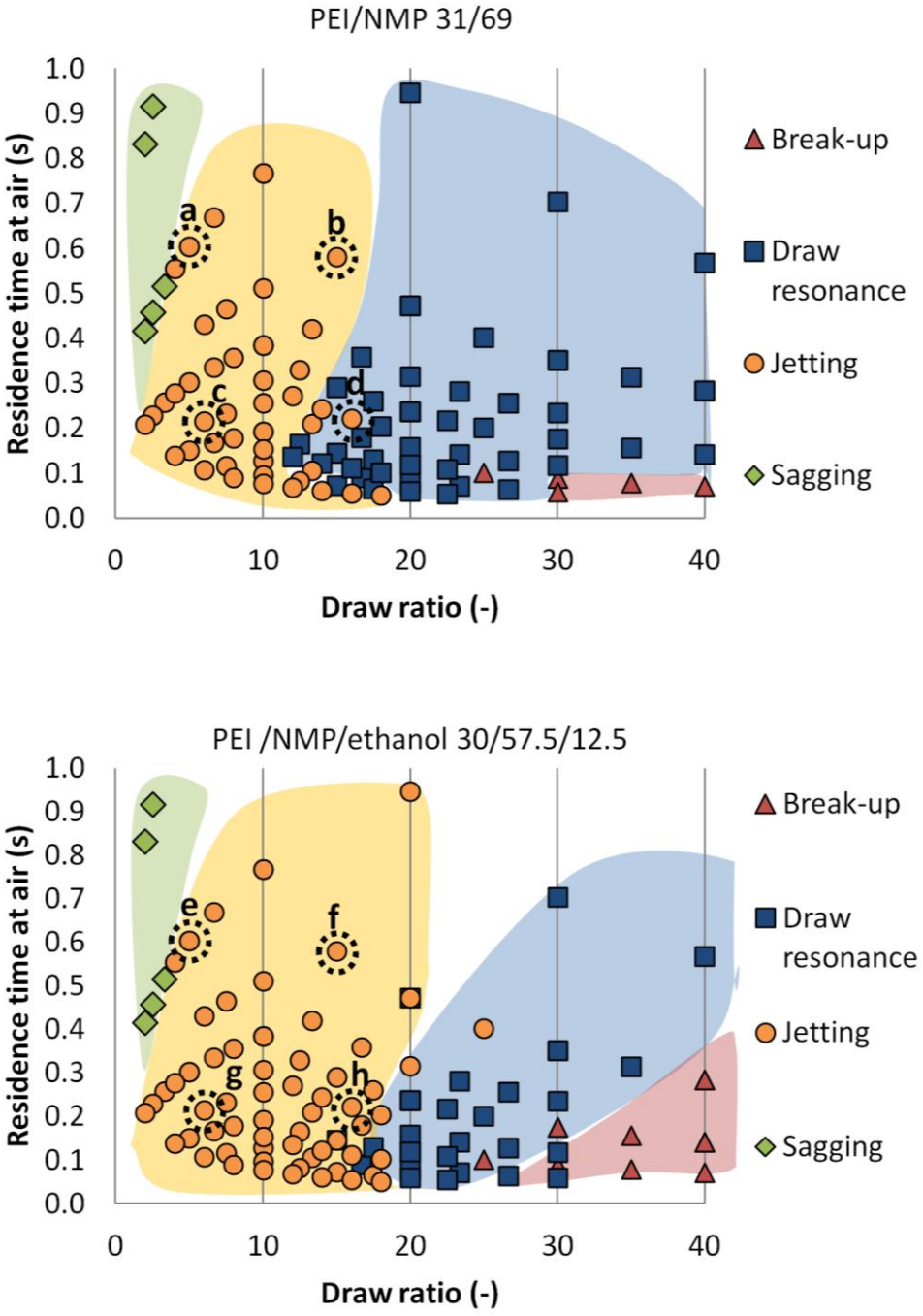

Figure 4.9 Spinnability diagram of PEI/NMP vs. PEI/NMP/ethanol system of same viscosity.

4.3.2.3. Comparison to the melt spinning

Based on the rheological properties of the PEI/NMP (30/70) and PEI/NMP/ethanol (30/60/10) in Chapter 3, the power law exponent of these fluids was approximately 0.5. If we apply this number to the spinnability diagram of power law fluids in **Figure 4.1**, the limit of critical draw ratio is around 8. However, our experiments showed 12 for the critical draw ratio of the PEI/NMP (30/70) and 16 for the one of PEI/NMP/ethanol (30/60/10). The discrepancy arises from the fact that the phase separation process is inevitable in real fiber spinning process with polymer solution. The previous theoretical and experimental studies are based on the assumption of isothermal spinning. The experimental setup of the isothermal spinning can be achieved by maintaining hot atmosphere while the cooled roller was used to draw the fiber. In case of polymer solutions, the phase separation process is essential in the process, and the humidity in air gap cannot be avoided.

4.3.2.4. Suggested methods to suppress instabilities in polymer solution spinning

From the theoretical studies on melt spinning and the experimental data, several methods can be suggested to suppress instabilities in polymer solution spinning.

- *Start-up condition*: typically, instant instabilities that arise at the start-up flow mostly fade away in the steady state and do not develop to draw resonance. However, other instabilities such as necking should also be avoided by starting at mild elongation conditions. Starting from the low take-up velocity i.e. low draw ratio and increasing to higher value gradually would help prevent instability

occurrence. In our observation, no draw resonance phenomena were found in a free falling condition or in the sagging regime.

- *Humidity*: just as the cooling air suppresses the instability in the melt spinning, humidified air condition can precipitate the moisture-induced phase separation in air gap and stabilizes the spinning flow. Supplying of cooling air is practically used in melt fiber spinning, and similar setup can be used in membrane spinning, such as covering water bath for closed air condition, increasing water bath temperature, or direct mist supply.
- *Co-solvent component in dope solution*: addition of co-solvent (e.g. ethanol) hastens the phase separation kinetics and formation of solid sheet will help stabilize the flow.
- *Water-air interface stabilization*: it was sometimes observed that once the draw resonance occurs, it resonates with the fluctuation of the water-air interface; therefore, the water-air interface must be stabilized before the actual fiber spinning.
- *Air gap*: in isothermal melt spinning, it was often reported that a small air gap distance stabilize the spinning flow, and our experiments somewhat agrees with the statement (expansion of jetting regime at $t_{gap} < 0.1$ s). However, it is only true in isothermal conditions with an assumption that solidification occurs at the cooling bath. In the solution spinning, the increase of air gap is likely to allow more time for phase separation and stabilize the spinline.
- *Spinneret design*: discussion about the spinneret dimensions was not treated well in open literature. As long as the assumption of thin liquid filament ($d << l$) is

valid, the theory of critical draw ratio is likely to be valid as well. Practically, the use of small spinneret dimensions will be favorable for the instability suppression because the fibers spun at smaller spinneret dimensions will have smaller fiber dimensions at identical draw ratio, and the mass transfer limitation will be more dominant. `

4.3.3. Morphological change in the fibers of PEI/NMP and PEI/NMP/ethanol, spun at jetting regime

In Chapter 3, we demonstrated how shear and elongation affects the fiber morphology and membrane defects. In this Chapter, our new finding is that the limit of stable regime is restricted by the draw ratio, elongational strain. Our next task now is to check whether our findings (the effects of shear and elongation) in Chapter 3 are still applicable in the stable jetting, which is limited by critical draw ratio.

Four conditions were chosen from jetting regime to see the morphological change of the fibers of PEI/NMP (31/69) and PEI/NMP/ethanol (30/57.5/12.5). Conditions are marked in **Figure 4.9** as a, e (draw ratio of 5 and t_{gap} of 0.60 s), b, f (draw ratio of 15 and t_{gap} of 0.58 s), c, g (draw ratio of 5 and t_{gap} of 0.22 s), and d, h (draw ratio of 16 and t_{gap} of 0.22 s). In **Figure 4.10**, the top four images are the cross-sectional images of the spun PEI/NMP (31/69) fibers and the bottom four are the ones of PEI/NMP/ethanol (30/57.5/12.5).

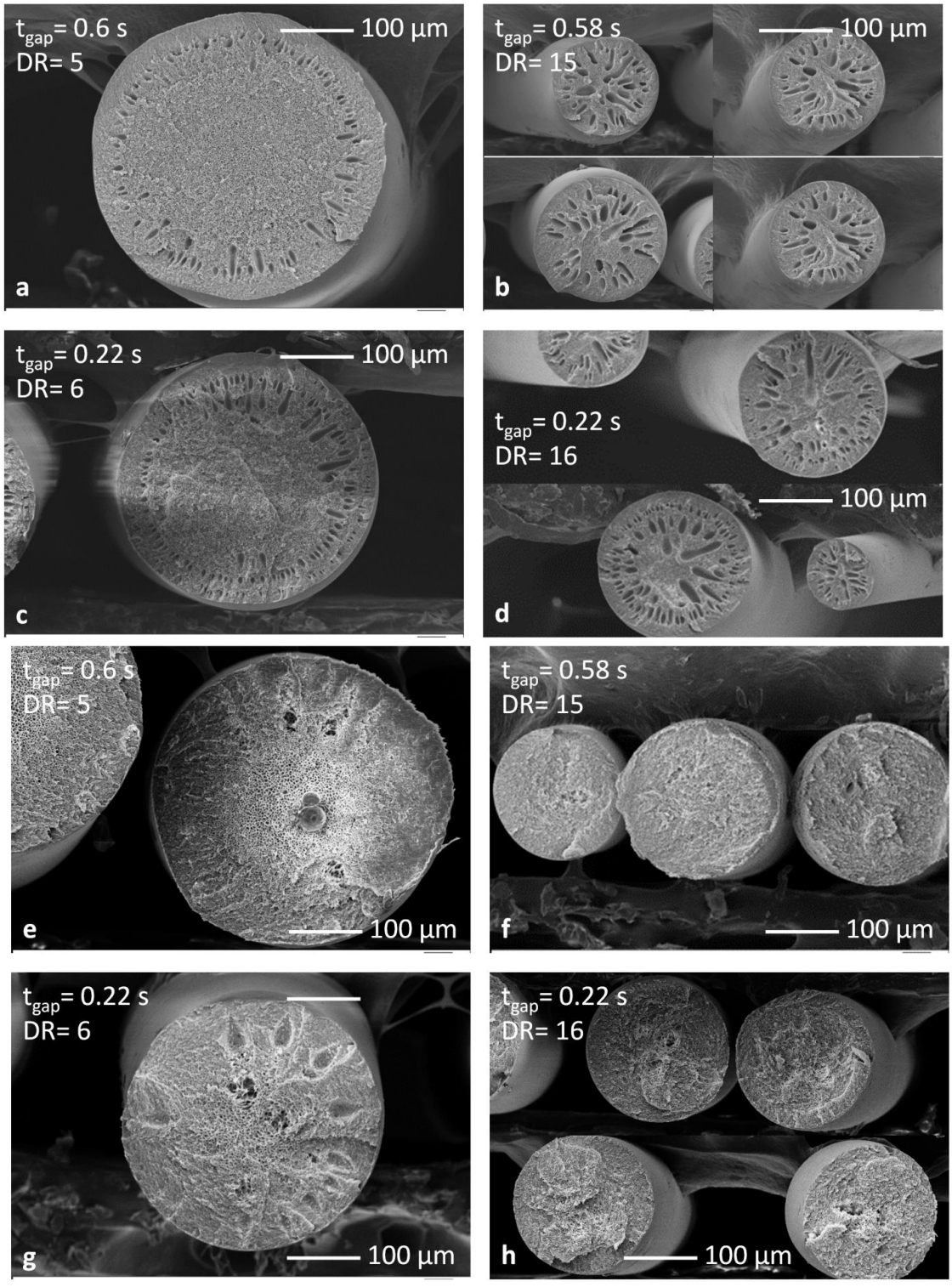

Figure 4.10 Scanning electron microscope images of the cross-section of PEI/NMP (top four) and PEI/NMP/ethanol (bottom four) fibers spun at different conditions.

One of the most noticeable features in PEI/NMP system is the macrovoid formation in all conditions. This result is consistent with the fact that the extruded PEI/NMP fibers contained macrovoids under any flow conditions (both in shear and elongational) in Chapter 3. As discussed, the initial dope composition was far from the binodal curve and the resulting morphology is likely dominated by change in thermodynamics rather than shear or elongational stresses.

The findings about PES/NMP/ethanol (30/60/10) solution in Chapter 3 were valid for PEI/NMP/ethanol (30/57.5/12.5), although the ethanol concentration is slightly higher in the dope. At the condition c (low draw ratio with short t_{gap}), the many macrovoids were found in the cross-sections. As the t_{gap} increases three times with fixed draw ratio (c → a), only few macrovoids left. This result is somewhat different from the results from Chapter 2, where the effects of solvent evaporation were investigated systematically with a microfluidic device. As a reminder, the solvent evaporation has influenced the kinetics of phase separation by slowing down the rate, but the macrovoids were not removed effectively even after very long evaporation time (~30 s). This discrepancy comes from the fact that the moisture-induced phase separation occurs simultaneously as well as the solvent evaporation. By comparing these results, we found that both solvent evaporation and the humidity-induced phase separation are required to effectively remove macrovoid formation.

If the draw ratio increases with a fixed t_{gap} (c→d), macrovoids are suppressed completely. Elongational stresses applied in the air are not entirely responsible for eliminating macrovoids because the shrinkage of fiber dimension also contributes to suppress macrovoid formation as discussed in previous chapter. Nevertheless, the fiber

diameter is much thicker than the critical thickness of macrocoid-free layer reported by Widjojo [32] and by fixing the residence time in the air, effects of solvent evaporation and the humidity has been also eliminated.

The average cross-sectional diameters of these fibers were determined and shown in **Figure 4.11**. The predicted diameter was calculated by following equation

$$(Draw\ ratio) = \frac{v_f}{v_0} = \frac{{d_{spinneret}}^2}{{d_{fiber}}^2} \tag{4.3}$$

based on mass conservation law. The actual fiber diameter was smaller than the predicted value in all conditions due to solvent loss during phase separation process. The dimensions of PEI/NMP/ethanol fibers were always larger than those of PEI/NMP fibers probably because the fast phase separation rate fixates the outer shape of the cross-section before the fibers shrink due to solvent removal. Although these conditions are thought to be in jetting regime, the large deviation of cross-sectional diameter was found in condition d (PEI/NMP 31/69). This large error is beyond the range of experimental error, indicating that the fiber may be in the draw resonance regime. In fact, condition d is in the mixed zone of jetting and draw resonance regime in **Figure 4.9** and the instability may have come from this.

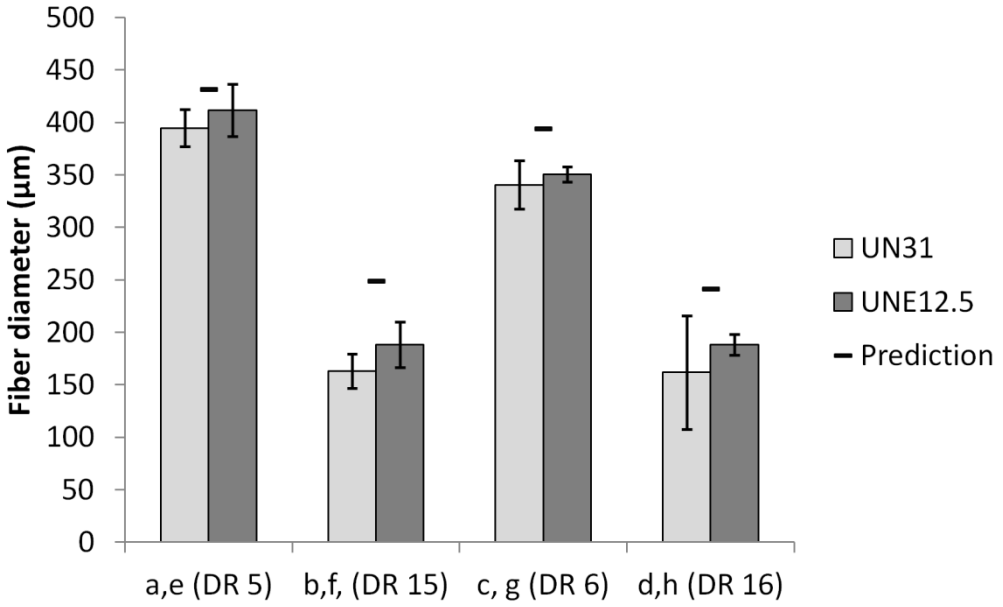

Figure 4.11 The measured cross-sectional diameters of PEI/NMP and PEI/NMP/ethanol fibers at different spinning conditions marked in **Figure 4.9**. Prediction values were calculated from Equation 4.3.

4.4. Conclusion

The occurrence of draw resonance (pulsing), a periodic fluctuation in diameter of the liquid fiber without breakage, was investigated in regards to the key variables, dope rheology and phase separation. Although draw resonance in polymer melt spinning is relatively well understood, not much knowledge exists in membrane spinning with polymer solutions. For the first time, we demonstrated the occurrence and suppression of draw resonance in solid fiber spinning with polymer solutions. The characteristic flow at the air gap was characterized into five different regimes, sagging, jetting, draw resonance, dripping and break-up, and the effects of shear viscosity and the phase separation kinetics on occurrence and suppression of the instability were demonstrated. The experimental

results showed deviation from the theoretical predictions of melt spinning because phase separation kinetics complicates the fiber formation process. Enhancing the kinetics of phase separation as well as increasing dope viscosity both resulted in expansion of the stable spinning regime toward more aggressive elongation condition without instabilities. More specifically, starting from low draw ratio, increasing humidity in air, adding co-solvent to the dope solution, using very small air gap, increasing air gap with the dopes of fast phase separation kinetics, and using small dimension spinneret are suggested to suppress the occurrence of draw resonance.

The findings about the effects of shear and elongation on fiber morphology in Chapter 3 were also confirmed in this chapter within the jetting regime. It was found that the fibers spun at higher draw ratio was contains fewer macrovoids. Also the polymeric dopes with the enhanced phase separation kinetics formed fibers with fewer macrovoids.

For a future study, the validity of the critical draw ratio in our solid fiber spinning must be tested for hollow fiber spinning. Although knowledge from polymer melt spinning indicates that the limit of draw resonance is valid both for solid and hollow fiber spinning, the presence of bore fluid and interaction between bore fluid and polymer solution may affect the occurrence and suppression of spinning instabilities.

4.5. References

[1] R.G. Larson, Instabilities in viscoelastic flows, Rheologica Acta, 31 (1992) 213-263.

[2] C.J.S. Petrie, M.M. Denn, Instabilities in polymer processing, AIChE Journal, 22 (1976) 209-236.

[3] G.G. Lipscomb, The melt hollow fiber spinning process: steady-state behavior, sensitivity and stability, Polymers for Advanced Technologies, 5 (1994) 745-758.

[4] S. Bonyadi, T.S. Chung, W.B. Krantz, Investigation of corrugation phenomenon in the inner contour of hollow fibers during the non-solvent induced phase-separation process, Journal of Membrane Science, 299 (2007) 200-210.

[5] O.M. Ekiner, G. Vassilatos, Polyaramide hollow fibers for H2/CH4 separation: II. Spinning and properties, Journal of Membrane Science, 186 (2001) 71-84.

[6] N. Widjojo, T. Chung, S. Kulprathipanja, The fabrication of hollow fiber membranes with double-layer mixed-matrix materials for gas separation, Journal of Membrane Science, 325 (2008) 326-335.

[7] S. Husain, W.J. Koros, Macrovoids in hybrid organic/inorganic hollow fiber membranes, Industrial & Engineering Chemistry Research, 48 (2009) 2372-2379.

[8] D. Wallace, C. Staudtbickel, W. Koros, Efficient development of effective hollow fiber membranes for gas separations from novel polymers, Journal of Membrane Science, 278 (2006) 92-104.

[9] D.W. Wallace, J. Williams, C. Staudt-Bickel, W.J. Koros, Characterization of crosslinked hollow fiber membranes, Polymer, 47 (2006) 1207-1216.

[10] N. Peng, T. Chung, J. Lai, The rheology of Torlon® solutions and its role in the formation of ultra-thin defect-free Torlon® hollow fiber membranes for gas separation, Journal of Membrane Science, 326 (2009) 608-617.

[11] N. Peng, effects of spinneret dimension and hollow fiber dimension on gas separation performance of ultra-thin defect-free Torlon &reg hollow fiber membranes, Journal of Membrane Science, 310 (2008) 455-465.

[12] R. Van Der Hout, Draw resonance in isothermal fibre spinning of Newtonian and power-law fluids, European Journal of Applied Mathematics, 11 (2000) 129-136.

[13] J.S. Lee, H.W. Jung, J.C. Hyun, L.E. Scriven, Simple indicator of draw resonance instability in melt spinning processes, AIChE Journal, 51 (2005) 2869-2874.

[14] J.C. Chang, M.M. Denn, F.T. Geyling, Effects of inertia, surface tension, and gravity on the stability of isothermal drawing of Newtonian fluids, Industrial & Engineering Chemistry Fundamentals, 20 (1981) 147-149.

[15] Y.U.N.J. Ho, S.D. Myeong, L.E.E.J. Sung, J.H. Wook, H.J. Chun, Direct Calculation of Limit Cycles of Draw Resonance and Their Stability in Spinning Process, Nihon Reoroji Gakkaishi, 36 (2008) 133-136.

[16] J. Pearson, M. Matovich, Spinning a molten threadline. Stability, Industrial & Engineering Chemistry Fundamentals, 8 (1969) 605-609.

[17] A. Bergonzoni, A. DiCresce, The phenomenon of draw resonance in polymeric melts. Part I—qualitative view, Polymer Engineering and Science, 6 (1966) 45-49.

[18] J.A. Pearson, Y.T. Shah, On the stability of isothermal and nonisothermal fiber spinning of power-law fluids, Industrial & Engineering Chemistry Fundamentals, 13 (1974) 134-138.

[19] W. Minoshima, J.L. White, Instability phenomena in tubular film, and melt spinning of rheologically characterized high density, low density and linear low density polyethylenes, Journal of Non-Newtonian Fluid Mechanics, 19 (1986) 275-302.

[20] J.L. White, Y. Ide, Instabilities and failure in elongational flow and melt spinning of fibers, Journal of Applied Polymer Science, 22 (1978) 3057-3074.

[21] R. Christensen, Extrusion coating of polypropylene, SPE Journal, 18 (1962) 751-755.

[22] J.C. Miller, Swelling behavior in extrusion, Polymer Engineering and Science, 3 (1963) 134-137.

[23] R.J. Fisher, M.M. Denn, A theory of isothermal melt spinning and draw resonance, AIChE Journal, 22 (1976) 236-246.

[24] J.R.A. Pearson, M.A. Matovich, Spinning a molten threadline. Stability, Industrial & Engineering Chemistry Fundamentals, 8 (1969) 605-609.

[25] S. Kase, Studies on melt spinning. IV. On the stability of melt spinning, Journal of Applied Polymer Science, 18 (1974) 3279-3304.

[26] D. Gelder, The stability of fiber drawing processes, Industrial & Engineering Chemistry Fundamentals, 10 (1971) 534-535.

[27] G.J. Donnelly, C.B. Weinberger, Stability of isothermal fiber spinning of a Newtonian fluid, Industrial & Engineering Chemistry Fundamentals, 14 (1975) 334-337.

[28] J.C. Hyun, Theory of draw resonance: Part II. Power-law and maxwell fluids, AIChE Journal, 24 (1978) 423-426.

[29] J.R.A. Pearson, Y.T. Shah, R.D. Mhaskar, On the stability of fiber spinning of freezing fluids, Industrial & Engineering Chemistry Fundamentals, 15 (1976) 31-37.

[30] J.C. Hyun, Theory of draw resonance: Part I. Newtonian fluids, AIChE Journal, 24 (1978) 418-422.

[31] K.O. Olanrewaju, The rheology and phase separation kinetics of mixed-matrix membrane dopes, in, Georgia Institute of Technology, 2011.

[32] N. Widjojo, Thickness and air gap dependence of macrovoid evolution in phase-inversion asymmetric hollow fiber membranes, Industrial and Engineering Chemistry Research, 45 (2006) 7618-7626.

CHAPTER 5

CONCLUSIONS

In this thesis, we primarily focused our attention on investigating the key variables in hollow fiber membrane spinning, which are the phase separation kinetics and rheology. The key conclusions are listed below.

- PDMS (polydimethylsiloxane) microfluidic device was fabricated for *in situ* observation of phase separation process. One of the major advantages of this device is that it enables quantitative analysis for both wet, and dry wet phase separation with excellent controllability in air/liquid flow. Another improvement is that the solidified polymer samples can be taken out of the device and prepared for morphology analysis.
- In ternary dope formulations (polymer/solvent/volatile co-solvent), the evaporation of the volatile component slows down the phase separation rate upon exposure to non-solvent but has minimal effects on suppression of macrovoid formation.
- In binary formulations (polymer/solvent), the phase separation rate is determined by the polymer concentration regardless of polymer molecular weight, while the formation of macrovoid defects is mainly affected by the bulk dope viscosity.
- In all cases, the evolution of macrovoid defects, when they occur, is always faster than the progression of phase separation.

- In binary formulations (polymer/solvent), the effective diffusivity of the phase separation can be predicted from the solubility parameter difference between the polymeric dope and the nonsolvent being used (alcohol analogues and NMP/water mixtures); there is a linear correlation between the effective diffusivity and the solubility parameter difference.
- Straight and contraction channel were fabricated to see the effects of shear and elongational stresses on polymer morphology. *In situ* membrane structure formation including macrovoids under various flow conditions were observed and compared with corresponding morphology.
- Depending on the shear rate, the membrane morphology, especially macrovoid formation is affected by different controlling factors; mass transfer at low extrusion regime, thermodynamics of the dopes at intermediate regime, and deformation rate or stresses (shear & elongation) at high speed extrusion regime.
- Shear induces the macrovoid formation while elongation suppresses it, only when the polymeric fluid is extruded at high speed.
- The prediction of draw resonance in polymer melt spinning is not directly applicable to polymer solution spinning.
- The effect of rheology is dominant at low viscosity sample; once the viscosity exceeds a threshold, the effect of viscosity on the onset of the draw resonance is minimal.
- Moisture-induced phase separation in the air gap stabilize the spinning flow, just like the cooling air stabilize the spinning flow in the polymer melt spinning; the

hypothesis is that the humidity-induced pseudo-solid thin sheet at the outer layer of the fiber suppress the occurrence of the draw resonance.

These conclusions are discussed in more detail below with recommendations toward future study.

5.1. Study of phase separation kinetics with a microfluidic device

Chapter 2 described experiments measuring the kinetics of wet and dry-wet phase separation with microfluidic devices. Due to the sensitivity of most polymeric dopes to (co-)solvent evaporation and nonsolvents in the atmosphere (humidity), it was necessary to develop a novel experimental setup that combines experiments on relevant length scales with excellent control over the composition of the environmental conditions to which the dope solution is exposed; this includes both the controlled exposure to liquid nonsolvent, as well as the composition of the gas phase with which the dope is in contact. Thus, a large portion of this chapter includes the device fabrication and optimization for the target experiments. Microfluidic devices were used because of excellent control over flow conditions and their suitability for phase separation experiments on the relevant length scale for membrane fibers.

Polymeric dopes composed of a ternary system (polymer/solvent/volatile co-solvent) were used to demonstrate the ability to study dry wet phase separation in a microfluidic device. The experimental challenge was to prevent evaporation of solvent during sample loading into the microfluidic channel. We solved this problem by keeping the dope solution in contact with nitrogen gas that was saturated with ethanol vapor.

Although this pushed the dope past the cloud point during the loading, subsequent exposure to dry nitrogen led to controlled removal of excess ethanol, so that the turbid region of the dope solution recovered its transparency. It was found that co-solvent evaporation reduces the phase separation rate on fairly short timescales (0 s ~20 s). The formation of macrovoids, however, was not suppressed significantly by co-solvent evaporation.

A binary system (polymer/solvent) with different polymer molecular weights was used to demonstrate the effects of polymer properties on the phase separation rate and macrovoid growth rate during wet phase separation. The experimental design focused on two sample sets: polymer solutions at the same polymer concentration with different viscosities, and solutions with different concentrations, but (almost) constant dope viscosity. The results showed that solutions with the same polymer concentration exhibit the same kinetics of phase separation, independent of polymer molecular weight (and dope viscosity). This can be explained by the fact that phase separation is a microscopic process that involves diffusion of non-solvent molecules through the polymeric network. The resistance against this mass transfer process is largely defined by the mesh size of the polymer solution, which depends on polymer concentration and not on bulk viscosity. On the other hand, it was found that the macrovoid formation rate is determined by the dope viscosity; in the sample with lowest viscosity, the macrovoid formation rate was fastest and vice versa. In the samples that were designed to have the same viscosity, the macrovoid formation rate was also constant within experimental errors.

The binary system (polymer/solvent) was also used with various non-solvents in wet phase separation experiments. The non-solvents used were alcohol analogues

(methanol, ethanol, isopropanol, 2-butanol, and 2-hexanol) and a series of NMP/water mixtures (0/100, 20/80, 30/70, 40/60, 50/50, 60/40, 70/30, 80/20, 85/15, and 90/10 wt%). It has been known that miscibility between the solvent and non-solvent affects the phase separation rate and our experiments showed a linear correlation between the solubility parameter difference (between the polymer and nonsolvent) and the effective diffusivity of phase separation. As the phase separation rate decreases, the resulting polymer morphology becomes more porous while macrovoids were eliminated.

For the first time, our study provides a thorough quantitative analysis of the phase separation kinetics and the corresponding polymer morphology. Previous research was either focused on the qualitative analysis of phase separation kinetics, on the characterization of fiber morphology, or on separation properties of the resulting membranes. In addition to the analysis of phase separation kinetics, our microfluidic device enabled post-characterization of the samples with scanning electron microscopy, because the solidified polymer samples can easily be removed from the microfluidic device.

The recommendation related to this topic is further automation of the microfluidic device. Control over the air and liquid flow is crucial for the quantitative analysis on the phase separation. For example, one of the difficulties encountered during device operation was stress compliance of the microfluidic devices, tubing and syringe; the flow of dope solution did not immediately stop even when the injection stopped. An automated system would be able to optimize the sample injection rate, injection volume as well as the timing of non-solvent injection, which would result in improvement of reproducibility.

As a topic of future study, the kinetics of phase separation in advanced systems is worth investigating. In actual hollow fiber spinning, the phase separation simultaneously occurs in two directions, from the shell side and from the bore side; both processes are induced by different non-solvents. In some research [1, 2], the macrovoids formed in the middle of the hollow fiber and this fact raises an interesting question: *which side* of phase separation is responsible for the formation of these macrovoids? Simultaneous dual phase separation could be visualized in a microfluidic device with nonsolvent counter flow on opposite sides of the dope solution; such an experiment would reveal the morphological changes that occur when the two phase separation fronts in the dope solution meet and interfere with each other.

5.2. Study of effects of shear and elongation on membrane morphology by extrusion

Chapter 3 presented the experiments investigating the effects of shear and elongation on the membrane morphology. In the hollow fiber spinning, the effects of these parameters are systematically coupled with other process parameters such as fiber dimension change and moisture-induced phase separation. In this study, the dope solutions were exposed to the shear and elongational stresses by extrusion, decoupled from other parameters. The real time observation of phase separation as well as macrovoid formation under different flow conditions were demonstrated using optical video microscopy.

Large portion of this chapter is dedicated to the microfluidic channel fabrication for shear flow and elongational flow. The device was fabricated with conventional soft lithography technique [3], and PDMS and TPE (thermosetting polyester resin) were used to construct a straight channel (shear) and a contraction channel (elongation). The polymer solutions were loaded from a syringe and extruded into non-solvent (water) bath, i.e., wet phase separation.

Binary (polymer/solvent) and ternary systems (polymer/solvent/volatile co-solvent) were used as model samples. The viscosity flow curves were measured and used for calculation of the velocity profile in the channels. The solutions were extruded through a straight channel and a contraction channel at various flow rates. Maximum wall shear rates and elongational rates were calculated and used as representative deformation rates for each condition.

Correlation between the materials' rheological properties, the deformation rates (shear and elongation), and resulting membrane morphology, and *in situ* phase separation video were collected in so-called "flow regime maps". It was found that the membrane morphology is dominated by different factors depending on the deformation rates. For example, in the case of shear flow, dominant factors were mass transfer at low shear rates, thermodynamics of polymer solution at intermediate shear rates, and normal stresses at high shear rates. Each of these factors leads to the formation of characteristic macrovoid defects: axial macrovoids, radial macrovoids, and secondary macrovoids, respectively. These morphological changes were prominent in the ternary dope solution, where the solution composition is determined closely to the binodal curve.

In the regime of high speed extrusion, it was found that shear stresses induced macrovoid formation while elongational stresses suppressed it. The extruded fibers from a straight channel contained secondary macrovoid defects because of high shear stresses and the fiber dimensions were also increased by die swell. These macrovoids can be suppressed if the fibers were exposed to the elongational stresses by extruding them from a contraction channel even at very high extrusion rate.

Several experiments can be recommended as a follow-up regarding this topic. First, it is important to check if the flow regime map is valid in extrusion experiments with different channel sizes. Although the dimensions of the slit channel were kept close to the actual fiber thickness (~50 μm), it has been demonstrated by other researchers that macrovoid formation strongly depends on the membrane thickness. Knowing the applicable range of the flow regime map is important for the use as a guideline for determining the spinning conditions and as a prediction for the resulting morphology.

Another recommended experiment is the coextrusion of dope solution with a bore fluid through a concentric channel, more closely resembling a spinneret with wet phase separation. One of the advantages of using PDMS for microfluidics is the ease in fabrication of various geometries, and concentric channels are in principle possible. Such a device would be helpful for improving our understanding of some issues that occur on the bore side, such as corrugation (shape irregularity) of the inner contour [4], as well as the macrovoid formation.

5.3. Study of instability in fiber spinning with aspects of rheology and phase separation kinetics

Chapter 4 demonstrated the effect of rheology and the kinetics of phase separation on the occurrence and suppression of spinning instability. Draw resonance, often referred to as "pulsing" in the field of membrane spinning, is commonly encountered in fiber spinning. This phenomenon is relatively well-known in the field of polymer melt spinning, but not much knowledge exists in the field of polymer solution spinning. Our study is the first attempt to investigate the spinning instability with polymeric dopes in application of membrane spinning.

The two key building blocks of the membrane spinning, dope rheology and the phase separation kinetics were investigated as a characterization of the dope solutions. The binary system (polymer/solvent) with different polymer concentrations and the ternary system (polymer/solvent/volatile co-solvent) with different solvent ratios were used as model dopes. The shear viscosity of the binary solution increased exponentially as the polymer concentration increased. Meanwhile, the kinetics of phase separation decreased and reached plateau as more polymer was added. These characterization data were used to interpret the spinning instability.

Solid fiber spinning from a syringe was conducted for instability analysis. The changed parameters were the air gap distance, the extrusion velocity, and the take-up velocity. At each condition, the draw ratio, which represents the amount of elongation experienced by the fiber (Hencky strain), and the residence time in the air gap, which represents the exposure time to the air, were calculated and used as the principle

variables. The characteristic flow regimes were categorized into five classes: dripping, sagging, break-up, draw resonance, and jetting. The first four are likely to lead to the failure, even to the cease of continuous operation. Only the jetting flow without disturbances was considered as a favorable stabilized condition.

The spinnability diagram was drawn as a function of the parameters draw ratio and residence time in the air gap. For the binary system, it was found that the jetting regime expands with higher polymer concentration. In the spinnability diagram for high polymer concentration solutions that exhibit similar phase separation kinetics but have different viscosities, the jetting regime expanded slightly with increases in viscosity. However, for low viscosity solutions, the boundary between the stable (jetting) and unstable (draw resonance) regimes was not clear, due to the counter effect of viscosity and phase separation kinetics; as polymer concentration increased, the viscosity increased while the rate of phase separation decreased. These effects were therefore decoupled by adjusting the solution composition. The ternary system (polymer/solvent/volatile co-solvent) was used as samples with enhanced phase separation kinetics. The spinnability diagrams of the samples with similar viscosity but different phase separation rate indicates that the fast phase separation rate shifts the onset of the draw resonance towards more aggressive elongation conditions. This suggests that the enhanced phase separation kinetics stabilizes the spinning flow in air gap, and suppresses the occurrence of instability.

Our results have strong implications for hollow fiber membrane spinning. Our experiments show that in addition to microstructural defects like macrovoids, the spinnable conditions are restricted by the occurrence of instabilities. Although the

phenomenon of draw resonance has been studied for melt spinning, the theoretical and numerical predictions for melt spinning cannot be applied directly to membrane spinning, which is more complicated because of the phase separation effects. However, knowledge and techniques in polymer melt spinning can be useful in polymer solution spinning; for example, it was found that enhanced phase separation kinetics stabilizes the spinning flow, analogous to the application of cooling air in air the gap during melt spinning.

A key recommendation with regards to this topic is to extend the work to a hollow fiber spinning setup. Although it is known from the melt spinning literature that predictions of the onset of the draw resonance are valid for both solid fiber spinning and hollow fiber spinning [5], experimental variables associated with the bore side flow may add complexity to the system in case of membrane spinning with polymer solutions.

Another recommendation for the spinning instability analysis is hollow fiber membrane spinning in non-isothermal conditions. In practice, high temperature dope solutions are used to improve the ease of extrusion through the spinneret by reducing viscosity. Although the non-isothermal condition is likely to complicate the fabrication process, spinning instabilities could be suppressed significantly due to the combined effects of the cooling air and phase separation in the air gap. This is expected to expand the spinnable regime greatly, which can eventually lead to improvement in membrane production efficiency.

5.4. References

[1] M.M. Teoh, T.-S. Chung, Micelle-like macrovoids in mixed matrix PVDF-PTFE hollow fiber membranes, Journal of Membrane Science, 338 (2009) 5-10.

[2] N. Widjojo, Thickness and air gap dependence of macrovoid evolution in phase-inversion asymmetric hollow fiber membranes, Industrial and Engineering Chemistry Research, 45 (2006) 7618-7626.

[3] J.C. McDonald, D.C. Duffy, J.R. Anderson, D.T. Chiu, H. Wu, O.J.A. Schueller, G.M. Whitesides, Fabrication of microfluidic systems in poly(dimethylsiloxane), Electrophoresis, 21 (2000) 27-40.

[4] S. Bonyadi, T.S. Chung, W.B. Krantz, Investigation of corrugation phenomenon in the inner contour of hollow fibers during the non-solvent induced phase-separation process, Journal of Membrane Science, 299 (2007) 200-210.

[5] G.G. Lipscomb, The melt hollow fiber spinning process: steady-state behavior, sensitivity and stability, Polymers for Advanced Technologies, 5 (1994) 745-758.